UNIVERSITY OF CATANIA

DEPARTMENT OF CHEMICAL SCIENCES

INTERNATIONAL PhD IN CHEMICAL SCIENCES

XXXIV CYCLE

Vincenzo Patamia

Cucurbiturils, tetrahedral capsules, and porous systems: synthesis, functionalization, and applications

PhD Thesis

Tutor
Prof. Antonio Rescifina

Ph.D. Coordinator

Prof. Salvatore Sortino

ACADEMIC YEAR 2020–2021

*"L'uomo non è che un fuscello, il più debole
della natura, ma è un fuscello che pensa."*

Blaise Pascal

*"Meravigliarsi di tutto è il primo passo della
ragione verso la scoperta."*

Louis Pasteur

Table of content

Abstract

Taking a cue from the principles developed by the founding fathers of supramolecular chemistry, my Ph.D. program consists of four lines of research that develop in a multidisciplinary plan starting from alternative and more environmentally friendly synthesis methodologies.

During the first year, a new synthetic strategy was developed to prepare cucurbit[7]uril through the use of molecular models to increase the yield of CB[7] compared to the classical syntheses reported so far. The conversion of the imidazole models into magnetic liquid facilitated the separation of CB[7], which, in general, is time-consuming and costly in terms of time and money. Subsequently, CB[7] was used as a supramolecular reactor for the stereocontrolled synthesis of substituted isoxazolidines by exploiting the 1,3-dipolar cycloaddition reaction. The reaction was carried out under "GREEN" conditions using water and microwaves. Remaining in the context of the use of water as a reaction solvent, in the second part of the first year and the beginning of the second year of the doctorate, a tetrahedral capsule was exploited as a nanoreactor for the realization of dehydration reactions in water, in particular for the synthesis of nitrones. A new supramolecular system was developed during the second year, capable of adsorbing a significant amount of carbon dioxide. This system was developed starting from the cucurbit[6]uril, which was functionalized with 12 chains of 1-(ethyl)-3-methyl-1H-imidazol-3-ium bromide. The presence of the positively charged imidazole groups made possible the

formation of cation-dipole interactions between the positively charged side chain of a functionalized CB[6] and the carbonyl dipole of another functionalized CB[6]. This network of interactions led to the formation of further interstices, in addition to the cavities of the macrocycles, which transformed the system into a supramolecular nanosponge. Furthermore, the adsorbed CO_2 was used to perform the carboxylation of phenylacetylene was easily and satisfactorily accomplished.

Finally, following the current topic of environmental awareness in the development of new advanced materials that are both ecological and capable of exhibiting the properties targeted for the required application, was developed a straightforward and rapid synthetic methodology to synthesize a new hybrid, ecological and reusable material starting from cheap materials such as loofah and halloysite.

The composite showed a significantly greater ability to absorb and retain carbon dioxide than non-contaminated materials. This underlines the synergistic effect of the two materials, which also possess a greater adsorption capacity than the BEA and MOR zeolites, which are currently used in the industrial field for gas adsorption and require more prolonged and more expensive synthetic processes. Moreover, the synergistic effect of the materials is evident in the greater carrying capacity of resveratrol compared to individual materials. This study opens another way towards developing hybrid, organic-inorganic materials, applicable in multiple fields and at the same time eco-sustainable and economical.

Chapter 1. Cucurbit[7]uril: synthesis and applications

1.1 Introduction

"Supramolecular chemistry is the chemistry of the intermolecular bond, covering the structures and functions of the entities formed by the association of two or more chemical species."[1]

This was the definition given by Jean-Marie Lehn, one of the founding fathers of supramolecular chemistry.

Its development requires the use of all the theoretical and experimental resources of molecular chemistry combined with well-designed manipulations of non-covalent interactions to form entities called supramolecular with well-defined characteristics. The associations between the molecules have been identified and studied for a long time, and the term *Übermolekül*, which mean supramolecule, was introduced already in the mid-thirties of the twentieth century to describe entities endowed with a high degree of organization, which derived from the association of species saturated in a coordinated manner.[2] The associated entities in a supramolecular species have been called molecular receptors and substrate. The latter, in general, is the smallest component with which an attempt is made to obtain a bond. Molecular interactions are the basis of a series of peculiar phenomena of recognition, reaction, transport, regulation, and more; of typical processes of biology, such as, for example, the link between a substrate and a receptor protein, enzymatic reactions, the establishment of biological structures, the immunological associations between antigens and

antibodies, intermolecular recognition, translation and transcription of the code genetic, signal transmission through neurotransmitters and cellular recognition.[3] The design of artificial, abiotic receptor molecules, characterized by very high efficiency and selectivity, requires a correct manipulation of the energetic and stereochemical properties of non-covalent intermolecular forces, such as electrostatic interactions, hydrogen bonding, van der Waals forces.[4]

The binding of a *Guest* substrate with its receptor *Host* leads to the formation of a supramolecular *Host-Guest* and implies a molecular recognition process (Figure 1).[5]

Figure 1.

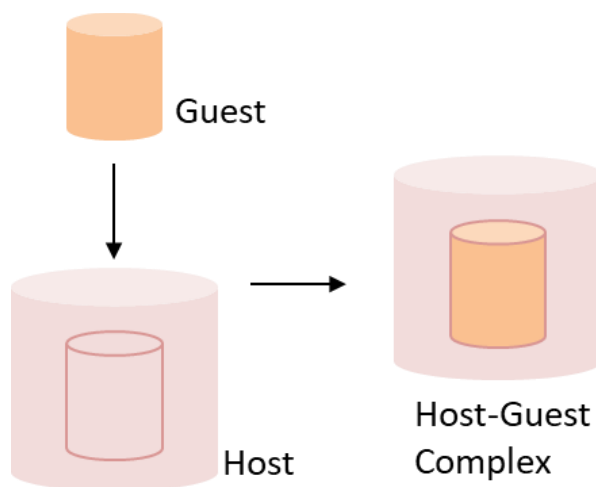If the receptor also has reactive functions in addition to the binding sites, it can cause a chemical transformation on the bound substrate, acting as a supramolecular reagent or catalyst. A lipophilic receptor, soluble in the membranes, can act as a substrate transporter. Therefore, molecular recognition, transformation, and relocation represent the essential functions of the supramolecular species. In association with

polymolecular organizations and phases (layers, membranes, vesicles, liquid crystals), supramolecules could form molecular devices. Another fundamental aspect of supramolecular chemistry is molecular recognition, whose bases were given by Emil Fischer in 1894.[6] He postulated the *Lock and Key* concept to explain the specific action of an enzyme with a single substrate (Figure 2).
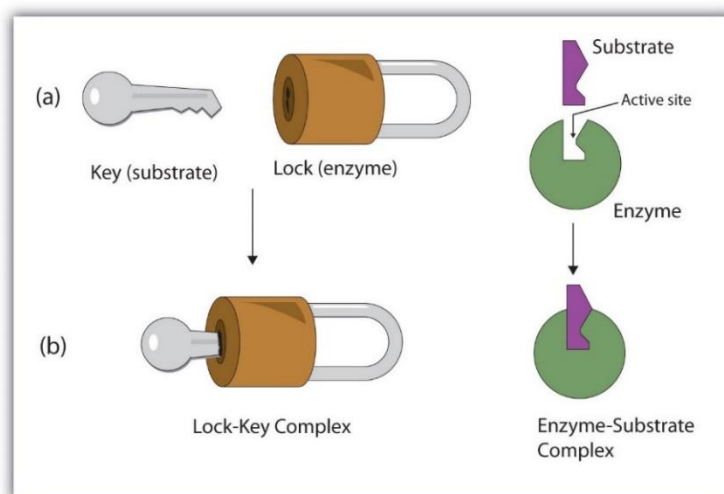
Figure 2.

Molecular recognition has been defined as a process involving the binding and selection of substrates by a receptor molecule and possibly a specific function. It implies a structurally well-defined network of intermolecular interactions. The interactions between *Host* and *Guest* create a supramolecule characterized by specific stability and a determined kinetic and thermodynamic selectivity, and therefore by the quantity of energy and information involved.[7]

The chemistry of artificial receptor molecules could be considered as generalized

coordination chemistry, not limited only to the ions of transition metals but extended to all types of substrates, such as anionic, cationic, or neutral species of inorganic, organic, or biological nature. To obtain recognition with high efficiency, it would be convenient for the receptor and the substrate to have a wide interaction surface. This occurs when the *Host* can interact with the *Guest* creating a high number of non-covalent ligand interactions and when the *Host* and *Guest* have a high degree of shape complementarity.[8] This occurs with receptor molecules containing intramolecular cavities within which the substrate can sit, giving rise to an inclusion complex.

In addition to molecular recognition, reactivity and catalysis are characteristics of great importance for supramolecular systems.[5] The molecular receptors that possess appropriate reactive groups, in addition to the binding sites, can complex a substrate that possesses specific characteristics of stability, selectivity, and kinetics, and react with it with a given speed, selectivity, and a given turnover and subsequently release the products, thus regenerating the reagent for a new cycle.[9] The supramolecular reactivity and catalysis, therefore, involve two main steps: the formation of the bond, which selects the substrate, and the transformation of the species bound into products. Both steps take part in the molecular recognition of the productive substrate and require the correct molecular information on the reactive receptor. The design of reagents and efficient and selective supramolecular catalysts could offer information on the mechanisms that intervene in the elementary stages of catalysis, provide new types of chemical reagents, and produce reactions capable of detecting

the factors that contribute to enzymatic catalysis.

The supramolecular chemistry is based on molecular receptors organized in a more or less rigid way, obtained synthetically, able to perform molecular recognition, catalysis, and transport processes. The design of systems subject to self-organization, *i.e.*, capable of spontaneously generating well-defined functional molecular architectures through the self-assembly of the components according to a series of conditions, is located at a more advanced stage compared to pre-organized systems.[10] Therefore, we can have designed assemblies of elements within well-defined discrete supramolecular species or spontaneous formations of molecular layers, films, membranes, and so on. The phenomena of self-assembly require the formation of bonds. Construction rules must be stored within the various components and operate through selective molecular interactions for a self-organizing process to take place.[11] Therefore, systems of this type could be called programmed molecular and supramolecular systems, capable of generating organized entities following a defined plan based on molecular recognition phenomena. Self-organizing phenomena can take place in solution, in the liquid crystalline phase or the solid-state, and use hydrogen bonds, electrostatic effects or of the acceptor-donor type, or coordination of metal ions, such as fundamental interactions between the components, or due effects to the medium in which they take place.[12]

Numerous supramolecular biological structures can originate from the self-assembly processes, such as, for example, occurs in the spontaneous formation of the double helix of nucleic acids, the protein coating of viruses, and multiprotein complexes.

The development of supramolecular chemistry implies increasing the complete control of molecules, supramolecules, and materials. Although many studies deal with biological or biomimetic substances, the main interest is concentrated on abiotic, non-natural species produced by the chemist's imagination and which possess determined and desired chemical, biological or physical properties.[13]

1.2 Macrocycles and self-assembling capsules as a supramolecular catalyst

There are different types of macrocycles used as supramolecular catalysts in literature because they have a cavity that can accommodate different substrates.[14] The macrocycles are systems made up of subunits, the so-called building blocks, joined by covalent bonds. The number and characteristics of the building blocks determine the macrocycle's dimensions and chemical-physical characteristics.[13] Many of them have a hydrophobic cavity capable of accommodating one or more hydrophobic substrates; furthermore, some macrocycles have a hydrophilic surface useful for solubilizing hydrophobic molecules in aqueous environment. For this reason, when the subunits that constitute the macrocycle are synthesized, the chemist must think about what the chemical and physical characteristics of the final system must be.[15]

Three of the most widely used supramolecular systems for their ability to transfer hydrophobic substrates to the aqueous environment are cucurbiturils, cyclodextrins,

and resorcinarenes (Figure 3).
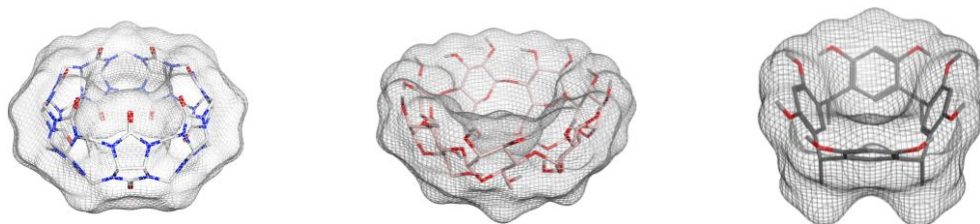
Figure 3.

Such systems were used as supramolecular catalysts, often using water as a reaction solvent.[16] In addition to macrocycles, there are other supramolecular systems whose building blocks are held together by non-covalent bonds. The interactions that are established between building blocks are generally hydrogen bonds and coordination bonds between a metal and a binder.[17] Some of them are able to self-assemble by forming supramolecular complexes, even in water, by exploiting the interactions mentioned above.[18] Below are reported two of these: a hexameric capsule consisting of resorcinarene units held together by hydrogen bonds; and a tetrahedral capsule whose ligands are capable of complexing the metals that make up the vertices of the capsule (Figure 4).

Figure 4.

All the macrocycles and self-assembling capsules, so far cited, have been used as supramolecular catalysts.[19] This has been possible by exploiting their hydrophobic cavity; furthermore, having a hydrophilic surface, it has been possible, in some cases, to use water as the reaction solvent.[20]
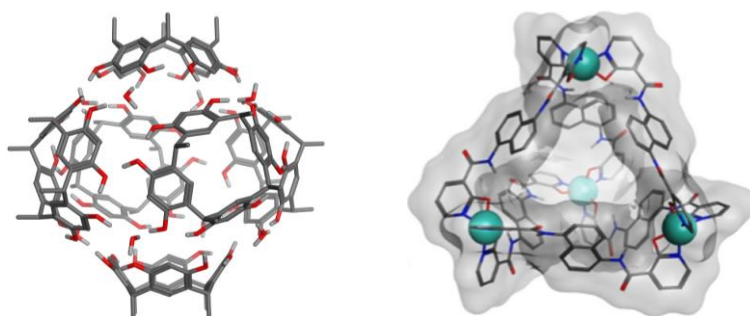
The purpose of this project is to synthesize a macrocycle and a self-assembling capsule in order to be able to use them as supramolecular nanoreactors to catalyze some reactions using water as a solvent.

I synthesized the cucurbit[7]uril macrocycle because it has a high solubility in water and a hydrophobic cavity large enough to accommodate the reaction substrates. Subsequently has been developed the synthesis of the building blocks for a capsule, already present in literature, capable of self-assembling in water. Also, in this case, the aim is to use it as a supramolecular nanoreactor.

In the first part of the report, a new type of synthesis for cucurbit[7]uril will be shown and its subsequent application as a catalyst. In the second part, the synthesis of the ligand of the tetrahedral capsule, already present in literature, and its first applications as a nanoreactor will be presented. In both cases, the water will be used as a solvent.

1.3 Cucurbiturils

Among catalysts, cucurbiturils (CB[*n*]s), cyclic-oligomers compounds formed by *n* glycoluril units (where *n* is typically between 5 and 8 Figure 5) cyclically bounded *via* methylene bridges,[21] have attracted in the last years the attention of many

researchers.[22] The number of repeat units defines the size and cavity volume of this class of compounds. The dipolar nature of the carbonyl portion of the glycoluril that forms the portals of CB[*n*] imparts a cation binding affinity, whereas the inner cavity of CB[*n*] is remarkably hydrophobic as other classes of similar compounds.[23] This class of macrocycles can shield organic molecules from aqueous environments while encapsulating them in a hydrophobic cavity. From the standpoint of organic chemistry, they can be a useful catalyst, similar to analogous macrocycle reactors.[24]
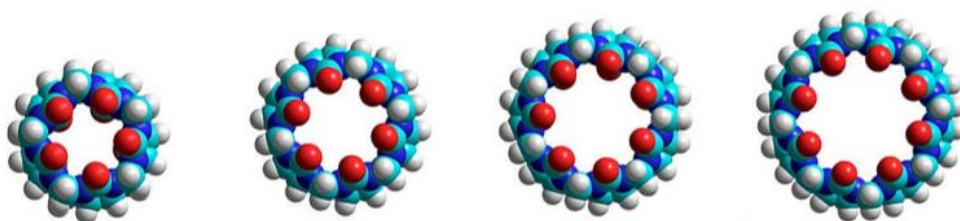
Figure 5. Series of cucurbiturils from 5 to 8 units of glycoluril.

The project's first objective is to synthesize the CB[7] by developing a new method that had a higher yield than the reactions already present in the literature, making separation easier than other homologs. In the literature, there are different methods to synthesize the CB[7] that differ for the different types of acid used, for the temperature, the reaction times and the various separation methods. The reaction reported in Figure 6, present in the literature, is that which allows obtaining the best yield with respect to CB[7], about 21%.[25]
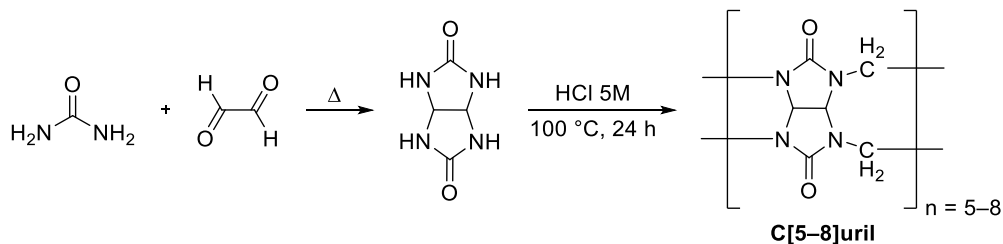
Figure 6. General procedure for the synthesis of cucurbiturils.

Generally, the purification methods used to separate CB[7] from other homologs are based on the different solubility of these systems in different solvents, making the process tedious and also expensive in terms of time and money.[25]

By exploiting the high capacity of the cucurbit[7]uril to form complexes with some systems, a new, efficient method was used, which uses templating molecules to synthesize the CB[7].

The templating molecules allow the monomeric units of glycoluril to pre-organize around them, thus facilitating the formation of the macrocycle with the exact dimensions. Furthermore, the use of these templants has facilitated the process of separating CB[7] from other homologs.

After developing the synthesis of CB[7], it was used to create an ecological and efficient method for the synthesis of 3,5-diarylisoxazolidine in water. In particular, the reactions between different para-substituted nitrones such as the dipole and various styrenes or cinnamates such as dipolarophiles have been studied.

1.4 Results and Discussion

In order to optimize the optimal reaction condition, we initially studied a model reaction between glycoluril and 3-ethyl-1-methyl-1*H*-imidazol-3-ium bromide (Figure 7), varying the templating equivalents and obtaining the best yield (Table 1).
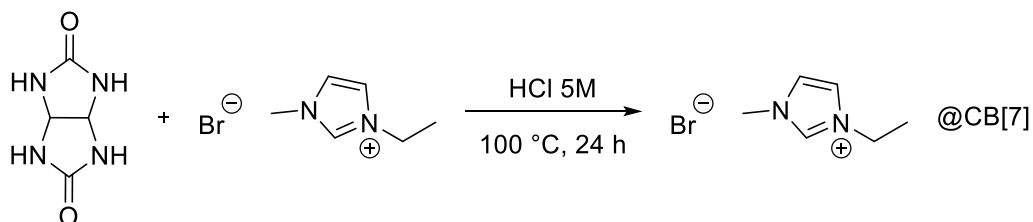
Figure 7. Synthesis of cucurbit[7]uril assisted by 3-ethyl-1-methyl-1*H*-imidazol-3-ium bromide.

Table 1. Optimization of synthesis of CB [7] assisted by 3-ethyl-1-methyl-1*H*-imidazol-3-ium bromide.

Entry	Eq. Et-Imid. log K 5.48	Eq. Glycoluril	Eq. Formaldehyde	HCl (M)	Yield %			
					CB[5]	CB[6]	CB[7]	CB[8]
1	0.14	1	2	5	4.0	70.0	24.0	2.0
2	0.50	1	2	5	6.5	65.3	23.5	4.7

Using the first mold molecule, Et-Imid., which has a complexation constant equal to log 5.48 with respect to CB[7], we can see how the synthesis yield is slightly higher than those present in the literature.

Once the reaction conditions were established, the templating molecules were varied in order to find the molecule that gave us the highest yield (Table 2).

Table 2. Synthesis CB [7] using different templating molecules.

Templating molecule	Yield %			
	CB[5]	CB[6]	CB[7]	CB[8]
Butyl-Imid. (log K 6.88)	—	61.0	30.5	8.5
1-adamantylamine (log K 14.32)	—	54,6	45.4	—
1-adamantanol (log K 10.36)	8.2	68.0	23.8	—
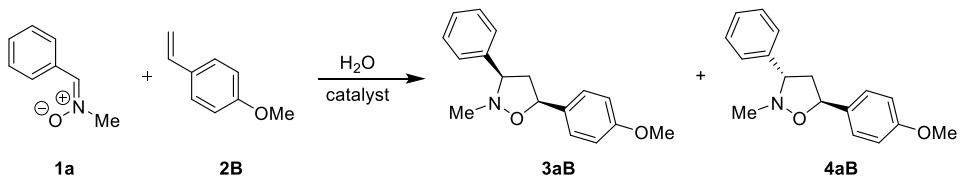
In Table 2, it can be seen that the best yield is given by 1-adamantylamine, and therefore, it is possible to deduce how the reaction yield increases parallel to the complexation constants.[26] Subsequently, for the separation of the CB[7] from the other cucurbiturils, two different methods have been used, adapted in function of the type of template used for the synthesis. The molecular molds with an imidazole structure have a rapid and straightforward separation of the cucurbi[7]uril from the mixture of reactions. They are ionic liquids capable of transforming into magnetic ionic liquids reacting with $FeCl_3$, as shown in Figure 8.
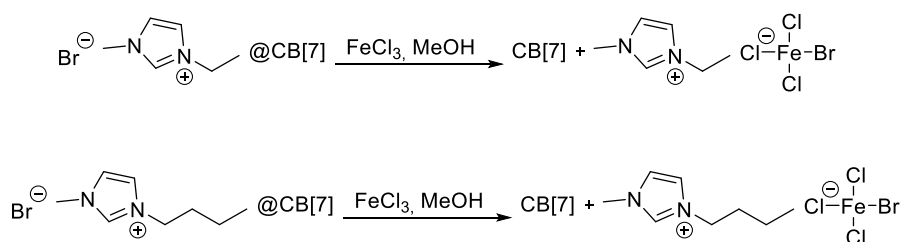
Figure 8. Separation of the complex imidazole@CB[7] using $FeCl_3$.

The reaction between the imidazole@CB[7] and $FeCl_3$ allowed the template to exit from the macrocycle cavity by using a magnet. The synthesis yield of CB[7] was calculated from the integrals of the ^{13}C NMR resonances for each homolog from the

reaction crude because ^{1}H NMR resonances were not clearly distinguishable. This method, very often used in the literature for these macrocycles, uses correlation factors that are divided by the integral of the peak of each homolog.[25] In any case, the yields were confirmed by weighing the quantity of product obtained after the separation. Instead, a small reversed-phase chromatography column was used to separate the complexes formed with 1-adamantylamine and 1-adamantanol. Developed the new and efficient method of synthesis for cucurbit[7]uril, this was used as a supramolecular catalyst for the synthesis of 3,5-diarylisoxazolidine in water. In order to optimize the optimal reaction condition, we initially studied a model reaction between nitrone **1a** and styrene **2B**, using water as a solvent, and varying the catalyst (Table 3).

Table 3. Optimization of the reaction conditions between nitrone **1a** and styrene **2B**.[a]

Entry	Catalyst	Eq.	Time (h)	Total yield (%)
1	—	—	48	—
2	CB[5]	1.0	24	—
3	CB[5]	2.0	24	—
4	CB[6]	1.0	24	—
5	CB[6]	2.0	24	—
6	CB[7]	1.0	24	82
7	CB[7]	1.5	24	55
8	CB[7]	2.0	24	traces
9	CB[7]	3.0	24	traces
10	CB[7]	0.5	24	85
11	CB[7]	0.2	24	94
12	CB[7]	0.1	24	93

[a] Reactions conducted in a sealed tube with 1 eq. of **1a** and 1 eq. of **2B** at 100 °C.

The screening was initiated by using three different cucurbiturils (CB[5], CB[6], and CB[7]) to determine their effective catalytic capabilities. No isoxazolidine formation was observed without the supramolecular catalyst in the water at 100 °C for 48 h or longer (Table 3, entry 1). The CB[5] and CB[6] did not show any catalytic activity in the dipolar cycloaddition (Table 3, entries 2–5), probably because they are not able to form inclusion complexes with the reactants due to their small cavity. On the contrary, the CB[7] efficiently catalyzed the reaction giving a good yield (Table 3, entry 6). Increasing the quantity of catalyst at 1.5 eq. reduced the yield (Table 3, entry 7), and, with two or three equivalents, only traces of products were observed (Table 3, entries 8 and 9). This behavior could be explained by the formation of individual nitrone and styrene complexes within the CB[7] cavity that avoids the two reactants coming in close contact and provide indirect proof that the CB[7] behaves as an effective nanoreactor in water. Lowering the amount of CB[7] from 1 to 0.5, 0.2, and 0.1 equivalents increases the efficiency of the reaction bringing the yields to 93% and demonstrating that the CB[7] can be used in actually catalytic quantities (Table 1, entries 10–12).

To further improve the reaction times, we conduct the reaction under microwave irradiations (Table 2). In this way, we maintained the high yields of the reaction but lowering the reaction time to 4 hours (Table 2, entry 7) using 1.2 eq. of nitrone, 1.0 eq. of styrene, 0.1 eq. of CB[7], and performing the reaction at 120 °C and 80 W. The use of 1.2 eq. of nitrone was due to its enhanced hydrolysis at these conditions.

To overcome this problem, we proved to perform the reaction without solvent, grinding the two reagents and the catalyst in an agate mortar. Although the reaction proceeded with a high yield in only 1.5 h (Table 2, entry 8), the grinding of a mixture containing an oil and the successive workup of the solid aggregated mass obtained at the end of the reaction discourage the use of this methodology.

Table 4. Optimization of the MW reaction condition between nitrone **1a** and styrene **2B** in water[a].

Entry	1a (eq.)	2B (eq.)	CB[7] (eq.)	Total yield (%)
1	1.0	1.0	1.0	82
3	1.0	1.0	0.1	75
5	1.0	1.0	2.0	—
6	1.2	1.0	0.2	94
7[b]	1.2	1.0	0.1	93
8[c]	1.0	1.0	0.1	93

[a] Reaction performed for 6 h at 80 W (120 °C); [b] Reaction performed for 4 h at 80 W (120 °C); [c] Reaction performed for 1.5 h at 80 W (120 °C) without solvent.

Then, under the optimized reaction conditions (Table 4, entry 7), we carried out the reaction between nitrones **1a,b**, and styrenes **2A–C** in both toluene and water (in the presence of CB[7]) solution to compare the classic with the new strategy (Scheme 1, Table 5). In all the cases, the reaction proceeds with complete regioselectivity and improvement of yield with respect to the one carried out in toluene; moreover, the supramolecular catalyst effectively controls the stereoselectivity outcomes improving the formation of the *trans* cycloadduct, except for the isoxazolidines **3**,**4bC**.
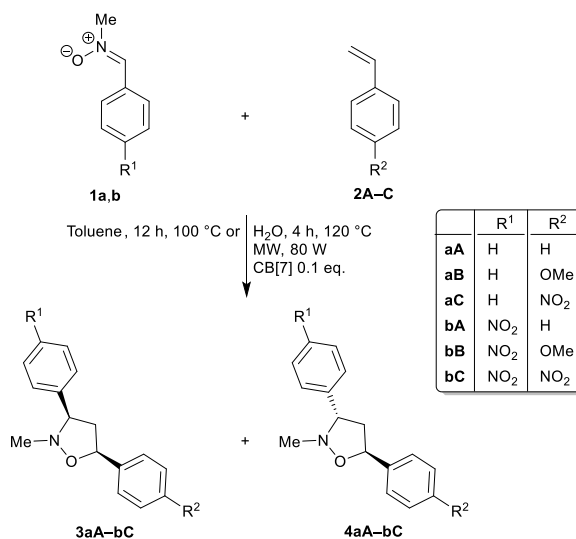
Scheme 1. Reactions of nitrones **1a,B** with styrenes **2A**–**C**, at the optimized conditions.

Table 5. Reactions of nitrones **1a,B**, and styrenes **2A**–**C** in both optimized conditions in water and toluene.

	Reactions in toluene without CB[7]		Reactions in water with CB[7]	
Isoxazolidine	**cis/trans ratio[a]**	**Total yield (%)**	**cis/trans ratio[a]**	**Total yield (%)**
3,4aA	3.0/1	79	1.3/1	92
3,4aB	3.1/1	75	1.0/1	92
3,4aC	2.8/1	77	1.7/1	76
3,4bA	3.3/1	80	1.9/1	82
3,4bB	3.1/1	79	2.5/1	85
3,4bC	2.7/1	77	4.8/1	75

[a] The proportion of the cycloadducts was determined by ^{1}H NMR analysis of the crude product mixture.

The catalytic ability of CB[7] can be elucidated by the formation of a host-guest complex between the reactants and the macrocycle. In this way, the reactants are first solubilized in the aqueous medium, where the CB[7] acts like a phase-transfer catalyst.

The formation of the inclusion complexes between the two reactants used in the model reaction (nitrone **1a** and styrene **2B**) and the molecular reactor CB[7] was studied by NMR and MS experiments. The ^{1}H and DOSY NMR experiments were conducted in a 10% DMSO-d$_6$/D$_2$O solution.[27]

To investigate the real inclusion and the geometries of the complexes, we analyzed the complexation-induced shift (CIS) changes of the protons of the guests (**1a** and **2B**) during their inclusion in the hydrophobic cavity of the host molecule (CB[7]). The ^{1}H NMR spectra of the complexes obtained mixing 1 equivalent of **1a** or **2B** with 1 equivalent of the CB[7] were reported in Figure 9.
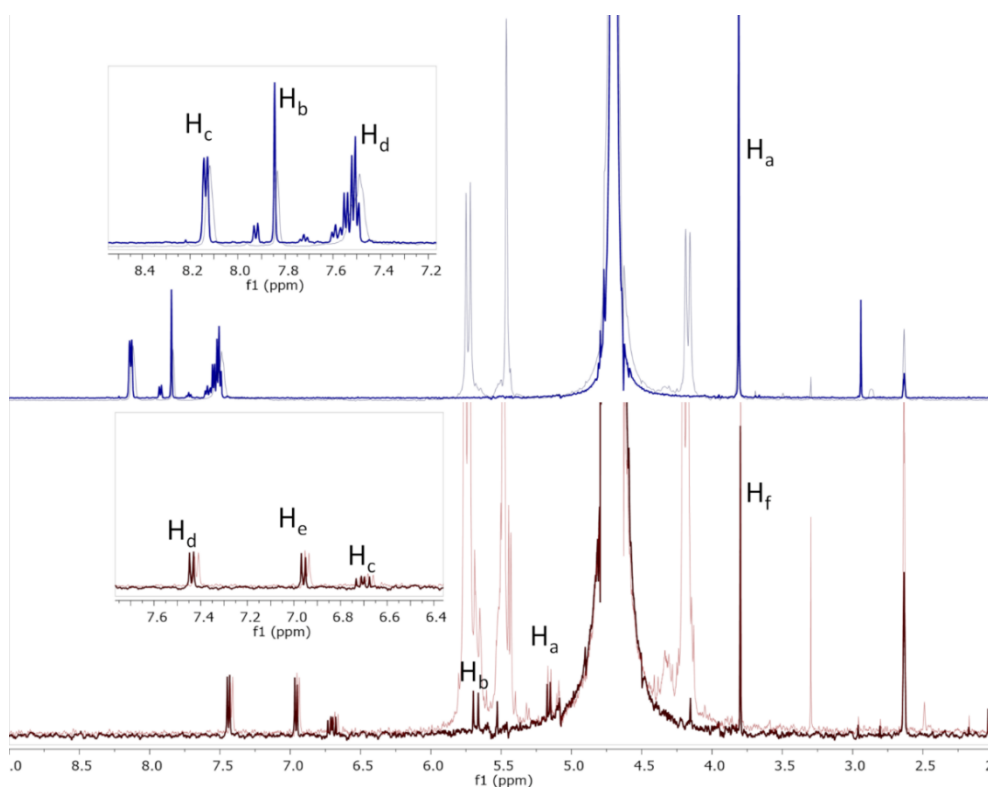

Figure 9. Stacked ^{1}H NMR spectra of **1a** (dark blue), **2B** (dark red), an equimolar mixture of **1a**/[CB7] (light blue), and an equimolar mixture of **2B**/[CB7] (light red).

Upfield shifts ($\Delta\delta < 0$) are observed for guest protons located in the shielding region of the cavity, while guest protons located near the carbonyl oxygens of the portals experience a deshielding effect and then a downfield of the CIS values ($\Delta\delta > 0$). The values of $\Delta\delta$ (Figure 9) clearly indicate that the aromatic ring of both **1a** and **2B** is located in the CB[7] cavity, while the polar end units are located outside of the cavity, near the carbonyl-lined portals. Moreover, the entity of CIS values for compound **2B** indicates that this experience a deeper penetration.

To further unequivocally demonstrate the capability of the CB[7] system to work as a macrocyclic reactor, monitoring of the reaction steps of CB[7] in the presence of **1a** and **2B** was performed using ESI-MS technique. Figure 10 shows the ESI-MS spectra of the solutions containing: CB[7] (a); **2B** and 0.2 eq of CB[7] called **2B**@CB[7] (b); **1a**, **2B** and 0.2 eq of CB[7], called **1a**+**2B**@CB[7] (c); **3aB** and 0.2 eq of CB[7], called **3aB**@CB[7] (d). It can be observed that the ESI-MS spectrum of the CB[7] is essentially constituted of a signal at *m*/*z* 582.25 (Figure 10a), attributable to the CB[7] molecular species, detected as double charged (CB[7]2H$^+$) ions, whereas in Figure 10b, besides the peak of CB[7]2H$^+$ free species, a peak at *m*/*z* 649.96, attributable to the double charged **2B**@CB[7] inclusion complex species, is also observed. Then it can be concluded that the CB[7]'s cavity is able to inside accommodate, in a reversible way, **2B**.

The spectrum of the mixture **1a**, **2B**, and CB[7] (Figure 10c) shows a peak at *m*/*z* 717.30, and the one relative to the **3aB** and CB[7] mixture (Figure 10d) shows a peak at *m*/*z* 717.51. To confirm that the signal at *m*/*z* 717.30 (Figure 10c) is due to the

formation of the cycloadduct inside the cavity, and it is not a simple multi-molecular adduct/complex (**1a**+**2B**+CB[7]), the obtained product **3aB**, recovered employing a liquid-liquid extraction from the solution containing **1a**+**2B**@CB[7], was analyzed through ESI-MS. As expected, the resulting spectrum, reported in Figure 11, consists of a peak at 270.31, assigned to the **3aB** cycloadduct species, detected as a protonated adduct. It can be noticed that the obtained results were almost the same using a higher **2B**/CB[7] molar ratio.
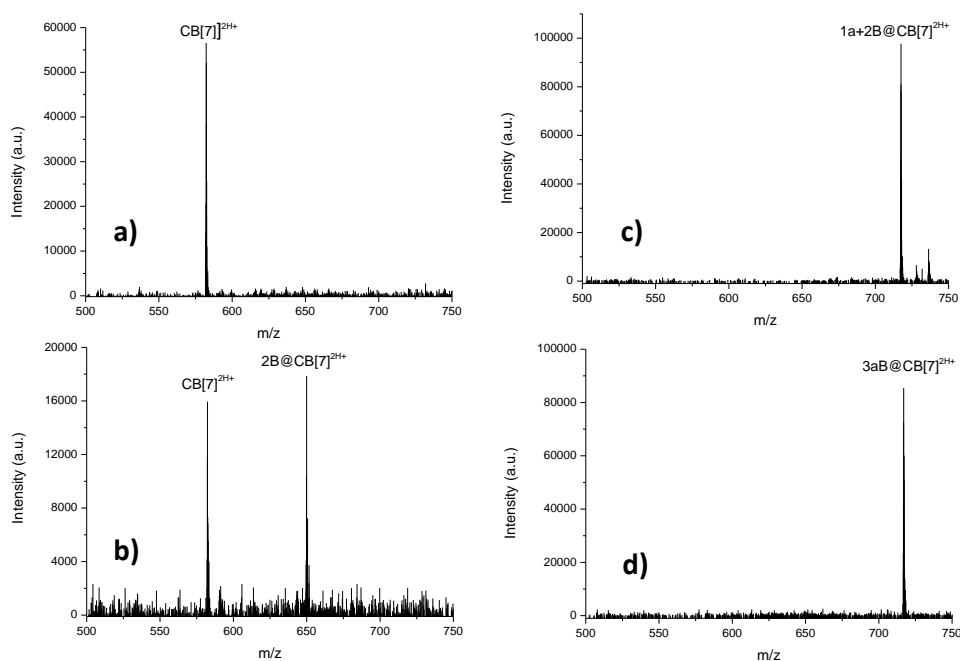

Figure 10. Positive ESI-MS spectra of (a) CB[7], (b) **2B**@CB[7], (c) **1a**+**2B**@CB7, and (d) **3aB**@CB[7].
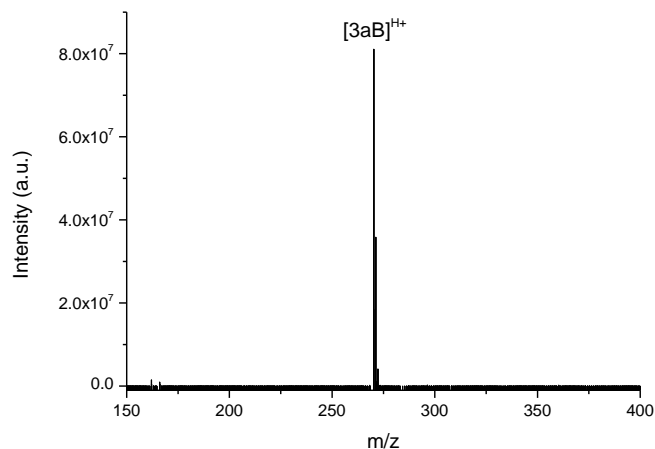
Figure 11. Positive ESI-MS spectrum of **3aB**.

Finally, the catalyst reusability of the CB[7] was studied on the 1,3-DC reactions of nitrones **1a**,**b** with styrene **2aB**. At the end of each reaction, the crude mixture was cooled to room temperature, and the aqueous phase was extracted with ethyl acetate (3 × 5 mL). The reaction products and the eventually remaining reagents and by-products were recovered by the organic phase, whereas to the same aqueous phase, containing the nanoreactor, were again added the reactants, and the mixture was reacted in the same conditions. The results of five experiments clearly demonstrate high catalytic activity during the first three cycles.

1.5 Conclusions

In this first year of my Ph.D., a new synthesis method has been developed that allows us, through the use of molecular models, to increase the yield of CB[7] with respect

to the classical syntheses reported so far. The conversion of imidazole models into magnetic liquid has facilitated the separation of CB[7], which, in general, is long and expensive for time and money. CB[7] has been used as a supramolecular reactor for the synthesis, in some cases, of stereocontrolled isoxazolidine substituted by exploiting the 1,3-dipolar cycloaddition reaction.

The reaction was conducted under "GREEN" conditions using water and microwaves. Furthermore, the catalyst can be recovered and reused in further catalytic cycles.

1.6 Experimental section

General information. All the required chemicals were purchased from Merck and Aldrich Chemical Company. The microwave used was a CEM Discover Microwave Synthesis System. All the reactions conducted under microwave irradiation were performed in a sealed vessel. The reaction temperature was monitored by an external surface sensor. Pre-coated aluminum sheets (silica gel 60 F254, Merck) were used for thin-layer chromatography (TLC), visualizing spots under UV light. Silica gel column chromatography was performed using silica gel 60–120 mesh size. ^{1}H NMR and ^{13}C NMR spectra were recorded on Varian UNITY Inova or a Bruker Avance spectrometer using $CDCl_3$ as a solvent and tetramethylsilane (TMS) as an internal standard, at 200 or 500 MHz for ^{1}H NMR and 125 MHz for ^{13}C NMR.[13]C spectra were ^{1}H decoupled, and multiplicities were determined by the APT pulse sequence.

Chemical shift (δ) values are given in ppm.

Positive ion ESI mass spectra were acquired using a Micromass ZQ mass spectrometer (Waters Corp., Milford, MA, USA). The ESI source potentials were ion-spray voltage 1.35 kV, cone voltage 13 V, source temperature 150 °C, and desolvation temperature 250 °C. The investigated samples, solubilized (concentration of about 10^{-4} M) with a CH_3CN/H_2O (50/50, added with 0.1% of formic acid) mixture, were introduced into the source at a flow rate of 20 μL/min. The mass spectra were elaborated with the ''MassLynx ver. 4.1'' software (from Waters).

Optimized general procedure for the synthesis of CB[7] assisted by imidazole templates

A sealed tube equipped with a stirrer bar was charged with glycoluril (3.5 mmol, 1.0 equiv), respective to imidazole templates (0.5 mmol, 0.14 equiv), and 3 mL of HCl 5M was added. The mixture was stirred at room temperature for 30 minutes to favor the pre-organization of the glycoluril around the template. Then formaldehyde (7.0 mmol, 2 equiv) was added, and the mixture was stirred for 24 h at 100 °C. After completion of the reaction, the mixture was cooled to room temperature, and the formed precipitate, consisting of CB[6], is filtered. The CB[5] and CB[7], left in solution, are precipitated by adding methanol. The precipitate, consisting of CB[5] and imidazole@CB[7], is solubilized in water, and 1.0 eq. of NaPF$_6$ is added, and

the imidazole@CB[7] complex precipitates while the CB[5] remains in solution.[28] The precipitate consisting of imidazole@CB[7] and $(PF_6)^-$ is solubilized in methanol, and 1.0 eq. of NaCl is added and subsequently 1.0 eq. of $FeCl_3$. The addition of $FeCl_3$ allows the formation of the magnetic ionic liquid and the CB[7] precipitates.

Optimized general procedure for the synthesis of CB[7] assisted by 1-admantylamine templates

A sealed tube equipped with a stirrer bar was charged with glycoluril (3.5 mmol, 1.0 equiv), respective to templates (0.5 mmol, 0.14 equiv), and 3 ml of HCl 5M was added. The mixture was stirred at room temperature for 30 minutes to favor the pre-organization of the glycoluril around the template. Then formaldehyde (7.0 mmol, 2 equiv) was added, and the mixture was stirred for 24 h at 100 °C. After completion of the reaction, the mixture was cooled to room temperature, and the formed precipitate, consisting of CB[6], was filtered. The imidazole@CB[7] complex is separated using a small reversed-phase chromatography column using acetonitrile/water (1:1) as eluent.

General procedure for the synthesis of nitrones 1a,b

Nitrones **1a**,**b** were synthesized from commercially available aldehydes (benzaldehyde or *p*-nitrobenzaldehyde) and *N*-methylhydroxylamine hydrochloride

in dichloromethane and using as a base sodium acetate, according to literature.[29] The crude product was purified by silica gel column chromatography using dichloromethane/methanol (9:1) as eluent. The ^{1}H NMR spectra are according to literature.[29]

Optimized general procedure for the synthesis of isoxazolidines 3, 4, 6, and 7

A sealed tube equipped with a stirrer bar was charged with CB[7] (0.05 mmol, 0.10 equiv), respective nitrone (0.5 mmol, 1.0 equiv) and dipolarophile (0.5 mmol, 1.0 equiv). Then water (1 mL) was added, and the mixture was stirred for 4 h at 120 °C under microwave irradiations (80 W). After completion of the reaction, the mixture was cooled to room temperature and extracted with EtOAc (3 × 5 mL), and the catalyst was filtered off and washed with EtOAc (2 × 5 mL); the filtrate was dried over anhydrous Na_2SO_4 and concentrated under reduced pressure. The crude product was purified by silica gel column chromatography using *n*-hexane/ethyl acetate (9.5:0.5) as an eluent. The *cis*/*trans* configuration was assigned according to the literature data.[30]

(3RS,5SR)-2-Methyl-3,5-diphenyl-isoxazolidine (3aA). Light yellow oil; ^{1}H NMR (500 MHz, Chloroform-*d*): 2.42 (1H, ddd, J = 12.4, 9.7, 7.7 Hz, H-4a), 2.70 (3H, s, N-Me), 3.09 (1H, ddd, J = 12.4, 7.7, 6.8 Hz, H-4b), 3.78 (1H, t, J = 8.4 Hz, H-3), 5.26 (1H, t, J = 7.7 Hz, H-5), 7.19−7.33 (4H, m, Ar-H), 7.30−7.39 (4H, m, Ar-H),

7.43−7.50 (2H, m, Ar-H); ^{13}C NMR (50 MHz, Chloroform-*d*): 43.8, 48.7, 73.9, 78.2, 126.0, 127.3, 127.6, 127.7, 128.4, 128.6, 139.1, 143.0; HRMS: *m/z* [M + H]$^+$ calculated for $C_{16}H_{18}NO^+$ 240.1383, found 240.1380.

(3RS,5RS)-2-Methyl-3,5-diphenyl-isoxazolidine (4aA). Light yellow oil; ^{1}H NMR (500 MHz, Chloroform-*d*): 2.62 (1H, ddd, J = 12.5, 8.4, 6.8 Hz, H-4a), 2.71 (3H, s, N-Me), 2.70−2.78 (1H, m, H-4b), 3.72 (1H, s, H-3), 5.25 (1H, dd, J = 8.3, 6.8 Hz, H-5), 7.26−7.33 (2H, m, Ar-H), 7.36 (4H, qd, J = 6.7, 6.2, 3.9 Hz, Ar-H), 7.40−7.46 (4H, m, Ar-H); ^{13}C NMR (50 MHz, Chloroform-*d*): 43.3, 47.8, 73.4, 78.8, 126.6, 127.7, 127.8, 127.9, 128.5, 128.6, 139.3, 140.8; HRMS: *m/z* [M + H] $^+$ calculated for $C_{16}H_{18}NO^+$ 240.1383, found 240.1378.

(3RS,5SR)-5-(4-Methoxyphenyl)-2-methyl-3-phenyl-isoxazolidine (3aB). Light yellow oil; ^{1}H NMR (500 MHz, Chloroform-*d*): 2.42 (1H, ddd, J = 12.5, 9.6, 7.6 Hz, H-4a), 2.70 (3H, s, N-Me), 3.06 (1H, dt, J = 12.5, 7.2 Hz, H-4b), 3.81 (4H, s, H-3, OMe), 5.23 (1H, t, J = 7.6 Hz, H-5), 6.86−6.92 (2H, m, Ar-H), 7.24−7.36 (4H, m, Ar-H), 7.36−7.42 (3H, m, Ar-H); ^{13}C NMR (50 MHz, Chloroform-*d*): 43.3, 43.9, 55.2, 73.0, 79.5, 113.8, 127.5, 127.7, 128.6, 129.1, 138.2, 139.2, 153.6; HRMS: *m/z* [M + H]$^+$ calculated for $C_{17}H_{20}NO_2^+$ 270.1489, found 270.1481.

(3RS,5RS)-5-(4-Methoxyphenyl)-2-methyl-3-phenyl-isoxazolidine (4aB). Light yellow oil; ^{1}H NMR (500 MHz, Chloroform-*d*): 2.56− 2.63 (1H, m, H-4a), 2.63−2.72 (4H, m, N-Me, H-4b), 3.71 (1H, s, H3), 3.81 (3H, s, OMe), 5.17−5.24 (1H, m, H-5), 6.86−6.94 (2H, m, Ar-H), 7.24−7.46 (7H, m, Ar-H); ^{13}C NMR (50 MHz, Chloroform-*d*): 42.6, 43.3, 55.3, 75.6, 78.6, 113.9, 127.5, 128.1, 128.6, 128.7,

138.3,139.4, 152.2; HRMS: *m/z* [M + H]$^+$ calculated for C$_{17}$H$_{20}$NO$_2$$^+$ 270.1489, found 270.1484.

(3RS,5SR)-2-Methyl-5-(4-nitrophenyl)-3-phenyl-isoxazolidine **(3aC)**. Light yellow oil; ^{1}H NMR (500 MHz, Chloroform-*d*): 2.34 (1H, ddd, J = 12.5, 9.6, 6.9 Hz, H-4a), 2.70 (3H, s, N-Me), 3.22 (1H, ddd, J = 12.5, 8.2, 7.2 Hz, H-4b), 3.71−3.78 (1H, m, H-3), 5.32 (1H, dd, J = 8.2, 6.9 Hz, H-5), 7.24−7.35 (5H, m, Ar-H), 7.64 (2H, d, J = 8.5 Hz, Ar-H), 8.18−8.25 (2H, m, Ar-H); ^{13}C NMR (50 MHz, Chloroform-*d*): 43.3, 48.6, 73.9, 76.8, 123.8, 126.4, 127.5, 128.0, 128.7, 138.1, 147.0, 151.7; HRMS: *m/z* [M + H]$^+$ calculated for C$_{16}$H$_{17}$N$_2$O$_3$$^+$ 285.1234, found 285.1228.

(3RS,5RS)-2-Methyl-5-(4-nitrophenyl)-3-phenyl-isoxazolidine **(4aC)**. Light yellow oil; ^{1}H NMR (500 MHz, Chloroform-*d*): 2.56 (1H, dq, J = 13.0, 7.7 Hz, H-4a), 2.74 (3H, s, N-Me), 2.79−2.89 (1H, m, H-4b), 3.73 (1H, s, H-3), 5.32−5.39 (1H, m, H-5), 7.29−7.38 (2H, m, Ar-H), 7.41 (3H, dd, J = 19.2, 7.1 Hz, Ar-H), 7.59 (2H, d, J = 8.6 Hz, Ar-H), 8.20 −8.27 (2H, m, Ar-H); ^{13}C NMR (50 MHz, Chloroform-*d*): 42.9, 48.4, 74.1, 76.5, 124.5, 126.4, 127.6, 127.7, 128.3, 138.1, 147.3, 151.1; HRMS: *m/z* [M + H]$^+$ calculated for C$_{16}$H$_{17}$N$_2$O$_3$$^+$ 285.1234, found 285.1225.

(3RS,5SR)-2-Methyl-3-(4-nitrophenyl)-5-phenyl-isoxazolidine **(3bA)**. Light yellow oil; ^{1}H NMR (500 MHz, Chloroform-*d*): 2.34 (1H, dt, J = 12.6, 8.0 Hz, H-4a), 2.76 (3H, s, N-Me), 3.21 (1H, dt, J = 12.6, 7.6 Hz, H-4b), 3.98 (1H, t, J = 8.0 Hz, H-3), 5.32 (1H, t, J = 7.6 Hz, H-5), 7.28 (1H, d, J = 7.2 Hz, Ar-H), 7.34 (2H, d, J = 7.8 Hz, ArH), 7.40 (2H, d, J = 7.4 Hz, Ar-H), 7.56 (2H, d, J = 8.7 Hz, Ar-H), 8.18

(2H, d, J = 8.7 Hz, Ar-H); ^{13}C NMR (50 MHz, Chloroform-*d*): 44.0, 48.4, 72.5, 78.3, 123.8, 125.9, 127.6, 128.1, 128.5, 141.7, 147.3, 147.8; HRMS: *m/z* [M + H]$^+$ calculated for $C_{16}H_{17}N_2O_3^+$ 285.1234, found 285.1230.

(3RS,5RS)-2-Methyl-3-(4-nitrophenyl)-5-phenyl-isoxazolidine ***(4bA).*** Light yellow oil; ^{1}H NMR (500 MHz, Chloroform-*d*): 2.62− 2.73 (2H, m, H-4a,b), 2.73 (3H, s, N-Me), 3.86 (1H, t, J = 8.3 Hz, H3), 5.24 (1H, t, J = 7.6 Hz, H-5), 7.30−7.45 (5H, m, Ar-H), 7.62 (2H, d, J = 8.7 Hz, Ar-H), 8.20−8.26 (2H, m, Ar-H); ^{13}C NMR (50 MHz, Chloroform-*d*): 43.6, 47.8, 72.4, 79.0, 123.9, 126.5, 128.1, 128.4, 128.6, 140.0, 147.4, 147.5; HRMS: *m/z* [M + H]$^+$ calculated for $C_{16}H_{17}N_2O_3^+$ 285.1234, found 285.1232.

(3RS,5SR)-5-(4-Methoxyphenyl)-2-methyl-3-(4-nitrophenyl)-isoxazolidine (3bB). Light yellow oil; ^{1}H NMR (500 MHz, Chloroform-*d*): 2.33 (1H, ddd, J = 12.6, 8.5, 7.6 Hz, H-4a), 2.76 (3H, s, N-Me), 3.16 (1H, dt, J = 12.6, 7.6 Hz, H-4b), 3.80 (3H, s, OMe), 4.00 (1H, t, J = 8.0 Hz, H-3), 5.29 (1H, t, J = 7.6 Hz, H-5), 6.85−6.91 (2H, m, ArH), 7.31 (2H, d, J = 8.5 Hz, Ar-H), 7.55−7.61 (2H, m, Ar-H), 8.16− 8.22 (2H, m, Ar-H); ^{13}C NMR (50 MHz, Chloroform-*d*): 44.2, 48.3, 55.3, 72.5, 78.2, 114.0, 123.9, 127.5, 128.1, 133.3, 147.4, 148.1, 159.2; HRMS: *m/z* [M + H]$^+$ calculated for $C_{17}H_{19}N_2O_4^+$ 315.1339, found 315.1333.

(3RS,5RS)-5-(4-Methoxyphenyl)-2-methyl-3-(4-nitrophenyl)-isoxazolidine (4bB). Light yellow oil; ^{1}H NMR (500 MHz, Chloroform-*d*): 2.55−2.72 (2H, m, H-4a,b), 2.71 (3H, s, N-Me), 3.82 (3H, s, OMe), 3.85 (1H, t, J = 8.3 Hz, H-3), 5.19 (1H, t, J = 7.6 Hz, H-5), 6.91 (2H, d, J = 8.6 Hz, Ar-H), 7.35 (2H, d, J = 8.6 Hz, Ar-H), 7.62

(2H, d, J = 8.6 Hz, Ar-H), 8.23 (2H, d, J = 8.6 Hz, Ar-H); ^{13}C NMR (50 MHz, Chloroform-*d*): 43.9, 47.3, 51.6, 71.6, 77.4, 112.0, 122.1, 126.9, 130.0, 133.2, 146.1, 149.0, 161.2; HRMS: *m/z* [M + H]$^+$ calculated C$_{17}$H$_{19}$N$_2$O$_4$$^+$ 315.1339, found 315.1329.

(3RS,5SR)-2-Methyl-3,5-bis(4-nitrophenyl)-isoxazolidine (3bC). Light yellow sticky oil; ^{1}H NMR (500 MHz, Chloroform-*d*): 2.23− 2.33 (1H, m, H-4a), 2.74 (3H, s, N-Me), 3.27−3.37 (1H, m, H-4b), 3.88−3.96 (1H, m, H-3), 5.38 (1H, dd, J = 8.2, 6.7 Hz, H-5), 7.47− 7.52 (2H, m, Ar-H), 7.57−7.64 (2H, m, Ar-H), 8.15−8.25 (4H, m, ArH); ^{13}C NMR (50 MHz, Chloroform-*d*): 43.5, 48.5, 72.7, 76.9, 123.8, 123.9, 126.4, 128.2, 146.4, 147.1, 147.5, 150.6; HRMS: *m/z* [M + H]$^+$ calculated for C$_{16}$H$_{16}$N$_3$O$_5$$^+$ 330.1084, found 330.1077.

(3RS,5RS)-2-Methyl-3,5-bis(4-nitrophenyl)-isoxazolidine (4bC). Light yellow sticky oil; ^{1}H NMR (500 MHz, Chloroform-*d*): 2.63 (1H, ddd, J = 12.6, 8.5, 6.8 Hz, H-4a), 2.70−2.80 (1H, m, H-4b), 2.75 (3H, s, N-Me) 3.84−3.88 (1H, m, H-3), 5.29−5.36 (1H, m, H-5), 7.56−7.64 (4H, m, Ar-H), 8.22−8.27 (4H, m, Ar-H); ^{13}C NMR (50 MHz, Chloroform-*d*): 43.6, 47.7, 72.0, 75.4, 123.8, 124.1, 126.9, 128.4, 146.6, 147.5, 147.7, 147.8; HRMS: *m/z* [M + H]$^+$ calculated for C$_{16}$H$_{16}$N$_3$O$_5$$^+$ 330.1084, found 330.1081.

Ethyl (3RS,4SR,5SR)-2-Methyl-3,5-diphenyl-isoxazolidine-4carboxylate (6aA). Light yellow sticky foam; ^{1}H NMR (500 MHz, Chloroform-*d*): 1.20 (3H, t, J = 7.1 Hz), 2.73 (3H, s, N-Me), 3.50 (1H, dd, J = 8.6, 6.3 Hz, H-4), 4.05 (1H, d, J = 8.6 Hz, H-3), 4.17 (2H, q, J = 7.1 Hz), 5.42 (1H, d, J = 6.3 Hz, H-5), 7.27−7.38 (6H, m,

ArH), 7.38 (2H, d, J = 7.5 Hz, Ar-H), 7.52 (2H, d, J = 7.3 Hz, Ar-H); ^{13}C NMR (50 MHz, Chloroform-*d*): 14.1, 43.4, 61.2, 65.8, 76.8, 80.7, 125.9, 127.6, 127.8, 128.1, 128.5, 128.7, 137.7, 171.4; HRMS: *m/z* [M + H]$^+$ calculated for $C_{19}H_{22}NO_3^+$ 312.1594, found 312.1588.

Ethyl (3RS,4SR,5SR)-5-(4-Methoxyphenyl)-2-methyl-3-phenyl-isoxazolidine-4-carboxylate (6aB). Light yellow sticky foam; ^{1}H NMR (500 MHz, Chloroform-*d*): 1.19 (3H, t, J = 7.1 Hz), 2.72 (3H, s, NMe), 3.47 (1H, dd, J = 8.6, 6.6 Hz, H-4), 3.81 (3H, s, OMe), 4.07 (1H, d, J = 8.6 Hz, H-3), 4.15 (2H, q, J = 7.1 Hz), 5.37 (1H, d, J = 6.6 Hz, H-5), 6.87−6.93 (2H, m, Ar-H), 7.24−7.46 (8H, m, Ar-H); ^{13}C NMR (50 MHz, Chloroform-*d*): 14.1, 43.5, 55.3, 61.2, 65.7, 80.7, 113.9,

127.4, 127.7, 128.1, 128.7, 133.7, 137.9, 159.1, 171.4; HRMS: *m/z* [M + H]$^+$ calculated for $C_{20}H_{24}NO_4^+$ 342.1700, found 342.1687.

Ethyl (3RS,4SR,5SR)-2-Methyl-5-(4-nitrophenyl)-3-phenyl-isoxazolidine-4-carboxylate (6aC). Light yellow sticky foam; ^{1}H NMR (500 MHz, Chloroform-*d*): 1.25 (3H, t, J = 7.1 Hz), 2.71 (3H, s, NMe), 3.42 (1H, dd, J = 8.8, 5.6 Hz, H-4), 4.00 (1H, d, J = 8.8 Hz, H-3), 4.21 (2H, q, J = 7.1 Hz), 5.48 (1H, d, J = 5.6 Hz, H-5), 7.24−7.33 (5H, m, Ar-H), 7.72 (2H, d, J = 8.4 Hz, Ar-H), 8.21−8.27 (2H, m, ArH); ^{13}C NMR (50 MHz, Chloroform-*d*): 14.1, 43.0, 61.6, 65.7, 76.7, 79.4, 123.9, 126.5, 127.8, 128.4, 128.8, 131.0, 136.8, 150.4, 170.9; HRMS: *m/z* [M + H]$^+$ calculated for $C_{19}H_{21}N_2O_5^+$ 357.1445, found 357.1436.

Ethyl (3RS,4SR,5SR)-2-Methyl-3-(4-nitrophenyl)-5-phenyl-isoxazolidine-4-carboxylate (6bA). Light yellow sticky foam; ^{1}H NMR (500 MHz, Chloroform-*d*):

1.25 (3H, t, J = 7.1 Hz), 2.77 (3H, s, NMe), 3.42 (1H, dd, J = 8.0, 6.3 Hz, H-4), 4.22 (3H, CH2, H-3), 5.48 (1H, d, J = 6.3 Hz, H-5), 7.28−7.41 (3H, m, Ar-H), 7.47 (2H, ddd, J = 8.2, 1.3, 0.6 Hz, Ar-H), 7.55−7.61 (2H, m, Ar-H), 8.16−8.22 (2H, m, Ar-H); ^{13}C NMR (50 MHz, Chloroform-d): 14.1, 43.6, 61.6, 65.9, 75.4, 80.8, 123.9, 125.8, 127.9, 128.5, 128.6, 141.0, 146.1, 147.6, 170.8; HRMS: m/z [M + H]$^+$ calculated for $C_{19}H_{21}N_2O_5^+$ 357.1445, found 357.1442.

Ethyl (3RS,4SR,5SR)-5-(4-Methoxyphenyl)-2-methyl-3-(4-nitrophenyl)-isoxazolidine-4-carboxylate (6bB). Light yellow sticky foam; ^{1}H NMR (500 MHz, Chloroform-d): 1.24 (3H, t, J = 7.1 Hz), 2.78 (3H, s, N-Me), 3.39 (1H, dd, J = 7.9, 6.6 Hz, H-4), 3.81 (3H, s, OMe), 4.20 (2H, d, J = 7.1 Hz), 4.26 (1H, d, J = 7.9 Hz, H-3), 5.44 (1H, d, J = 6.6 Hz, H-5), 6.87−6.93 (2H, m, Ar-H), 7.34−7.40 (2H, m, Ar-H), 7.57−7.63 (2H, m, Ar-H), 8.17−8.23 (2H, m, Ar-H)); ^{13}C NMR (126 MHz, Chloroform-d): 14.15, 43.8, 55.3, 61.6, 65.9, 75.3, 80.8, 114.0, 123.9, 127.4, 128.4, 132.5, 146.5, 147.7, 159.4, 170.9; HRMS: m/z [M + H]$^+$ calculated for $C_{20}H_{23}N_2O_6^+$ 387.1551, found 387.1547.

Ethyl (3RS,4SR,5SR)-2-Methyl-3,5-bis(4-nitrophenyl)-isoxazolidine-4-carboxylate (6bC). Light yellow sticky foam; ^{1}H NMR (500 MHz, Chloroform-d): 1.29 (3H, t, J = 7.1 Hz), 2.75 (3H, s, N-Me), 3.37 (1H, dd, J = 8.5, 5.6 Hz, H-4), 4.17 (1H, d, J = 8.5 Hz, H-3), 4.26 (2H, q, J = 7.1 Hz), 5.54 (1H, d, J = 5.6 Hz, H-5), 7.52 (2H, d, J = 8.8 Hz, Ar-H), 7.70 (2H, dd, J = 8.9, 0.7 Hz, Ar-H), 8.18 (2H, d, J = 8.9 Hz, Ar-H), 8.25 (2H, d, J = 8.9 Hz, Ar-H); ^{13}C NMR (50 MHz, Chloroform-d): 14.1, 43.1, 62.0, 65.7, 75.3, 79.4, 123.9, 124.0, 126.4, 128.6, 144.8, 147.3, 147.8, 149.5, 170.2;

HRMS: *m/z* [M + H]$^+$ calculated for $C_{19}H_{20}N_3O_7^+$ 402.1296, found 402.1292.

Chapter 2. Tetrahedral capsule: synthesis and applications

2.1 Introduction

The purpose of a supramolecular chemist is to mimic biological systems, where reactions and complex reactions with high non-catalyzed energy barriers proceed effectively with excellent selectivity. Effective control of enzymes on substrates is achieved by isolating substrates in the active sites. Therefore, it is evident to make parallelisms between the active enzyme sites and the micro-environments of the supramolecular hosts since both are based on molecular recognition, substrate isolation, and conformational control. Now, in the literature, there is a wide range of supramolecular systems that try to mimic the work carried out by enzymes, and various types of building blocks are formed that go to determine a wide range of cavities that can be used for catalysis.[31]

In fact, the purpose of this project is to mimic natural systems, using a tetrahedral capsule already present in the literature in order to use it as a catalyst in water. The supramolecular capsule in question was developed by Prof. Raymond et *al*. and, so far, it has been used to catalyze cyclization reactions, stabilize some substrates in water, and more.[31] Hence, the idea of using it to catalyze 1,3-dipolar cycloadditions and reductive aminations, using in both cases water as a solvent, and subsequently developing a new capsule and comparing the obtained results.

The supramolecular system is self-assembled by six bis-bidentate ligands and four metal ions to form a cage with metal atoms at the tetrahedron vertices. As

demonstrated by the crystallographically obtained geometric parameters and its T symmetry, the tetrahedron has ligands that cross the six edges. The ligand is *N*,*N'*-(naphthalene-1,5-diyl)bis(2,3-dihydroxybenzamide), consisting of a naphthalene core and two catechols groups capable of complexing the Ga^{3+} that constitute the vertices of the tetrahedron (Figure 12).[31]
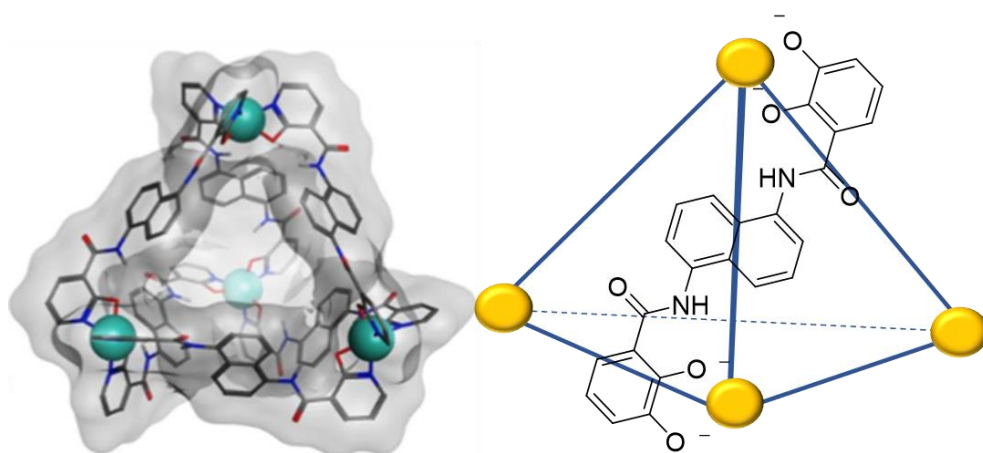

Figure 12. Tetrahedral capsule.

The stoichiometry of the capsule is $[K_{12}(Ga_4L_6)]$, and since each Ga(III)-triscateculate has a formal trianionic charge, it is overall dodecanoic. The host is soluble in water and polar organic solvents by this high charge. In terms of size, the host is within the nanoscale regime, measuring about 13 Å from vertex to vertex.[31] This second part of the first year of the Ph.D. period focused on synthesizing the ligand, the assembly of the capsule, and its use to synthesize some nitrones in water, substrates that can subsequently be used for cycloadditions.

2.2 Results and Discussion

For the ligand synthesis, the building blocks used were 2,3-dihydroxybenzoic acid and naphthalene-1,5-diamine. Initially, a direct coupling between acid and diamine was tried using different coupling agents, attempting to find a different method from the one present in the literature, but the reaction yield was low. Therefore, based on the literature, the hydroxyl groups of the acid were protected by methylation, also obtaining the acid ester. Subsequently, after hydrolyzing the methylated ester, methylated acid was transformed into 2,3-dimethoxybenzoyl chloride.

The coupling with the diamine was carried out at this point, obtaining the ligand with the methylated hydroxyl groups, which were demethylated with BBr_3. The diagram of the ligand synthesis is shown below (Scheme 2).[32]
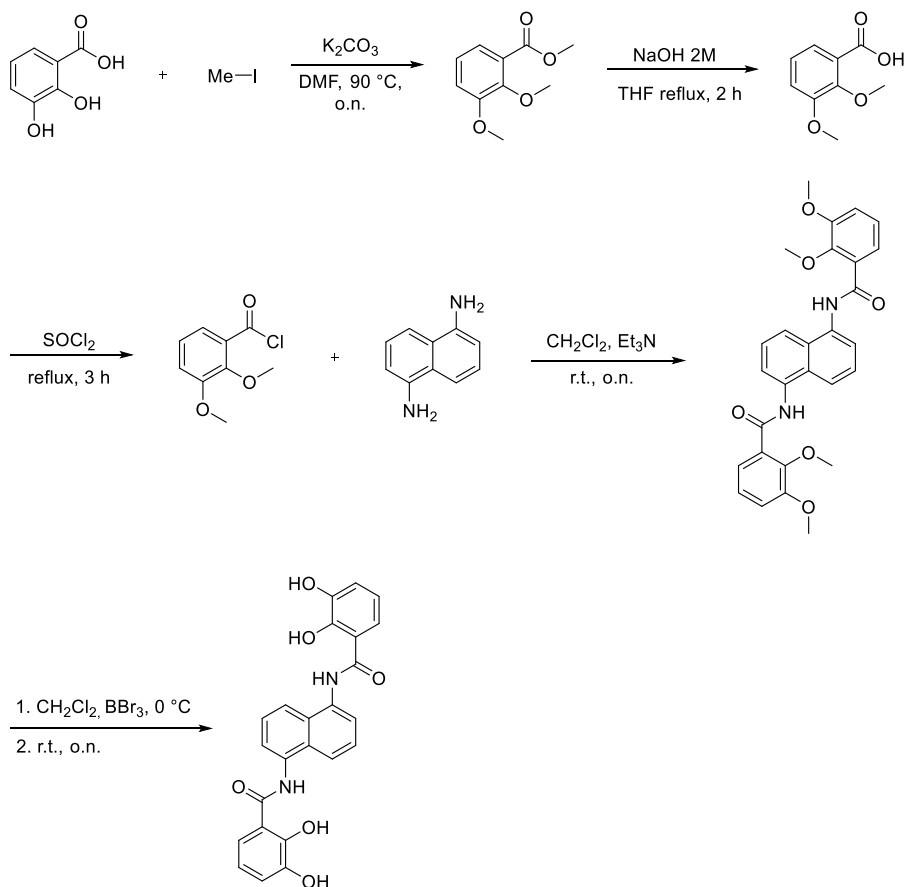
Scheme 2. Ligand synthesis procedure.

Once the synthesis of the ligand was finalized, the capsule (**1**) was assembled following the methodology described in the literature gallium(III) acetylacetonate as a precursor.[32]

To verify that the assembly had taken place, an ammonium salt was used, as reported in the literature.[33] This method is exploited because it has been demonstrated by NMR spectroscopy that these capsules have a high affinity for cations; in fact, when the capsule forms a complex with the ammonium salt a shift to high fields of the

signals related to protons occurs of salt. This is due to the interaction that occurs between host and guest, which is of the π-cation type, because inside the cavity there is a strong electronic cloud due to the aromatic systems that make up the ligands (Figure 13).
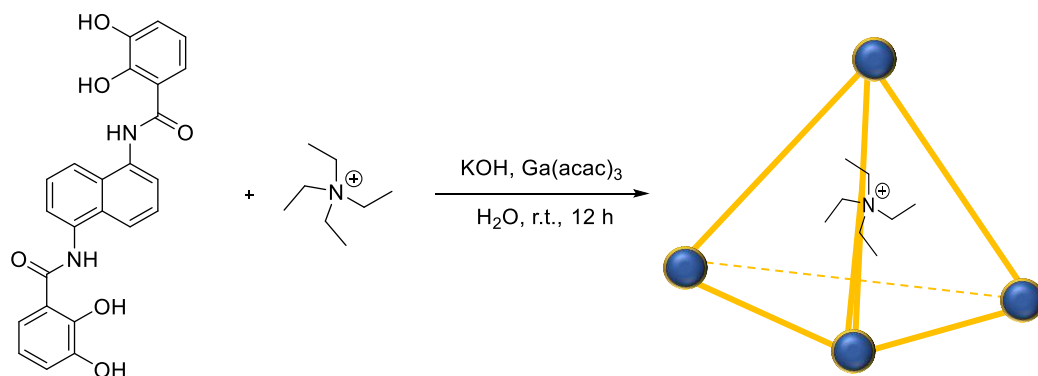

Figure 13. Capsule assembly with the tetraethylammonium salt.

To demonstrate the formation of the complex, we report a DOSY experiment, in which we see the signals of the ammonium salt at negative ppm values and that the signals of the capsule and the salt have the same diffusion coefficient, underlining the formation of the complex (Figure 14).
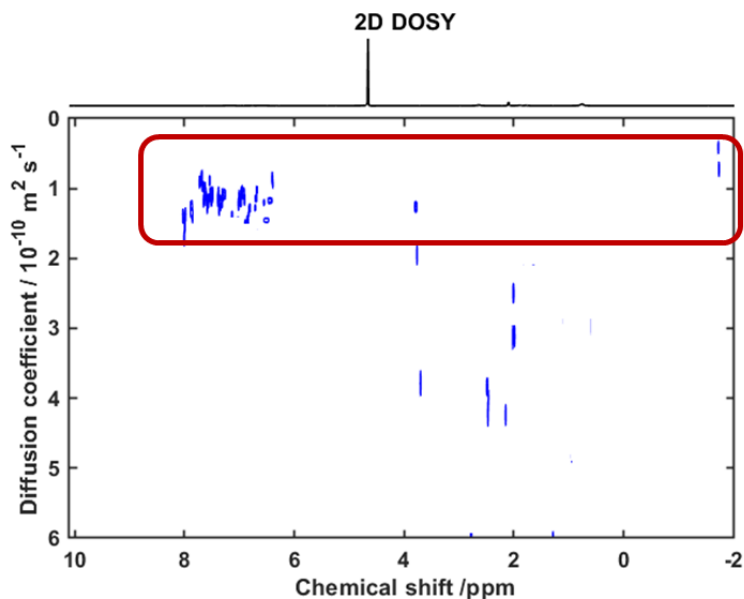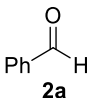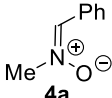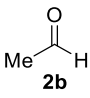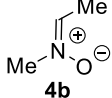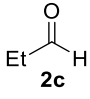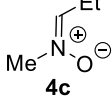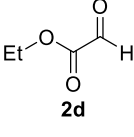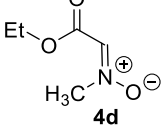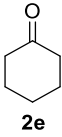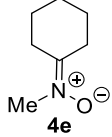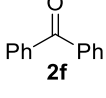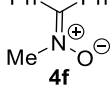
Figure 14. DOSY experiment of ammoniumsalt@capsule.

It was possible to synthesize six different nitrones, starting from aldehydes and ketones, taking advantage of the capsule's hydrophobic cavity. The advantage in using the capsule as a nanoreactor was the easy separation of the nitrones obtained by extraction with a green classified organic solvent.[34,35] On the contrary, the traditional methodologies for synthesizing these substrates foresee the use of chromatographic separation.[36] Furthermore, for some substrates, the yields were obtained with shorter reaction times and were higher than those reported in the literature.[37]

To optimize the reaction conditions, the synthesis of *N*-methyl-1-phenylmethanimine oxide (**4a**) was used as a model reaction (Table 6). The amounts of benzaldehyde (**1**) and *N*-methylhydroxylamine hydrochloride (**2**) have been varied

and, subsequently, the quantity of capsule from 1 eq. to 0.1 eq. Using a catalytic quantity of capsule (Entry 7) allowed us to obtain good reaction yields in shorter times.[36]

Table 6. Optimization of the reaction conditions between aldehyde **1** and *N*-methylhydroxylamine **2**.[a]

Entry	2a (eq.)	3 (eq.)	Capsule 1 (eq.)	Yield (%)
1	1	1	—	Traces
2	1	1	1.0	74
3	2	1	1.0	73
4	3	1	1.0	75
5	1	3	1.0	73
6	1	1	0.5	71
7	1	1	0.2	70
8	1	1	0.1	58

[a]All reactions were conducted with an equimolar amount of $NaHCO_3$ with respect to **3**.

With the optimized reaction conditions, the catalytic capacity of the capsule was tested using five other substrates, including aldehydes and ketones. Table 7 shows the reaction times and the yields obtained with respect to those reported in the literature. In addition, a never-reported nitrone has been synthesized from acetaldehyde (Table 7, Entry 2).

Table 7. Reaction times and yields obtained with the capsule and reported in the literature.[a]

Entry	Substrate	Reaction time (h)	Product	Yield (%)	Reaction time Lit. (h)	Yield (%) Lit.
1	Ph–CHO **2a**	12	**4a** (Me–N⊕(O⊖)=CH–Ph)	70	48	80[36]
2	Me–CHO **2b**	1	**4b** (Me–N⊕(O⊖)=CH–Me)	83	1	85 (this work)[b]
3	Et–CHO **2c**	3	**4c** (Me–N⊕(O⊖)=CH–Et)	79	48	56[36]
4	EtO–CO–CHO **2d**	12	**4d** (H₃C–N⊕(O⊖)=CH–CO–OEt)	70	12	75[38]
5	cyclohexanone **2e**	6	**4e** (Me–N⊕(O⊖)=cyclohexylidene)	75	10 min	68[39]
6	Ph–CO–Ph **2f**	12	**4f** (Me–N⊕(O⊖)=C(Ph)Ph)	39	7	65[40]

[a]All the reactions were conducted in water at room temperature with 0.2 eq. of the capsule and 1.0 eq. of NaHCO₃. [b]The *E*/*Z* configuration was assigned via 1D NOESY (see experimental section). All products were characterized by ^{1}H and ^{13}C NMR (see experimental section).

To examine the inclusion of the studied substrates (**2a** and **4a**) inside the catalytic cavity and estimate the association constant K_a at the same time, we performed a series of DOSY experiments on free capsule **1**, compounds **2a** and **4a**, and the **2a@1**

and **4a@1**complexes (Figure 15, and in experimental section Figures 16–21). Because the systems investigated in this study are under fast equilibrium between free and complexed states on the NMR time scale, the observed diffusion coefficient (D_{obs}) measured in the experiment is the weighted average of those of the free and complexed molecules:[27,41]

$$D_{obs} = x_{HG}\, D_{bound} + (1 - x_{HG})\, D_{free} \qquad (1)$$

D_{free} and D_{bound} are the diffusion coefficients of free and bound guest molecules, respectively, whereas the x_{HG} refers to the molar fraction of the host-guest (HG) complex.
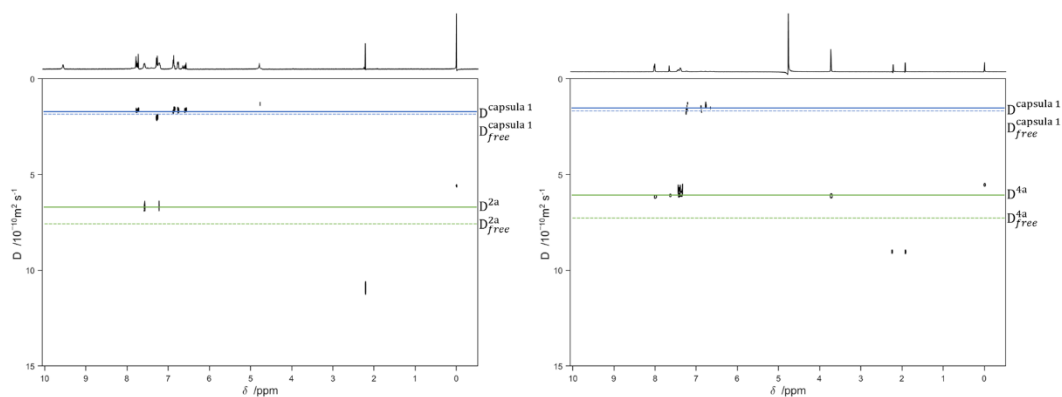
Figure 15. Left) 2D DOSY-NMR measurements on the D2O solution of 2a (0.025 M) and capsule 1 (0.005 M) mixture. Right) 2D DOSY-NMR measurements on the D2O solution of 4a (0.025 M) and capsule 1 (0.005 M) mixture. The horizontal axis represents the chemical shifts, whereas the vertical axis the diffusion coefficients; the black spots are the resonances of the water solution of the inclusion complex spread in the second dimension according to their measured diffusion coefficient.

The solid lines green and purple in Figure 15 represent the diffusion observed for **2a**

or **4a** $\left(D_{obs}^{2a \text{ or } 4a}\right)$ and capsule **1** $\left(D_{obs}^{capsule \, 1}\right)$, respectively, while the dashed lines are the diffusion coefficients of free **2a** or **4a** $\left(D_{free}^{2a \text{ or } 4a}\right)$ and free capsule **1** $\left(D_{free}^{capsule \, 1}\right)$.

The quantitative estimation of the complex formation constant is based on the degree to which the solid lines (complexed molecules) are displaced from their corresponding dashed (free molecules).

The results demonstrate that the diffusion coefficients for both the molecules **2a** and **4a** diminished from 7.42 to 6.82×10^{-10} m^2/s and from 6.77 to 6.00×10^{-10} m^2/s for molecules **2a** and **4a**, respectively (Table 8), and this is indicative of a complexation within the cavity of molecule **1**.

Table 8. Diffusion coefficients (D) of **1**, **2a**, **3**, **4a**, **1@2a** and **1@4a**, complex molar fraction, and **1@2a**/**1@4a** association constant (K_a).

Compound	D (10^{-10} m^{2}s^{-1})	Complex molar fraction (%)	K_a (M^{-1})
1	2.16	—	—
2a	7.42	—	—
3	9.80	—	—
4a	6.77	—	—
1@4a	6.00	16.70	243.00
1@2a	6.86	10.64	50.88

The association constant K_a can be calculated exploiting a single-point procedure on the assumption of known x_{HG} (**2a** or **4a**) (Equation 2).[42,43] This procedure assumes that the diffusion coefficient of the host-guest complex (**2a@1** and **4a@1** complexes) is the same as that of the host molecule (capsule **1**). This is because the host molecule

is usually very much larger than the guest, so it seems reasonable to assume that the diffusion coefficient of the host-guest complex is the same as that of the host molecule (a measurable quantity).

$$K_a = x_{HG}/[(1 - x_{HG}) ([H] - x_{HG} [G])] \tag{2}$$

In Equation 2, [H] and [G] are the total concentration of the host and guest, respectively. The diffusion coefficients (D) measured in D_2O and the respective association constants are reported in Table 3. As pointed out by the DOSY experiments, both the molecules **2a** and **4a** can be included inside the hydrophobic cavity of capsule **1**. Moreover, product **4a** is able to achieve a stronger interaction with the host molecule; this agrees with the experimental result that the higher the amount of capsule, the higher the yield of the reaction.

2.3 Conclusions

In conclusion, we have reported the first example of nitrone synthesis using this tetrahedral capsule as a nanoreactor in water. We have also synthesized a new nitrone, starting from acetaldehyde, using the capsule in water. The synthesis in a nanoconfined space has allowed us to reduce the reaction times in some cases and easily separate the nitrones from the reaction mix, obtaining reaction yields equal or comparable to those obtained with classical methodologies. The environmentally friendly approach underlying this work can be extended, in a relatively simple way, to other reactions that use various

types of macrocyclic hosts, suitably designed and widely used in supramolecular chemistry.

2.4 Experimental section

General information. All the required chemicals were purchased from Merck. The synthesis of the capsule building blocks and assembly were carried out as reported in the literature and subsequently characterized by NMR.[32] Pre-coated aluminum sheets (silica gel 60 F254, Merck) were used for thin-layer chromatography (TLC), and spots were visualized under UV light. Silica gel column chromatography was performed using silica gel 60–120 mesh size. ^{1}H and ^{13}C NMR spectra were recorded, at 300 K, on Varian UNITY Inova using $CDCl_3$ and D_2O as solvents, at 500 MHz for ^{1}H NMR and 125 MHz for ^{13}C NMR. ^{13}C spectra were ^{1}H-decoupled, and the APT pulse sequence determined multiplicities. Chemical shift (δ) values are given in ppm. Diffusion ordered spectroscopy (DOSY) experiments were performed using the DgcsteSL_cc (DOSY gradient compensated stimulated echo with spin-lock and convection compensation) HR-DOSY sequence. The pulsed gradient range amplitudes were 0.1067–0.5334 T m^{-1}, at a diffusion time of 0.06 s. The processing program (DOSY macro in the Varian instrument) was run with the data transformed using fn = 32 K and lb = 0.3. All the experiments were acquired at 300 K.

General procedure for the synthesis of nitrones 4a–e with capsule

Nitrones were synthesized from commercially available aldehydes and ketones (1.0 eq.), *N*-methylhydroxylamine hydrochloride (50.0 mg, 0.598 mmol, 1.0 eq.), NaHCO$_3$ (50.3 mg, 0.598 mmol, 1.0 eq.), and capsule **1** (396.0 mg, 0.199 mmol, 0.2 eq.) in water (5 mL) at room temperature. The products were extracted with EtOAc (3 × 10 mL). The *E*/*Z* configuration of nitrones **4a**,**c**,**d** was assigned according to the literature data.[36,38] All products were characterized by ^{1}H and ^{13}C NMR.

(*Z*)-*N*-methyl-1-phenylmethanimine oxide (**4a**)

White solid. ^{1}H NMR (500 MHz, Chloroform-*d*): δ = 8.35 – 8.11 (m, 2H), 7.69–7.33 (m, 4H), 3.87 (s, 3H); ^{13}C NMR (126 MHz, Chloroform-*d*): δ = 134.42, 130.45, 130.33, 129.64, 128.93, 128.43, 128.14, 54.24.

(*Z*)-isomer of *N*-methylethanimine oxide (**4b**)

Light brown oil. ^{1}H NMR (500 MHz, D$_2$O): δ = 7.36 (q, *J* = 5.5 Hz, 1H), 3.71 (s, 3H), 2.04 (d, *J* = 5.8 Hz, 3H); ^{13}C NMR (126 MHz, D$_2$O): δ =145.56, 50.82, 12.55.

(*Z*)-*N*-methylpropan-1-imine oxide (**4c**)

Colourless oil. ^{1}H NMR (500 MHz, D$_2$O): δ = 7.26 (t, *J* = 5.9 Hz, 1H), 3.67 (s, 3H), 2.48 – 2.41 (m, 2H), 1.12 (t, *J* = 7.7 Hz, 3H); ^{13}C NMR (126 MHz, D$_2$O): δ = 150.79, 50.83, 20.28, 8.65.

(*E*)-2-ethoxy-*N*-methyl-2-oxoethan-1-imine oxide (**4d**)

Yellow oil. ^{1}H NMR (500 MHz, Chloroform-*d*): δ = 7.24 (s, 1H), 4.26 (dt, *J* = 14.3, 5.7 Hz, 3H), 4.18 (s, 3H), 1.32 (t, *J* = 7.1 Hz, 2H); ^{13}C NMR (126 MHz, Chloroform-*d*): δ = 161.11, 127.70, 61.43, 52.26, 14.17.

N-methylcyclohexanimine oxide (**4e**)

Light brown oil. ^{1}H NMR (500 MHz, Chloroform-*d*): δ = 3.70 (s, 3H), 2.76 (t, *J* = 6.5 Hz, 1H), 2.71 (s, 1H), 2.64 (s, 1H), 2.47 (t, *J* = 6.4 Hz, 2H), 2.14 (d, *J* = 21.8 Hz, 1H), 1.69 (dt, *J* = 12.7, 6.3 Hz, 2H), 1.58 (ddd, *J* = 11.4, 7.2, 4.6 Hz, 2H); ^{13}C NMR (126 MHz, Chloroform-*d*): δ = 150.11, 47.22, 29.99, 26.72, 25.25, 24.50.

N-methyl-1,1-diphenylmethanimine oxide (**4f**)

Pale yellow solid. ^{1}H NMR (500 MHz, Chloroform-*d*): δ = 7.84 – 7.76 (m, 3H), 7.63 – 7.55 (m, 1H), 7.54 – 7.46 (m, 3H), 4.02 (s, 3H); ^{13}C NMR (126 MHz, Chloroform-*d*): δ = 137.85, 132.59, 130.46, 130.20, 128.42, 42.46.

Classical method for the synthesis of nitrones 4a–e

Into a 10 mL round flask containing dichloromethane (6 mL), at 0 °C under N_2 atmosphere, were added aldehyde or ketone (500 mg, 11.35 mmol, 5 eq.), *N*-methylhydroxylamine hydrochloride (189.60 mg, 2.27 mmol, 1 eq), $NaHCO_3$ (190.68 mg, 2.27 mmol, 1 eq.) and Na_2SO_4 (322.43 mg, 2.27 mmol, 1 eq.), and the solution was stirred for 1 h. The crude product was purified by silica gel column chromatography using dichloromethane/methanol (9:1) as eluent to give the corresponding nitrones.
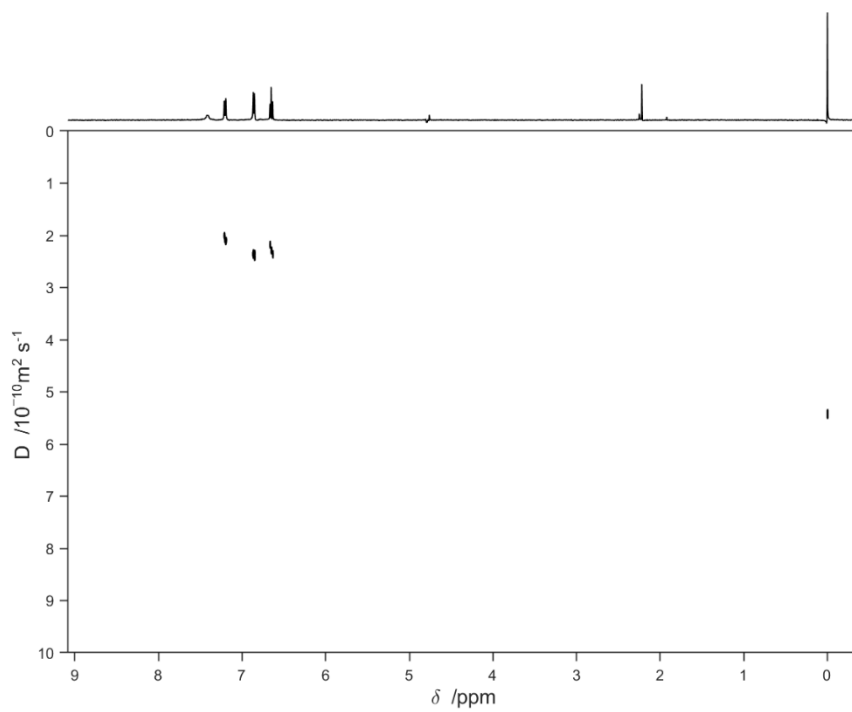
DOSY spectra

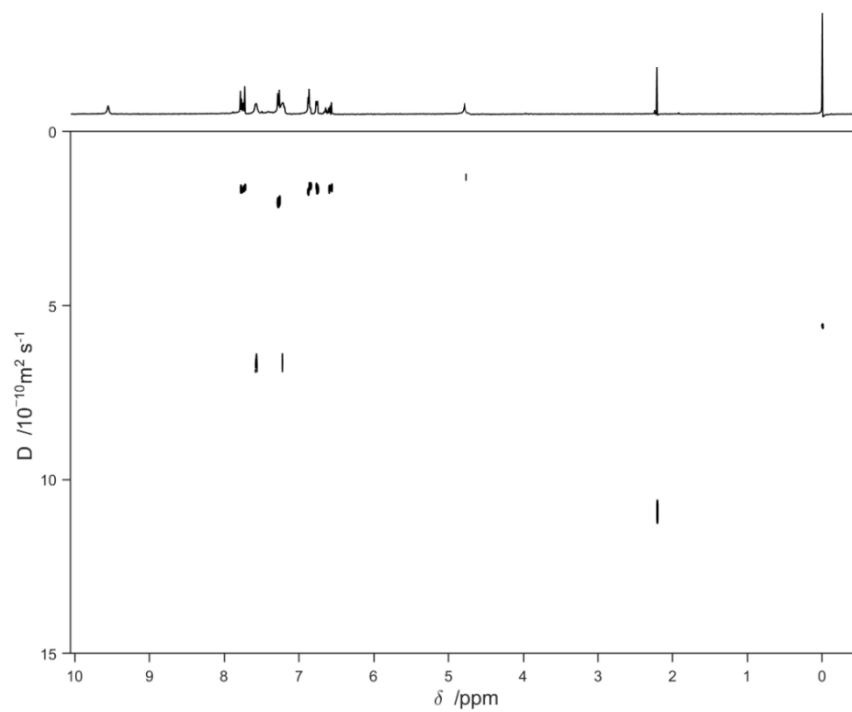**Figure 16**. DOSY spectrum of capsule **1**.
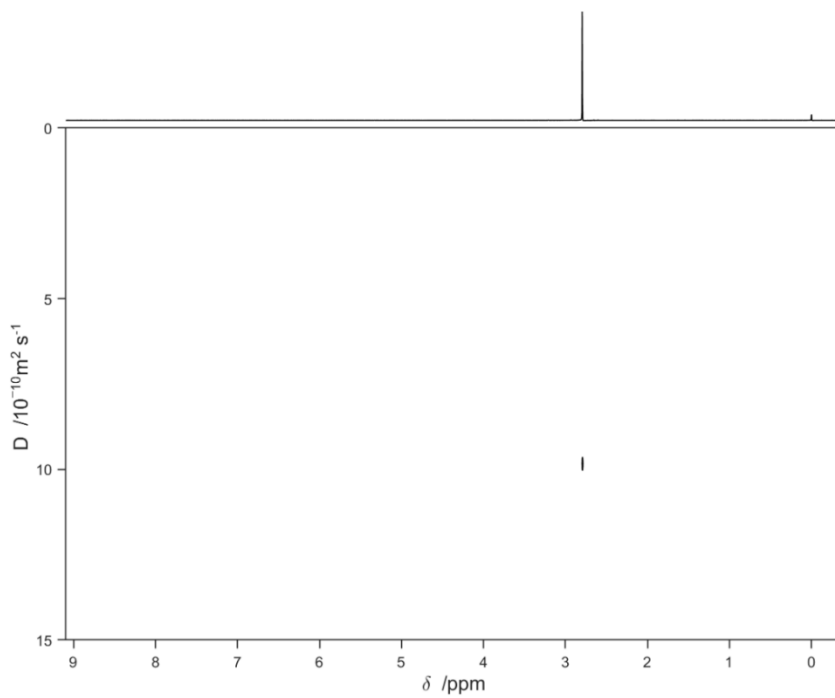

Figure 17. DOSY spectrum of **2a**.

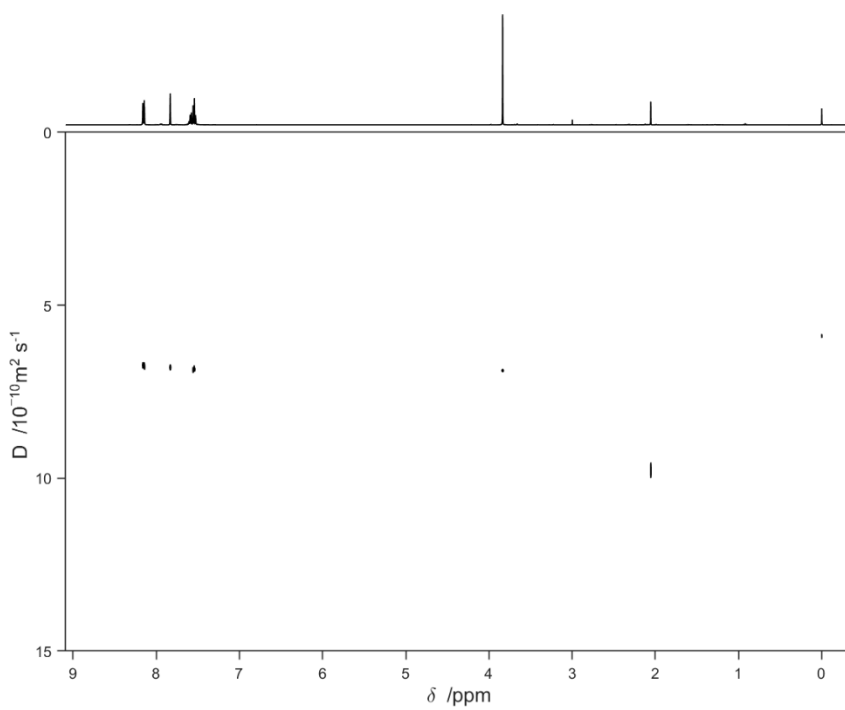**Figure 18**. DOSY spectrum of **3**.
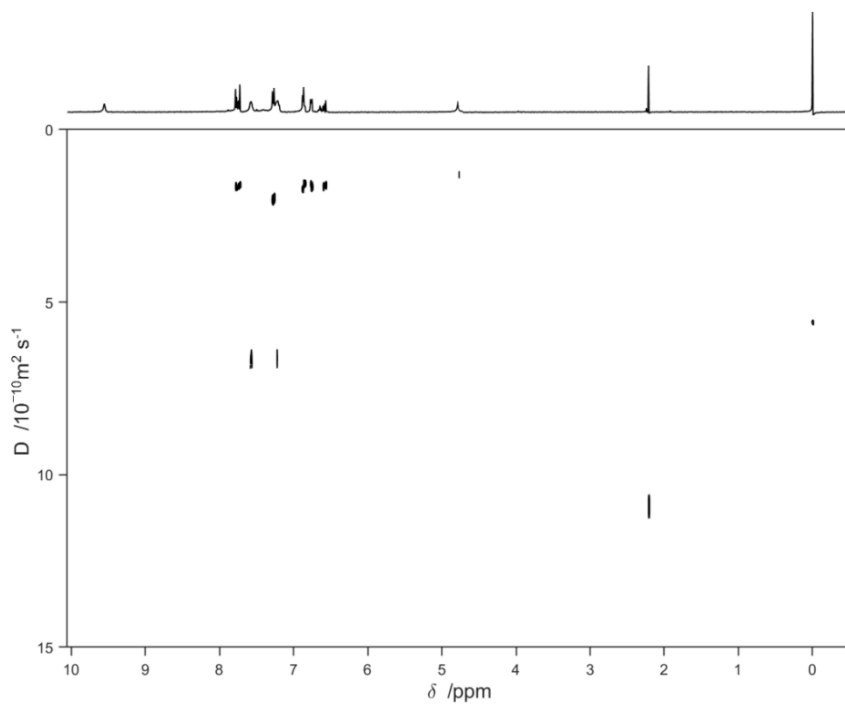

Figure 19. DOSY spectrum of **4a**.
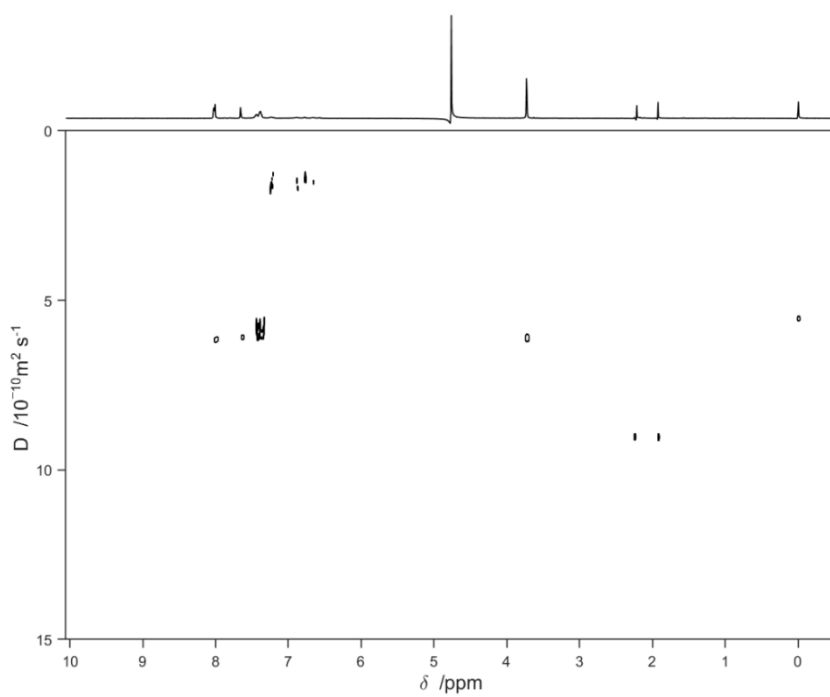
Figure 20. DOSY spectrum of **2a@1**.

Figure 21. DOSY spectrum of **4a@1**.

Chapter 3. Nanosponges based on self-assembled starfish-shaped cucurbit[6]urils functionalized with imidazolium arms

3.1 Introduction

Among the cucurbiturils, the most used is the cucurbit[6]uril (CB[6]), made up of six glycoluril units, due to the easiness in the synthesis and the functionalization procedures, compared to the other cucurbiturils.[21] Already in 1999, Kim et al. demonstrated the ability of cucurbiturils to form the one-dimensional columnar coordination polymer with potassium ions, thanks to the presence of carbonyl groups that coordinate the potassium ions.[44] Subsequently, the same group used CB[6] as a porous organic molecular material to store acetylene.[45] Recently, Xie et al. immobilized CB[6] on graphene oxide modified with Fe_3O_4 using this material to coordinate uranium(VI).[46] Furthermore, both CB[6] and CB[7] have been investigated for the application as sorbents of different gases, including CO_2, showing a good selectivity towards the latter.[47,48] Cucurbiturils have been widely used for the formation of complexes with different substrates such as ionic liquids, or nanoreactors.[49,50]

Ionic liquids have also been widely exploited to functionalize different supramolecular systems, such as self-assembling capsules,[51] or inorganic materials such as silica.[52] They have also been applied to the CO_2 capture.[53]

Before discussing the results obtained during the second year of my Ph.D. program,

I would like to introduce nanosponges briefly. Nanosponges can be either of organic or inorganic origin, natural or synthetic.[54] Nanosponges are three-dimensional networks with extensive nanometric porosity and remarkable adsorption properties. The list of materials classified in the broad family of nanosponges comprises carbon materials, zeolites, metal-organic frameworks (MOFs), and porous organic polymers (POPs). In other words, nanosponges can be counterintuitively classified as nanomaterials because of the presence of a network of nanometer-sized cavities in bulk, even though the dimensions of a given specimen, along three axes (x,y,z), can be larger than 100 nm. From this viewpoint, nanosponges are characterized by nanometric structural features, but they are generally not nanoparticles. The first example of nanosponges was based on cyclodextrins polymer (Figure 22).
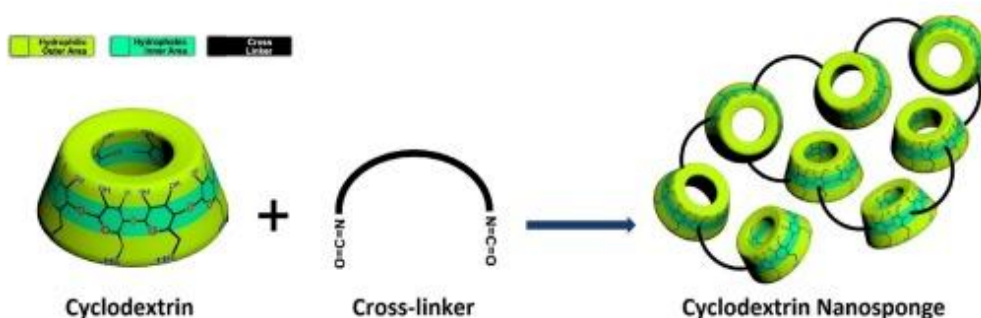

Figure 22. Nanosponges based on cyclodextrins.

In the past 20 years, nanosponges have been mainly used for pharmaceutical applications; however, there are several fields where nanosponges find wide application.

Below is a list of non-pharmaceutical applications of nanosponges:

1. Smart fabrics.

2. Agricultural applications.

3. Water purification.

4. Applications of catalysis.

5. Gas storage.

6. Industrial applications: rubber and oils.

7. Flame retardants.

The ability of nanosponges to reversibly bind compounds, even in the gas phase, through physisorption mechanisms, might lead to the development of new technology for the efficient storage of significant amounts of gas in surprisingly small volumes, without the need for high pressure and low temperatures, thus avoiding the risks and energy loss associated with the current use of compressed or liquefied gases. Inspired by these materials' remarkable capabilities, my research aims to exploit the functionalized CB[6] to form a supramolecular nanosponge to sequester CO_2.

3.2 Results and Discussion

Therefore, this work aimed to combine the ability of CB[6] to form complexes with positively charged substrates, such as ionic liquids, to create a new porous material (CB[6]-Funct$_{12}$) based on the functionalized CB[6] macrocycle. The synthesis of this

compound was accomplished by oxidizing the starting CB[6] to the dodecaoxydrilated intermediate CB[6]-(OH)$_{12}$,[55] and functionalizing this last with twelve chains of 1-(2-bromoethyl)-3-methyl-1*H*-imidazol-3-ium bromide (Imid), as reported in Scheme 3.
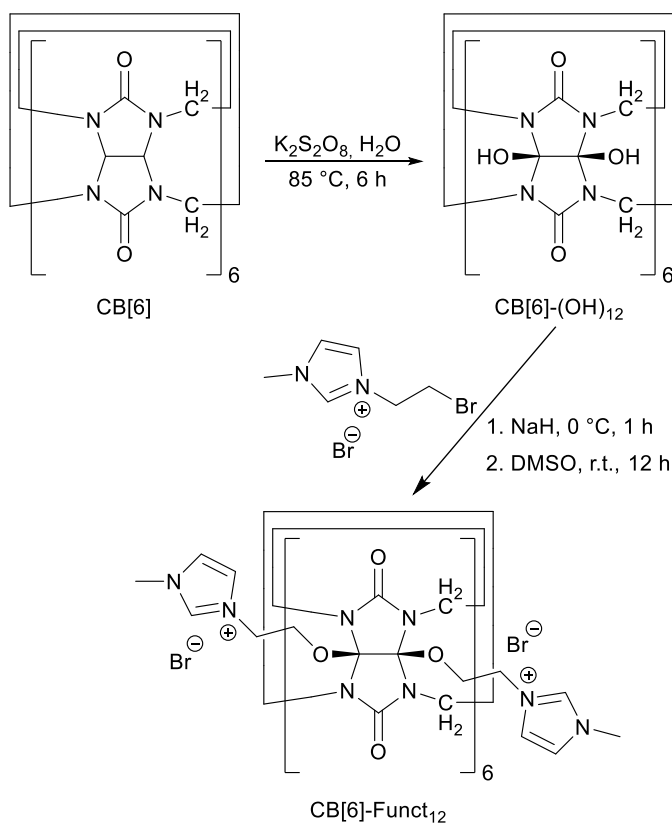
Scheme 3. Synthesis route to obtain CB[6]-Funct$_{12}$.

The CB[6]-Funct$_{12}$ was characterized by ^{1}H-, ^{13}C-NMR, FTIR, ESI-MS, and TGA analyses (see experimental section). The 3D-molecular model of CB[6]-Funct$_{12}$, minimized at PM6-D3H4 semiempirical level of theory, shows a high symmetry and resembles a 12-armed *Crossaster papposus* starfish (Figure 23). This high symmetry

is consistent with the signals observed by NMR spectroscopy, although in solution.
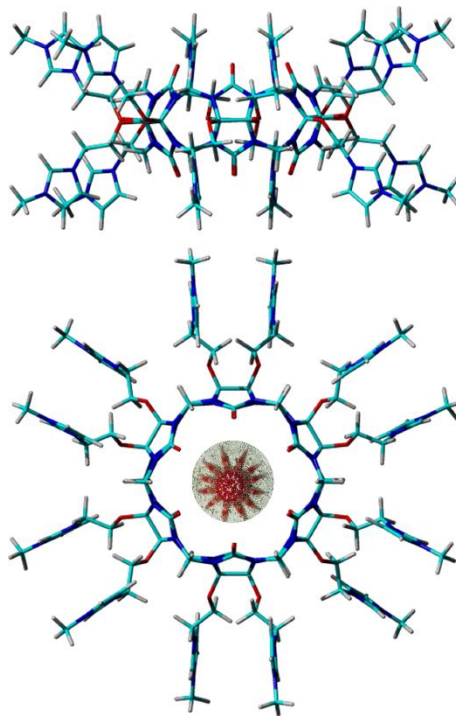
Figure 23. 3D-model of CB[6]-Funct$_{12}$; side, and top views. In the center of the top view is shown a 12-armed *Crossaster Papposus* starfish.

The presence of the positively charged imidazole groups made possible the formation of cation-dipole interactions between the cationic side chains of a CB[6]-Funct$_{12}$ and the carbonyl dipole of others CB[6]-Funct$_{12}$. This network of interactions led to the formation of further interstices, in addition to the cavities of the macrocycles, which transformed the system into a supramolecular nanosponge (Figure 24).

Figure 24. Pictographic 2D-representation of the supramolecular self-assembly of CB[6]-Funct$_{12}$.

A confirmation of these interactions is shown in Figure 25, where the carbonyl groups' vibration in CB[6]-Funct$_{12}$ are slightly shifted to 1644 cm^{-1}, compared to the 1639 cm^{-1} of CB[6].

Figure 25. Enlarged FTIR spectra of CB[6] (black line) and CB[6]-Funct$_{12}$ (red line).

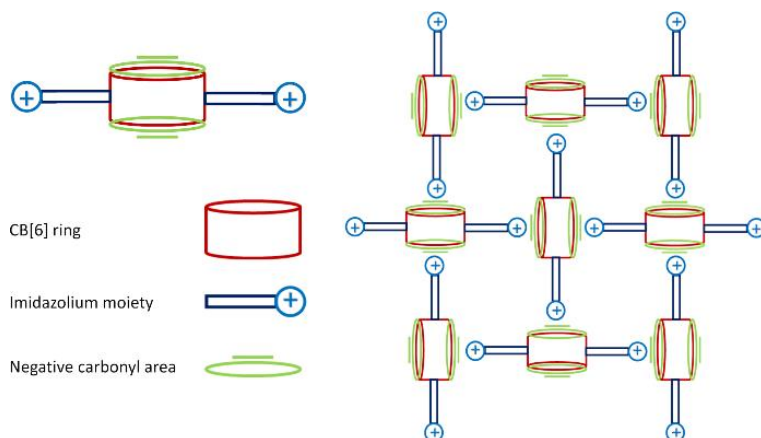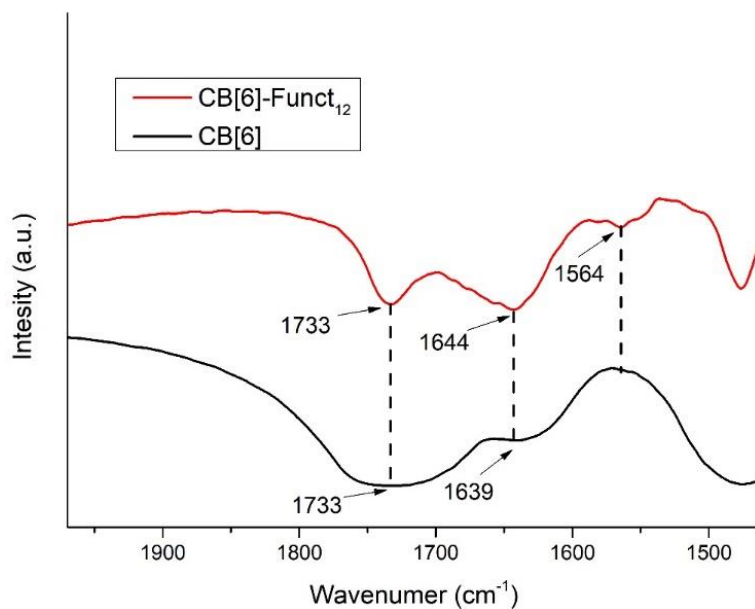Besides the vibration frequency of the C=O in CB[6]-Funct[12], there is a new peak at 1564 cm^{-1} ascribed to the splitting of the carbonyl groups of CB[6]-Funct[12]. This point to that there exist two kinds of carbonyl groups with different environments in the CB[6]-Funct[12] due to the interactions with imidazolium moiety.[56,57]

To verify the formation of this permanently porous material, we performed CO_2 adsorption studies at room temperature and atmospheric pressure on the powder sample. The breakthrough curves of CO_2 were determined by measuring the ratio between the concentration of CO_2 after the achievement of saturation in the analyzed sample and the initial carbon dioxide concentration (*i.e.*, without the sample).[58] For comparison, we used a zeolite (BEA zeolite CP 811-300 SiO_2/Al_2O_3 = 300, BET surface area 280 m^2/g), and CB[6], CB[6]-(OH)[12] and Imid. The latter constitute the building blocks of which the nanosponge is made; the BEA zeolite was chosen to compare the CO_2 adsorption performance of an inorganic and an organic sorbent, considering that this zeolite was often reported in the literature,[59-61] also for his high hydrophobicity (favored by a high SiO_2/Al_2O_3 ratio) that seems to improve its absorption properties in the presence of gaseous mixture with water.[62-64]

The CO_2 adsorption breakthrough curves show as the CB[6]-Funct[12] (black curve) exhibits superior adsorption capacities compared to both CB[6], CB[6]-(OH)[12], Imid, and BEA zeolite (Figure 26).
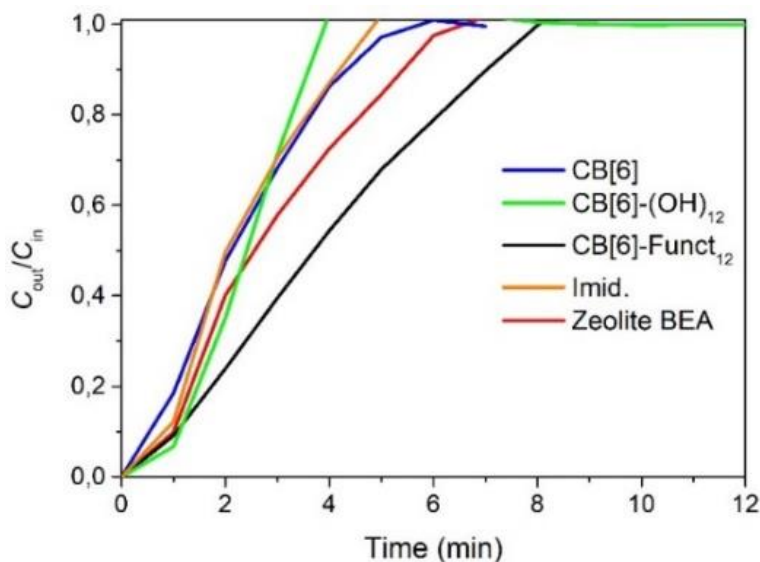
Figure 26. Breakthrough curves of CO_2 adsorbing abilities.

The amount of CO_2 adsorbed was calculated considering the formula q (mg/g) = [(C_{in} − C_f) × t × Q]/w, where w is the weight of the analyzed sample (g), Q is the CO_2 flow rate (mL/min), t is the time (min) at which the saturation was achieved, and C_{in} and C_f are the initial and final (at the saturation) CO_2 concentrations (mg/mL), respectively.[58] The graph illustrated in Figure 27 indicates the amount of CO_2 adsorbed by all the samples, in which it is possible to note as the CB[6]-Funct$_{12}$ owns an adsorption capacity eight times higher than the non-functionalized CB[6] samples. Notably, the quantity of adsorbed CO_2 by CB[6]-Funct$_{12}$ is slightly higher than that of the BEA zeolite, which is currently used in the industrial field to adsorb VOCs (volatile organic compounds) and nitrogen oxides.[65]
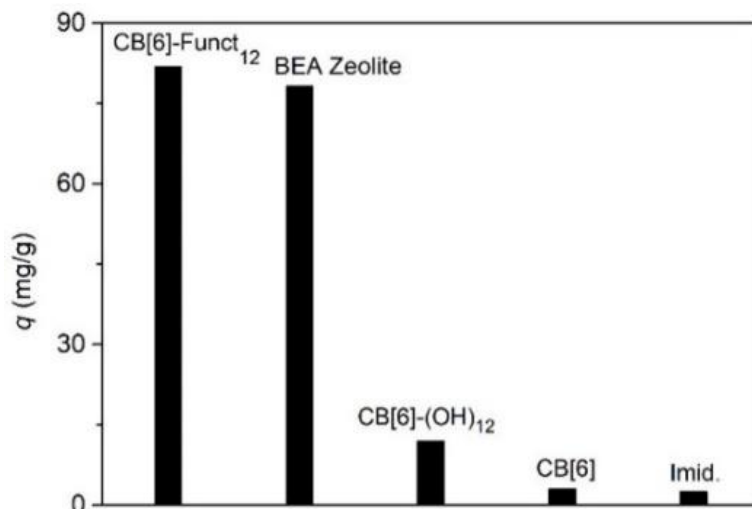
Figure 27. CO_2 adsorption capacity on 150 mg of samples.

From these data, it can be inferred that the functionalization with imidazolium moieties has allowed to significantly increased the ability of CB[6] to adsorb the carbon dioxide, leading to obtaining a nanosponge based on a supramolecular system. The good sorption capacity of the CB[6]-Funct$_{12}$ is reasonably due to the porous structure of the sample and the interaction of the adsorbed CO_2 with the negative-charged carbonyl oxygen atoms, as already reported in the literature.[47,48]

Verification of the new macrocycle's porous structure was made by the determination of the Brunauer-Emmett-Teller (BET) surface area and the Barrett-Joyner-Halenda (BJH) pore size distribution. CB[6]-Funct$_{12}$ showed a surface area value of 277 m^2/g, whereas the CB[6] had a sensibly lower surface area (144 m^2/g). From the comparison of the N$_2$ isotherms (Figure 28a), it is possible to note substantial differences between the CB[6] and the CB[6]-Funct$_{12}$ samples. This latter

compound showed a type IV curve typical of the mesoporous materials with a H2 hysteresis loop commonly observed for "ink-bottle" pores with narrow necks and wider bodies.[66,67] On the contrary, the CB[6] exhibited a type V physisorption isotherm, even associated with mesoporous structures, but with an H1 hysteresis loop typical of agglomerates in a fairly regular array, with a narrow distribution of pore size.[66,67] Indeed, the BJH curve of CB[6] (Figure 28b) was characterized by a narrow distribution centered at 11 nm (mesopores) with a mean pore volume of 0.05 cm^3/g. In contrast, the CB[6]-Funct$_{12}$ exhibited a bimodal distribution (Figure 28b) with the mean pore diameter of 3 nm (mesopores) and 65 nm (macropores) and the mean pore volume of 0.12 cm^3/g. These data point that the functionalization allowed to modify the textural properties of the CB[6], obtaining a higher pore volume and the formation of macropores. The presence of a macro-mesoporous structure in the functionalized sample favored, in accordance with the literature data,[68,69] a higher adsorption of CO_2 compared to the bare CB[6].
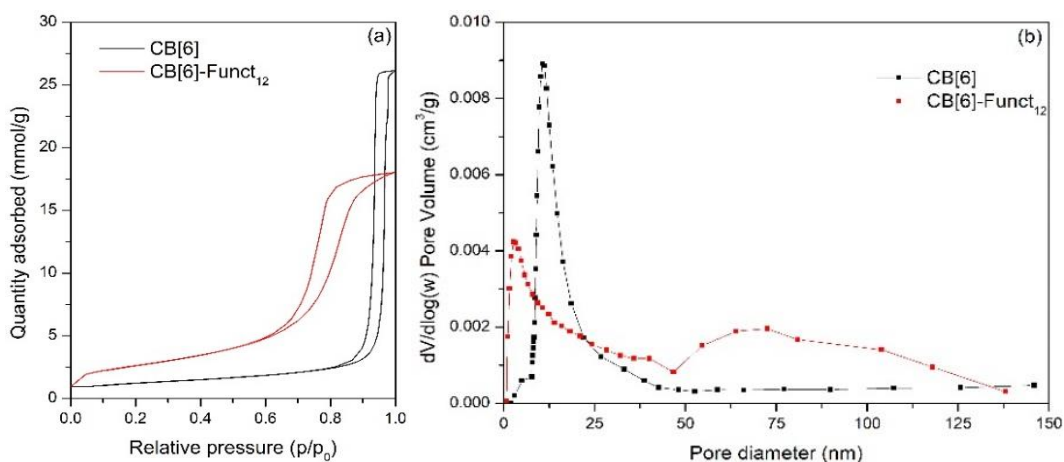
Figure 28. N_2 adsorption-desorption isotherms (a), and BJH pore size distribution curves (b) of CB[6] and CB[6]-Funct$_{12}$.

To further verify the carbon dioxide adsorption process, an infrared spectroscopy measurement was carried out to compare the $CB[6]$-$Funct_{12}$ before and after the CO_2 adsorption (Figure 29).
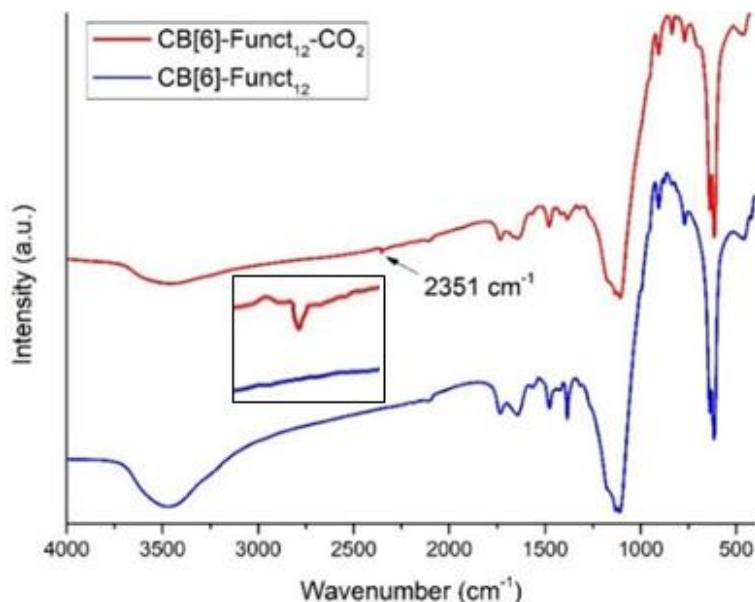
Figure 29. FTIR spectra of $CB[6]$-$Funct_{12}$ before (blue curve) and after (red curve) the CO_2 adsorption. In the box, the enlargement of the peak at $2351 \ cm^{-1}$.

The weak peak at $2351 \ cm^{-1}$ is the typical asymmetric stretching of the adsorbed CO_2 with the functionalized macrocycle.[48,70] In the box of Figure 29 is possible to note that in the FTIR spectra of the as-prepared $CB[6]$-$Funct_{12}$ (blue curve, *i.e.*, before of the CO_2 adsorption measurements), the peak related to the CO_2 is absent. Due to the low amount of CO_2 adsorbed, this signal is also not present in the FTIR spectra of the $CB[6]$ and $CB[6]$-OH_{12} samples performed after the adsorption tests (Figure 30).
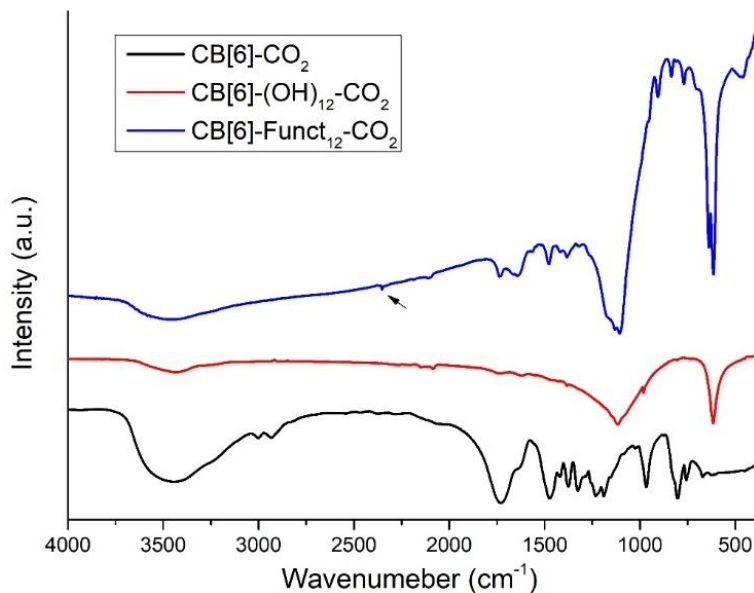
Figure 30. FTIR spectra of CB[6] (black line), CB[6]-(OH)$_{12}$ (red line) and CB[6]-Funct$_{12}$ after the CO$_2$ adsorption.

Furthermore, the synthesized supramolecular nanosponge showed improved thermal stability (see experimental section) with respect to CB[6]. Indeed, the TGA curve of CB[6]-Funct$_{12}$ shows an onset decomposition temperature at 746.2 °C and a maximum degradation rate at 815.5 °C, *i.e.*, a much higher temperature than CB[6] (T_{onset} = 350.0 °C).[45] This better thermal stability is reasonably due to the increase in the intermolecular forces established between the CB[6]-Funct$_{12}$ following the insertion of the imidazolium arms.[71-74]

Finally, to evaluate the possibility of using the CO$_2$ adsorbed by the nanosponge for organic synthesis, we investigated the possibility of performing a carboxylation reaction of acetylides. To this aim, the phenylacetylene was reacted with a saturated CO$_2$ sample of CB[6]-Funct$_{12}$ in the presence of cesium carbonate (Scheme 4).
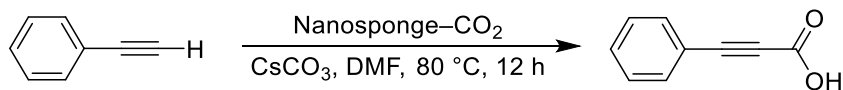
Scheme 4. Carboxylation of phenylacetylene catalyzed by CO_2 saturated CB[6]-Funct$_{12}$.

In the optimized reaction conditions (Table 9, entry 5), phenylpropiolic acid was isolated with a yield of 89%. Typically, to achieve high yields, these reactions are performed in the presence of elaborate silver or copper-based catalysts.[75,76]

The same reaction conducted in the same conditions of entry 5 of Table 6 but without the CB[6]-Funct$_{12}$ or with the BEA instead of the CB[6]-Funct$_{12}$ did not lead to the desired product (Table 6, entries 8 and 9, respectively).

Table 9. Optimization of the reaction conditions for the carboxylation of phenylacetylene[a].

Entry	Solvent	CB[6]-Funct$_{12}$ (eq.)	Adsorbed CO_2 (eq.)[b]	Temp (°C)	Isolated yield (%)
1	DMF	0.2	1.30	80	23
2	DMF	0.5	3.25	80	57
3	DMF	0.8	5.20	80	76
4	DMF	1.0	6.50	80	81
5	DMF	1.0	6.50[c]	80	89
6	DMF	1.0	6.50[c]	50	34
7	DMF	1.0	6.50[c]	100	83
8	DMF	—	6.50[c]	80	—
9	DMF	Only 1.0 of BEA	6.50[c]	80	—
10	DMSO	1.0	6.50[c]	80	81
11	ACN	1.0	6.50[c]	80	79

[a] In all the cases were used 1.0 eq. of phenylacetylene, 1.5 eq. of cesium carbonate, 2 mL of solvent,

and a reaction time of 12 h. [b] Based on the amount adsorbed by the 150 mg of CB[6]-Funct$_{12}$ sample (Figure 24, 82.5 mg/g); the excess of CO_2 was removed, except for entries 5–9. [c] Under CO_2 atmosphere.

3.3 Conclusions

In conclusion, a new supramolecular system was developed; it was capable of adsorbing a significant amount of carbon dioxide. The presence of the positively charged imidazole groups made possible the formation of intermolecular cation-dipole interactions between the cationic arms and the carbonyl dipoles of many CB[6]-Funct$_{12}$ structures. This network of interactions led to the formation of further interstices, in addition to the cavities of the macrocycles, which transformed the system into a supramolecular nanosponge, also improving the thermal stability of the compound. Finally, the adsorbed CO_2 could be used to perform several chemical organic reactions efficiently; here, the carboxylation of phenylacetylene was easily and satisfactorily accomplished.

3.4 Experimental section

General information. All the required chemicals were purchased from Merck and Aldrich Chemical Company. The synthesis of CB[6],[25] CB[6]-OH$_{12}$,[55] and 1-(2-bromoethyl)-3-methyl-1*H*-imidazol-3-ium bromide[77] were carried out as reported in the literature and subsequently characterized by NMR and IR spectroscopy.

Pre-coated aluminium sheets (silica gel 60 F254, Merck) were used for thin-layer

chromatography (TLC), and spots were visualized under UV light. Silica gel column chromatography was performed using silica gel 60–120 mesh size. ^1H and ^{13}C NMR spectra were recorded, at 300 K, on Varian UNITY Inova using CD_3OD as a solvent, at 500 MHz for ^1H NMR and 125 MHz for ^{13}C NMR. ^{13}C spectra were ^1H-decoupled, and the APT pulse sequence determined multiplicities. Chemical shift (δ) values are given in ppm.

The CO_2 adsorption experiments were carried out in a quartz U-shape reactor, utilizing 150 mg of the investigated sample and a CO_2 (99.999%) flow of 30 mL/min. The CO_2 was detected by a quadrupole mass spectrometer (Sensorlab VG Quadrupoles) following the $m/z = 44$ signal. The breakthrough curves of CO_2 were determined by measuring the ratio between the concentration of CO_2 after the achievement of saturation in the sample and the initial carbon dioxide concentration (*i.e*., without the sample). Before the measurements, the materials were pretreated in He flow (50 mL/min) at 150 °C for 2 h to remove eventual impurities from the sample's surface.

FTIR analyses in the 4000–400 cm^{-1} region were attained using FTIR System 2000 (Perkin-Elmer, Waltham, MA, USA) and KBr as media.

The mass spectrometric analysis was performed on an ion trap mass spectrometer equipped with an electrospray ion source ESI (LCQ-DECA, Thermo Fischer Scientific, San Jose, CA, USA). The sample was dissolved in a mixture of CH_3OH/H_2O (50:50 v/v) at 1×10^{-5} M and infused at 5μL/min. Full scan mass spectrum was acquired in positive ion mode in the m/z range 200–2000. ESI ion

source operated with 220 °C capillary temperature, 25 a.u. sheath gas, +5 kV source voltage, and +26 V capillary voltage. Mass calibration was achieved with a standard mixture of caffeine (Mr 194.1 Da), MRFA peptide (Mr 524.6 Da), and Ultramark (Mr 1621 Da). Data analysis was performed with the Xcalibur v. 1.3 Software.

TGA was performed employing Pyris TGA7 (Perkin Elmer, Waltham, US) in the temperature range between 50 and 950 °C, under air N_2 (60 mL/min) and heating rate of 10 °C/min.

The N_2 adsorption-desorption measurements were performed utilizing a Sorptomatic series 1990 instrument. The samples were pretreated with an outgassing step at 150 °C for 12 h. The surface area was calculated with the BET (Brunauer-Emmett-Teller) method, whereas the pore size distribution with the BJH (Barrett, Joyner, and Halenda) method.

Synthesis of CB[6]-Funct$_{12}$

To a solution of NaH (306 mg, 7.657 mmol, 13 eq, 60% dispersion in mineral oil) in anhydrous DMSO (17 mL) was added CB[6]-(OH)$_{12}$[55] (700 mg, 0.589 mmol, 1 eq) at 0 °C and stirred at r.t. for 1 h. 1-(2-bromoethyl)-3-methyl-1*H*-imidazol-3-ium bromide (2.23 g, 8.246 mmol, 14 eq.) was added to this reaction mixture and stirred for 12 h. The reaction mixture was poured into chloroform (150 mL), resulting in a pale-yellow solid precipitate that was collected by filtration, washed with chloroform, and finally dried in the oven at 60 °C to give the CB[6]-Funct$_{12}$ (770 mg, 38%). ^{1}H NMR (500 MHz, Methanol-*d*): δ = 3.88 (24 H, t, *J* = 5.9 Hz), 3.98 (36 H,

s, *N*-Me), 4.68 (24 H, t, J = 5.9 Hz), 4.73 (12 H, d, J = 15.3), 5.52 (12 H, d, J = 15.3), 7.62 (12 H, d, J = 2.0 Hz), 7.67 (12 H, d, J = 2.0 Hz), 9.10 (12 H, s); ^{13}C NMR (125 MHz, Methanol-*d*): δ = 36.95, 49.99, 52.08, 66.57, 109.90, 123.76, 125.59, 137.51, 154.80.

Synthesis of phenylpropiolic acid

Into a pressure tube containing CB[6]-Funct$_{12}$ (715 mg, 0.206 mmol, 1.0 eq), phenylacetylene (21.0 mg, 0.206 mmol, 1.0 eq), Cs_2CO_3 (100.7 mg, 0.309 mmol, 1.5 eq), and DMF (2 mL), under CO_2 atmosphere and the mixture was heated at 80 °C for 12 h. After this time, the mixture was processed as reported in the literature,[75] obtaining the phenylpropiolic acid in 89% yield, based on phenylacetylene.

Characterizations: NMR, FTIR, ESI, and TGA
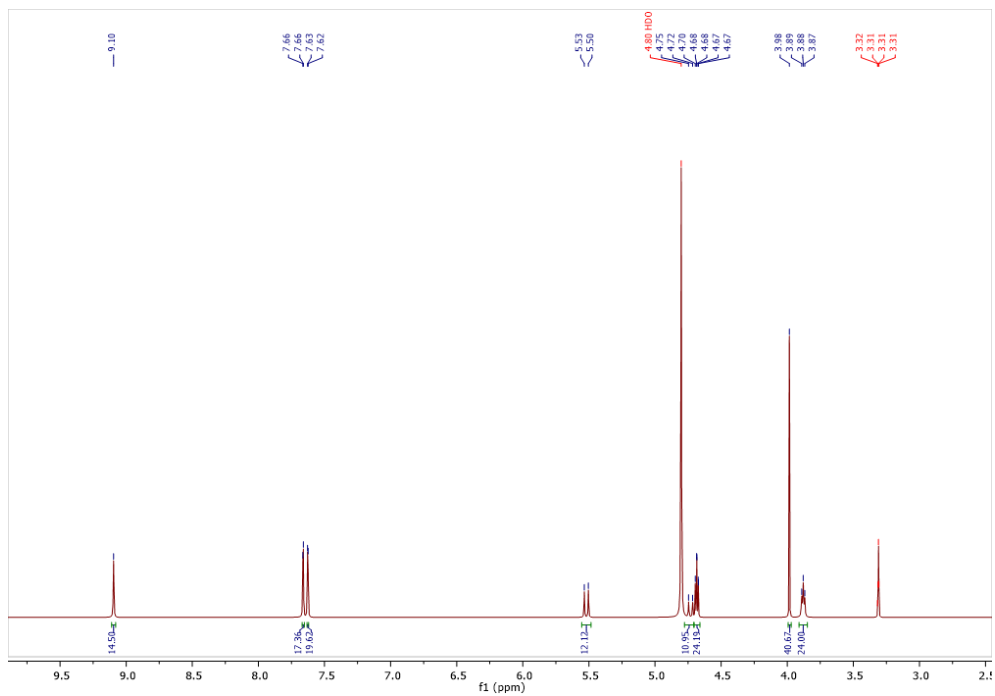
Figure 31. ^{1}H NMR spectrum of CB[6]-Funct$_{12}$.
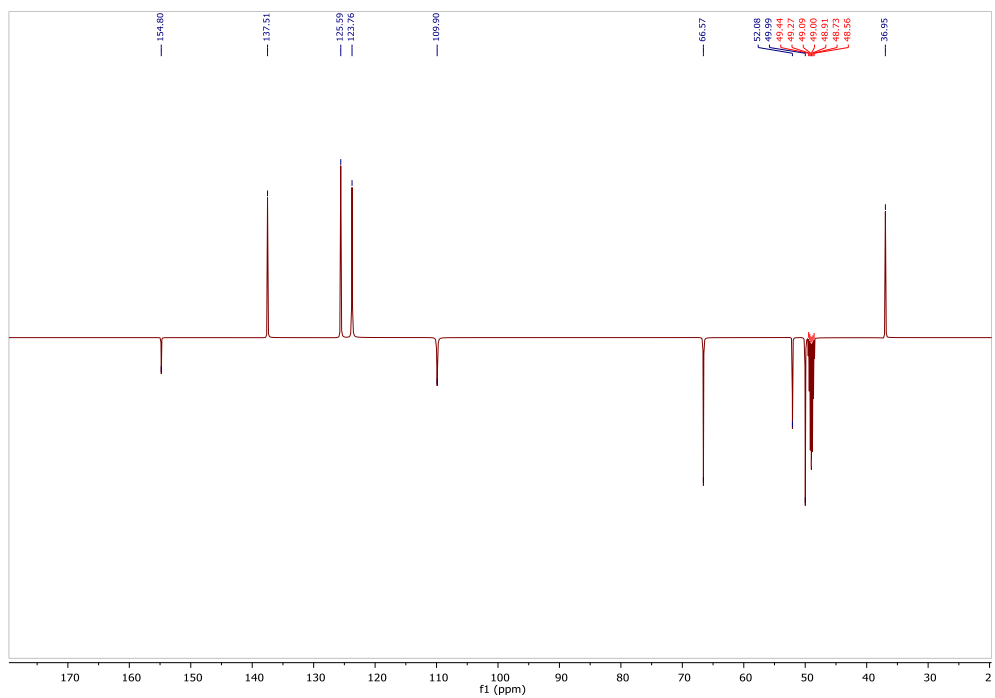
Figure 32. ^{13}C NMR spectrum of CB[6]-Funct$_{12}$.
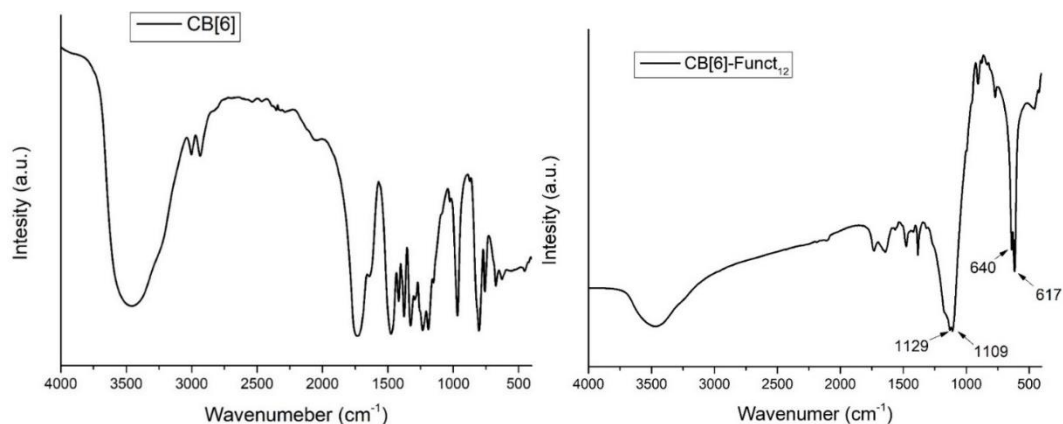
Figure 33. FTIR spectra of CB[6] (left) and CB[6]-Funct$_{12}$ (right). On the left, it is possible to see the typical vibrations of the carbonyl groups at 1733 cm^{-1}, as previously reported in the literature.[56] On the right, it is possible to see the presence of the characteristics C–O–C strecthing[78] at 1109 cm^{-1} and 1129 cm^{-1}, Me–N bending at 617 cm^{-1}, and H–C=C bending at 640 cm^{-1}.[79]
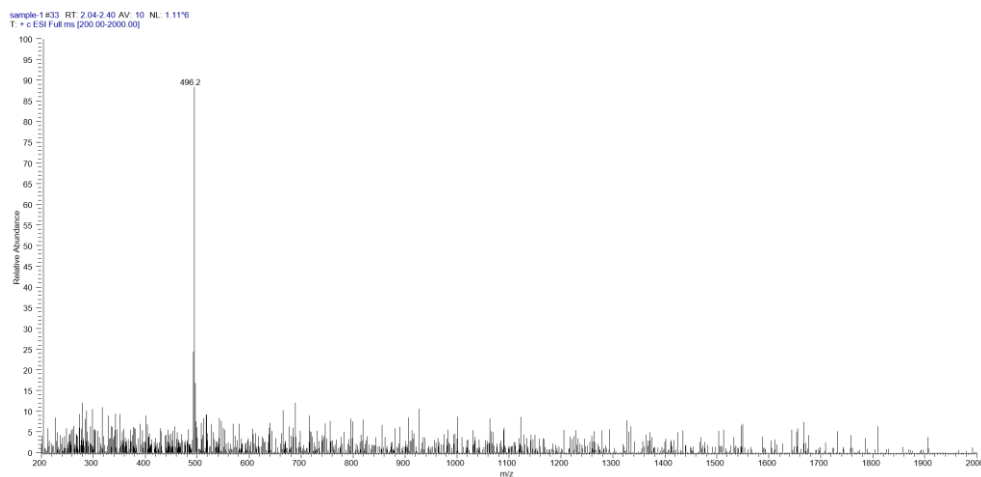
Figure 34. Full scan ESI mass spectrum of a CB[6]-Funct$_{12}$ solution. The spectrum shows a signal at m/z 496.2, with $z = 6$. This m/z value corresponds to the average molecular mass of the multi charged ion of CB[6]-Funct$_{12}$ minus six bromides as originated during ESI ionization (calcd for $[C_{108}H_{144}N_{48}O_{24}Br_6]^{6+}$, 496.3).

Figure 35. TGA thermogram (red line, left axis) and DTG (blue line, right axis) of CB[6]-Funct$_{12}$.

Chapter 4. Porous bio-hybrid material based on Loofah-Halloysite for gas adsorption and drug delivery

4.1 Introduction

Currently, the environmental awareness of the global community boosted the interest of both academy and industry researchers in developing new advanced materials which are both eco-friend and able to exhibit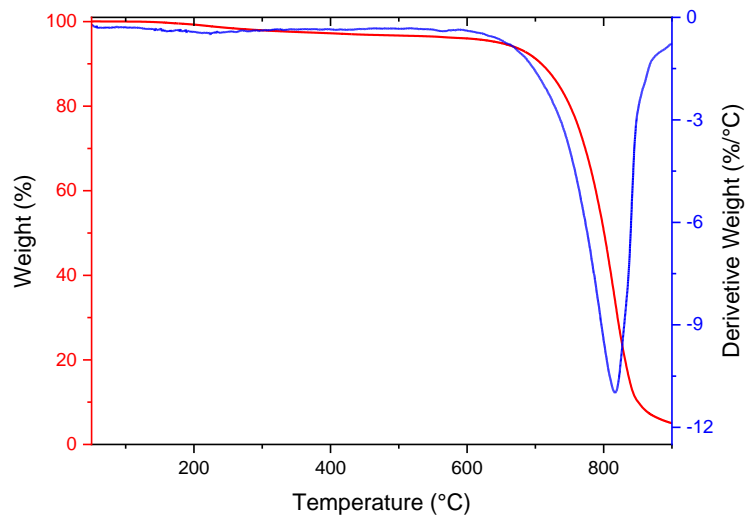 the targeted properties for the required application. For this purpose, scientists often looked at nature, trying to mimic it to find eco-materials with high performance and low cost. Among these, the loofah sponge (L), a natural porous and light 3D structure material, obtained from the matured dried fruit of *loofah cylindrica*,[80] has been used in many applications, such as cleaning products and insole materials,[80,81] pharmaceuticals,[82,83] environmental engineering,[84,85] biotechnology.[86] The highly porous structure provides excellent gas exchange and facilitates effective light transmission,[87] allowing its use for gas adsorption and promising photocatalytic applications.[88] Due to its high degree of lignification, loofah also has great potential for use in composite materials and fibers.[89-93] However, L must be coupled with inorganic materials to provide better physical, chemical, and mechanical properties to expand its applicability.[88]

In this work, we functionalized the L fibers with halloysite (H), a natural clay mineral of the kaolin group,[94] to improve the loofah's adsorption performance and mechanical resistance. This is the first attempt to prepare and apply this hybrid loofah-halloysite organic-inorganic bio-composite to the best of our knowledge.

H has a 1D tubular structure in the range of mesopores (2–50 nm) and macropores (>50 nm).[95] This more significant porosity with respect to other known synthetic porous materials, such as carbon nanotubes (CNT), qualifies H for loading large molecules such as drugs and enzymes.[96] Moreover, its peculiar tubular aluminosilicate structure enables H to be variously functionalized (external, internal, and interlayer surface), thus making it highly versatile.[94] Finally, H has been proved to be highly biocompatible and low toxic.[97]

Specifically, in this work, we used different crosslinkers for the loofah functionalization with halloysite. The new organic-inorganic composites were characterized by several techniques (Fourier-transform infrared spectroscopy, Thermogravimetric analysis, High-Resolution Transmission Electron Microscopy, and Tensile test). These composites were applied for the carbon dioxide capture, showing superior adsorption capacities than the single components, L and H, and to zeolites currently used in industry. Furthermore, they also proved to be candidates for the adsorption/delivery of resveratrol, a natural phenolic compound found in grape skin and other plants, with many beneficial effects on human health, as an antioxidant, antitumor, neuroprotective, and antiviral activities.[98-100]

This study's results underline that the L functionalization with H gives rise to a synergistic effect enhancing the adsorption properties compared to the starting materials, thus pointing to the possibility of using this new low-cost, eco-friend, and biocompatible composite in various fields such as gas adsorption and drug delivery.

4.2 Results and Discussion

4.2.1 Materials preparation

The polypores material was synthesized using loofah (L) and halloysite (H) by exploiting the surface hydroxyl groups to bind them via a crosslinker. The crosslinkers used were: 1,1'-carbonyldiimidazole (C) and 1,4,5,8-naphthalenetetracarboxylic dianhydride (N), both of which have often been used for the synthesis of different materials such as cyclodextrin nanosponges[101,102] (Figure 36).
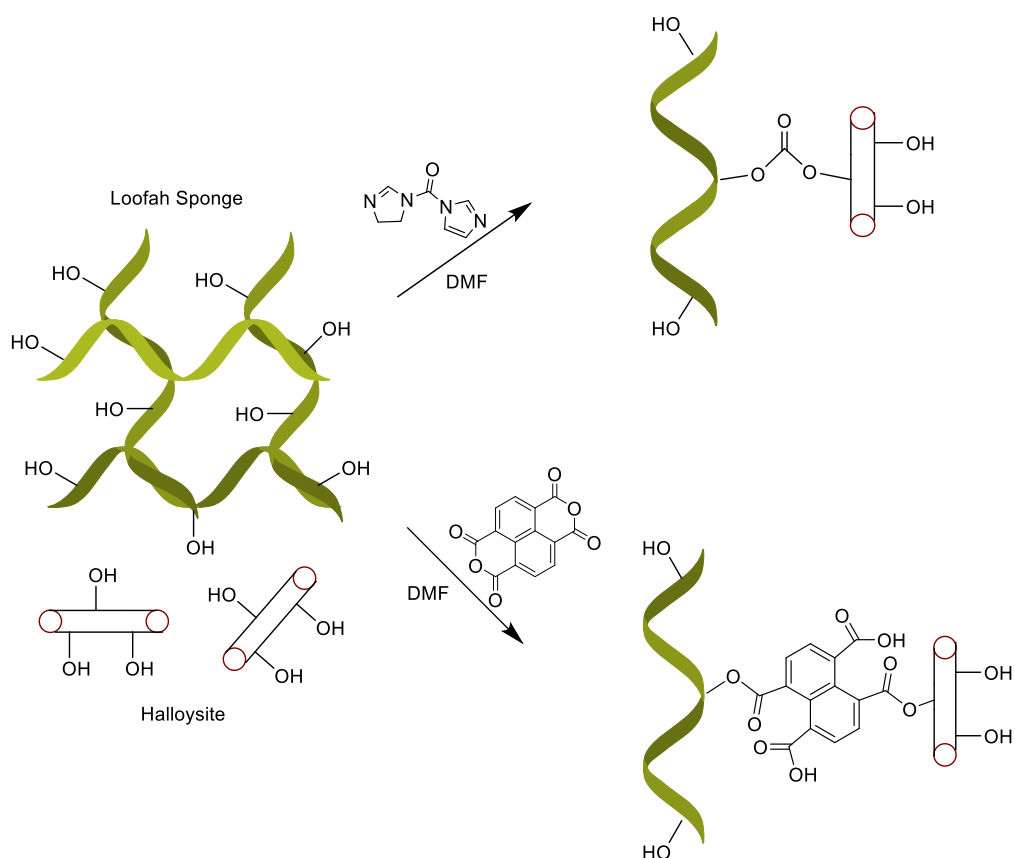

Figure 36. Synthesis of the loofah-halloysite composite.

An L:H ratio of 1:5 w/w was used, and the molar ratios of the crosslinkers were varied with respect to H. In particular, ratios of 2, 10, and 20 equivalents were used for each crosslinker. Composites prepared with 1,1'-carbonyldiimidazole will be named with the acronym LHCx and composites prepared with 1,4,5,8-Naphthalenetetracarboxylic dianhydride will be named with the acronym LHNx, where x indicates the crosslinker equivalents with respect to H (Table 10).

Table 10. Reaction conditions for the synthesis of LHCx and LHNx composites.[a]

L:H ratio 1:5 w/w				
Time h	H:C ratio (eq.)	Composite name	H:N ratio (eq.)	Composite name
3	1:2	LHC2	1:2	LHN2
12	1:10	LHC10	1:10	LHN10
24	1:20	LHC20	1:20	LHN20

[a]All reactions were conducted in DMF at 80 °C.

4.2.2 Pristine materials and composites characterization

Pristine loofah (L), halloysite (H), and LH composites were characterized employing thermogravimetric analysis (TGA), Fourier-transform infrared spectroscopy (FT-IR), Scanning Electron Microscopy (SEM), transmission electron microscopy (TEM), and high-resolution transmission electron microscopy (HR TEM). The amount of H in both LHCx and LHNx composites was checked through TGA. The thermographs of all samples are reported in the experimental section (Figures 48a,b). Mass losses (mass %) of composites and pristine materials are reported in Table 11.

Table 11. Mass losses (mass %) for pristine L, H, LHCx, and LHNx composites, from TGA analysis.[a]

Sample	Mass loss (%)			Residue (%)
	T < 150 °C	150 °C < T < 380 °C	380 °C < T < 700 °C	T > 700 °C
Halloysite	1.2	1.8	11.2	85.8
Loofah	3.0	67.0	29.0	1.0
LHC2	5.5	64.5	26.5	3.5
LHC10	4.0	66.0	26.0	4.0
LHC20	4.0	66.5	24.5	5.0
LNH2	3.0	66.5	26.0	4.5
LNH10	3.0	66.0	24.0	7.0
LNH20	3.0	67.0	20.0	10.0

[a]Tests were conducted with a temperature ramp of 10 °C/min from 25 °C to 900 °C in an inert nitrogen atmosphere, followed by 15 min isotherm at 900 °C in air flux.

The decomposition profile of L shows three main steps, at the following temperatures: below 150 °C, between 150 °C and 380 °C, and above 380 °C. The mass loss at T < 150 °C could be reasonably attributed to the release of water molecules on the surface. The mass loss from 150 °C to 380 °C is attributed to the polysaccharide component (hemicellulose and cellulose). The mass loss at T > 380 °C is due to the decomposition of the lignin component.[103]

The thermal profile of H is characterized by two main steps: below 540 °C and above 540 °C. The mass loss at T < 540 °C is attributed to the release of water molecules

on the surface. The mass loss at T > 540 °C is due to the so-called bound water (structural water) loss and the dihydroxylation process.[104]

Appreciable mass losses were found for the LHCx and LHNx composites in temperatures ranging from 150 °C to 700 °C. For all LH samples, the residual amount was also reported and used to indicate the actual amount of H, which was incorporated in the composites.

Based on these residue values, the theoretical and experimental loading of H (%) were compared.[105] The experimental H loading % of LHCx and LHNx composites are reported in Table 12.

Table 12. Loading of H (%) in LHCx and LHNx composites calculated from TGA data.

Sample	H loading (%)	Sample	H loading (%)
LHC2	2.5	LHN2	3.5
LHC10	3.0	LHN10	6.0
LHC20	4.0	LHN20	9.0

Infrared spectroscopy was used to study the nature of functional chemicals groups. Pristine materials and LH composites were characterized employing attenuated total reflectance Fourier transform infrared spectroscopy (FT-ATR). Functional groups were detected by analyzing the samples on a zinc selenide crystal (ZnSe) (Figure 37a,b).
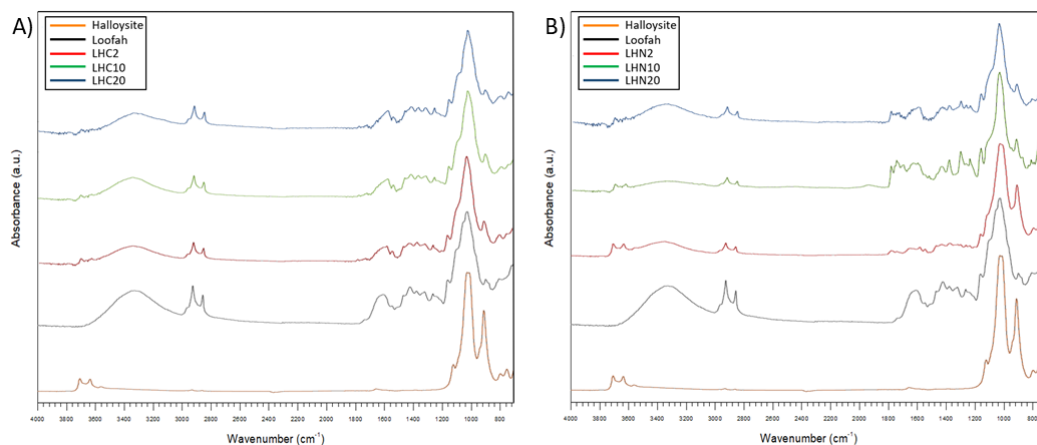
Figure 37. FT-ATR spectra of H (orange line), L (black line) and LH composites: a) LHC2 (red line), LHC10 (green line) and LHC20 (blue line); b) LHN2 (red line), LHN10 (green line) and LHN20 (blue line).

In the spectrum of L, the C–O–C symmetric stretching and the C–OH stretching vibrations were at 1100 cm^{-1} and around 1055–1060 cm^{-1}, respectively. These two bands arise from its polysaccharide component. The band at 1430 cm^{-1} is attributed to the CH$_2$ bending of cellulose. The two bands at 1370 cm^{-1} and 1320 cm^{-1} are due to the alcohol groups of the cellulose chains.[106]

In the spectrum of H, bands related to water molecules are evident: the one at 3520 cm^{-1} is related to the O–H stretching typical of coordination water. The peak at 910 cm^{-1} can be assigned to the Al–O–OH vibration, while the bands at 3710 and 3630 cm^{-1} are attributed to the stretching vibration of the inner-surface Al–OH groups. A strong O–Si–O peak is observed at around 1150 cm^{-1}, and the peaks at 770 and 745 cm^{-1} are assigned to the stretching mode of apical Si–O.[107]

In the spectra of all LH composites (Figures 37a,b), bands related to the starting

materials are observed along with other features due to the chemicals used to generate the bond between H and L. In LHCx samples, a new weak signal appears at 1747 cm^{-1}, related to the C=O stretching of the carbonate bridge group. This new band, along with other new features, demonstrates that the functionalization procedure with 1,1'-carbonyldiimidazole was successful. These new features, related to the chemical alteration of the lignin component, suggest that the chemical bond has been formed with this part: the band at 1695 cm^{-1} appears asymmetrical and usually originates from unconjugated carbonyl groups on the lignin structure.

In LHNx samples, a new series of signals appear in the range between 1800–1598 cm^{-1}: the band at 1610 cm^{-1} is related to C=O stretching vibration of CO$_2$H, whereas the band at 1790 cm^{-1} is related to the C=O stretching vibration of hydrogen-bonded esters.

Morphological investigation of L, H, and LH composites was performed through transmission electron (TEM) and high-resolution transition electron microscopies (HR-TEM). In order to check if the morphology has been maintained after the functionalization procedure, the LHC10 sample was selected and analyzed. Acetone suspensions of L, H, and LH composites, with 1 mg/mL as the concentration, were sonicated for 5 minutes using an ultrasonic bath. The unstable suspensions had been then analyzed, and micrographs were taken at lower and higher magnification (Figure 38).
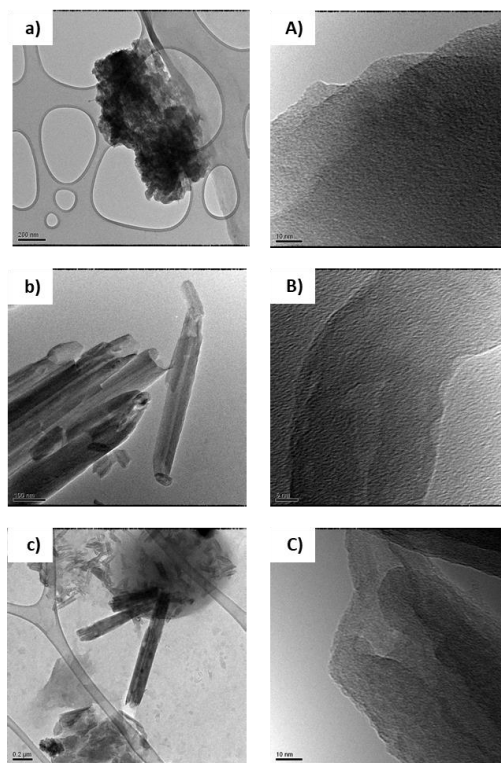
Figure 38. Micrographs of L (a, A), H (b, B), and LHC10 (c, C), after mild sonication for 5 min. Bright-field TEM micrographs at low magnification (a–c). HR-TEM micrographs (A–C).

The micrograph at lower magnification in Figure 38a reveals that the morphology of loofah seems to be characterized by a highly disordered texture. The statistical analysis performed on many micrographs underlines the high purity of this lignocellulosic material. HR-TEM image (Figure 38A) suggests that the pristine loofah could have a light graphitized layer on the surface.

Morphologies of halloysite nanotubes and LHC10 had been checked, and micrographs are in Figure 38. The micrographs at high magnification in Figures 38B,C show a regular nanotube skeleton in both samples. The inspection of such

images allowed us to detect the lengths of halloysite tubules (0.5 to > 10 µm) and a diameter in the range of 50 to 110 nm. The micrographs at low magnification reveal a different degree of aggregation for the pristine (Figure 38b) and functionalized (Figure 38c) halloysite nanotubes: bundles of oriented and aligned nanotubes are clearly visible in the former figure, whereas the more disordered distribution and the presence of loofah on the nanotubes is appreciable in the latter one. It appears that the functionalization procedure can lead to an appreciable nanotubes-loofah interaction. Another important information that brings back from HR-TEM investigation is that the sonication and functionalization processes did not modify the nanotubes dimensions.

Tensile tests were performed on starting material and LH composites. The samples have been pulled with the method reported in Table 13 (see experimental section).
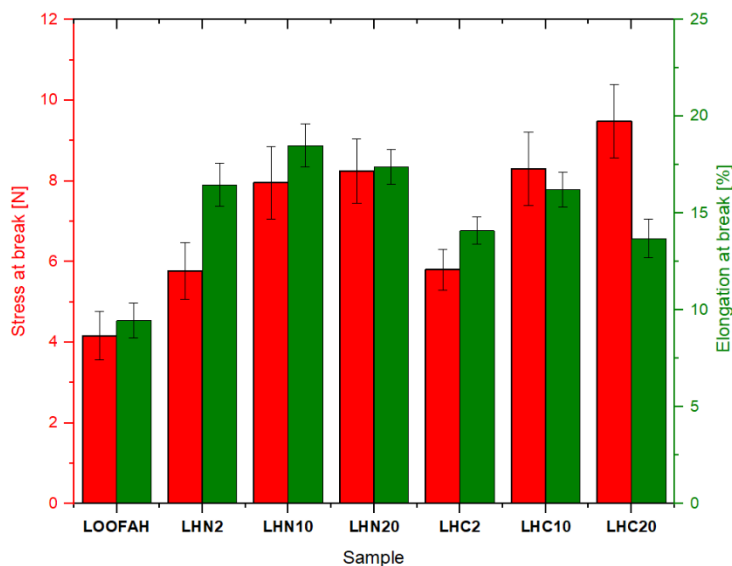

Figure 39. Effect of H content on tensile properties of HL composites.

As reported in Figure 39, the enhanced interfacial interaction, together with the covalent interaction between L and H, seem to significantly influence the mechanical properties of HL composites compared with the starting loofah. In fact, the presence of H in the composite material makes the loofah fibers stronger than the untreated ones. The large surface area of H leads to significant intermolecular interactions with the L fibers. An increase in stress and elongation at break with increasing H content in composites indicates that this interaction is stable. In fact, the intercalation of the nanotubes between the L fibers allows them to slip, making it possible to elongate the material before fracture.

SEM images of L and LHNx composites are shown in Figure 40. From Figure 40a, it was observed that the surface of the fibers is tightly banded; the interior of the loofah fiber had a porous structure with the diameter of the macropores of 12–20 microns.

Figures 40b,c represent the SEM images of loofah/halloysite composites treated with dianhydride. A better distribution of the nanotubes on the loofah surface (red arrows) demonstrates an increase in the amount of halloysite. This behavior was visible when LHN2 and LHN20 composites were compared.

The dimensions of the nanotubes are consistent with those detected by analyzing micrographs obtained from transition electron microscopy (0.5–2.0 µm). The increased distribution of the nanotubes appears to agree with the results of the tensile tests. The LHC series show similar morphology.
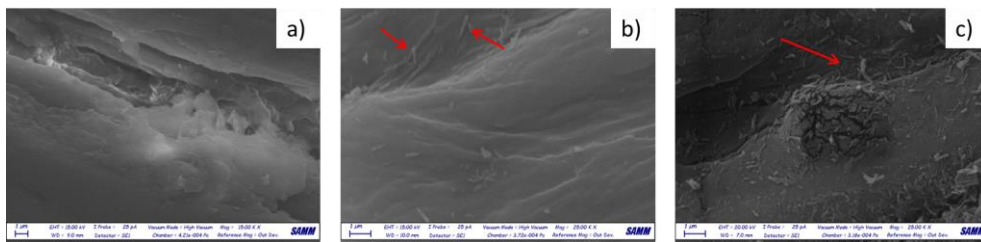
Figure 40. SEM micrographs of Loofah (a), LHN2 (b), and LHN20 (c) composites. Red arrows indicate halloysite nanotubes on the loofah surface.

4.2.3 CO_2 adsorption and CO_2-TPD measurements

The CO_2 adsorption capacity of the investigated materials is illustrated in Figure 41 (the corresponding breakthrough curves are reported in the experimental section Figure 49). For comparison we used two zeolites a BEA zeolite (CP 811-300, $SiO_2/Al_2O_3 = 300$, BET surface area 280 m^2/g) and a MOR zeolite (CBV 21 Ammonium form, $SiO_2/Al_2O_3 = 20$, BET surface area 500 m^2/g). These zeolites are widely used as CO_2 and gases sorbents.[59,61,108,109] Furthermore, in Figure 41 is displayed the amount of CO_2 adsorbed on the grounded mixed sample of loofah and halloysite coded as LHM (*i.e*., without the addition of crosslinkers). The bare L showed the lowest CO_2 adsorption capacity ($q = 8.9$), whereas the pure H ($q = 143$) performance is similar to the MOR zeolite. The addition of the crosslinkers to the halloysite and loofah allowed increasing the amount of adsorbed CO_2 with the sample LHC10 that exhibited the highest value ($q = 162.8$). A lower amount of crosslinker C (LHC2) did not alter the sorption capacity of the composites, whereas a slight decrease was verified with the crosslinker N (LHN2, $q = 157.9$ and LHN10,

$q = 161.8$). A further increase of both C and N crosslinkers led to an additional decrease in CO_2 adsorption, more relevant for the LHN20 ($q = 131.5$) than the LHC20 sample ($q = 155.2$). The increase in the number of naphthalene groups probably led to steric hindrance effects that did not favor the adsorption of CO_2. The CO_2 adsorption trend can be rationalized considering the loading of H reported in Table 12. Indeed, it seems that after a definite H loading, the synergistic effect between the H and L was progressively lower, following a "volcano" trend. In particular, for the crosslinker C the best loading is 2.5–3.0% of H, whereas, for the N crosslinker, the maximum is between 3.5 and 6.0% of H.
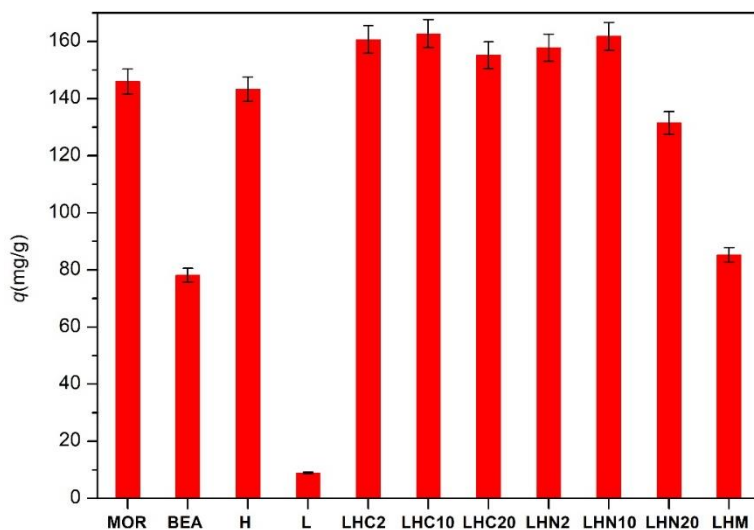

Figure 41. The CO_2 adsorption capacity of the investigated samples.

The increase in the number of naphthalene groups probably led to steric hindrance effects that did not favor the adsorption of CO_2. Interestingly, the combination of loofah and halloysite especially promoted by the crosslinker C with a definite

amount, allowed to exploit a holistic effect. Indeed, the bare L and H performance sum gave a q value of 151.9, lower than the best composite LHC10 (162.8), where the amount of halloysite loaded on loofah is only the 3.0% (Table 12), significantly lower than the pure H. This pointed to as only the strong interaction between the two components of the hybrid composite mediated by the crosslinker led to a synergistic effect that favored the CO_2 adsorption.

Five consecutive runs of CO_2 adsorption-desorption measurements were carried out to determine the reusability properties of LHC2. Based on the CO_2-TPD profile of LHC2 (Figure 50 experimental section), after the adsorption of CO_2 and the surface saturation, the CO_2 flow was stopped, and the sample was heated from room temperature to 180 °C (the CO_2 desorption peak was at 171 °C). The composite was cooled under He flow, and the CO_2 flow was turned on to favor its adsorption to perform the subsequent run.

From Figure 42, it is possible to note that the adsorption capacity of the LHC2 composite started to become lower from the third run, reaching in the fifth run a q value of 132.8. This behavior can be reasonably ascribed to the folding of the loofah favored to the consecutive run of heating and cooling.[110] Although the degradation of composite started at 230 °C as stated by the TGA measurements (Figure 48a,b see experimental section), the heating at a temperature (180 °C, necessary for the desorption of CO_2) near to the initial decomposition temperature of the composite can create loofah aggregates in the structure of the hybrid material that harmed the adsorption properties. However, comparing Figures 41 and 42, it is essential to

highlight that after the fifth run, the performance of the LHC2 material was better than BEA zeolite and LHM samples.
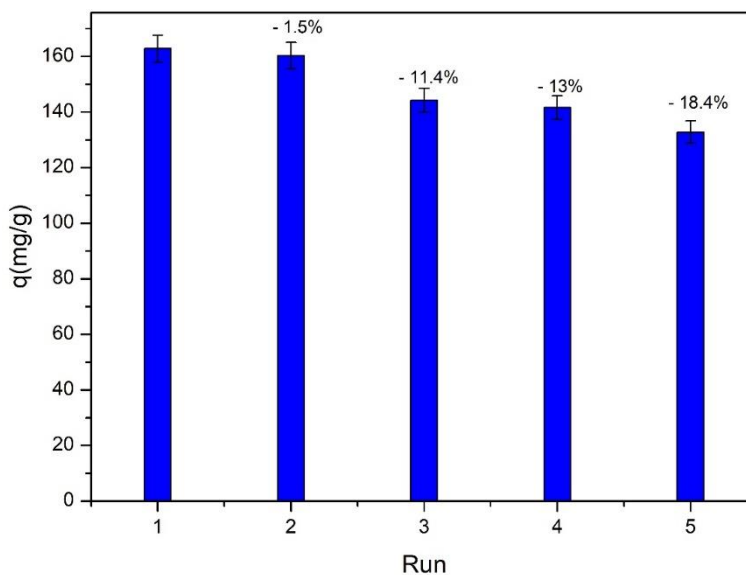
Figure 42. The adsorption capacity of LHC2 composite after five consecutive runs of CO_2 adsorption-desorption.

Further confirmation of the strong interaction between the new hybrid material and carbon dioxide was verified by FTIR investigation. In particular, it is possible to deduce from Figure 43 that after 24 hours from the adsorption of CO_2, the samples LHC2 and LHN2 show the typical stretching of carbon dioxide at 2352 cm^{-1}.[48,111] Interestingly, even after 48 hours, both samples show the same band (Figure 44).

Figure 43. FTIR spectra of LHN2 and LHC2 after 24 h of CO_2 adsorption.

Figure 44. FTIR spectra of LHN2 and LHC2 after 48 h of CO_2 adsorption.

4.2.4 Drug loading

Resveratrol charge on LHC2 composite was carried on at different weight ratio: 1:10, 1:50, 1:100 and 1:1000 (drug: LHC2 w/w). Briefly, 30 mg/L resveratrol solution was prepared, and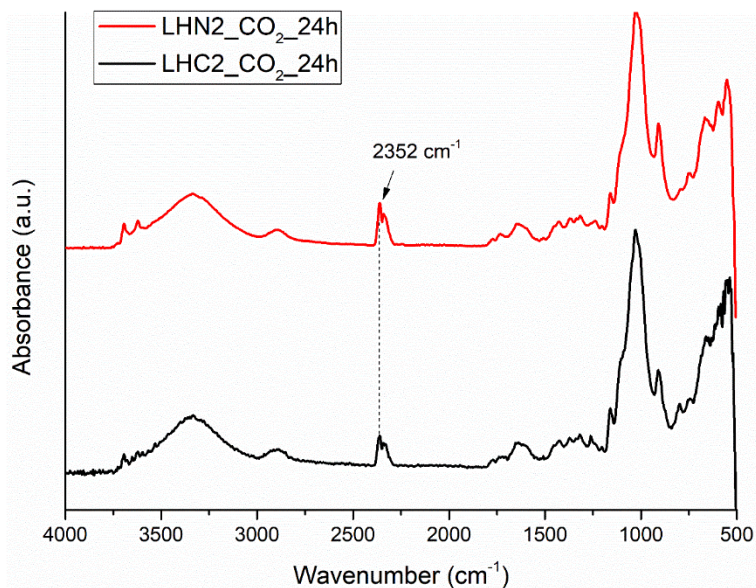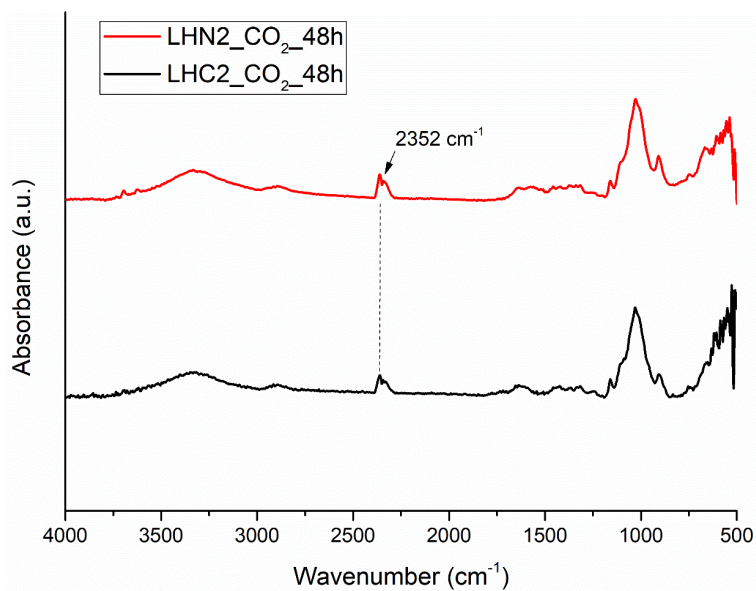 the correct amount of LHC2 was suspended and kept under stirring for 1 h in the dark. Then, the suspension was centrifuged in order to separate the loofah materials from the uncharged drug. The Drug Loading Capacity (DLC) and Encapsulation Efficiency (EE) were evaluated using the spectrophotometric method at 303 nm, fitting with a previously obtained calibration curve.[112,113] Every solution was diluted to 5.4 mg/L before each analysis to remain in the Lambert-Beer law regime. The DLC and the EE were evaluated following respectively these Equation 3 and 4:

$$DLC = \frac{\text{loaded drug amount}}{\text{total loofah amount}} \tag{3}$$

$$EE = \frac{\text{loaded drug amount}}{\text{total drug amount}} \tag{4}$$

From Figure 45, it is possible to note that the highest EE was obtained with the highest quantity of adsorbent, as expected. However, for our purpose, it is more suitable to evaluate the DLC that is optimized with a 1:10 drug-adsorbent ratio. The results obtained are in line with the data reported in the literature for the delivery of resveratrol.[114] The resveratrol loading capacity measurements were also performed on the individual starting materials (Figure 51 see experimental section). The latter showed no-significant load capacity (around 2%), which underlines, as in the case

of CO_2 adsorption, the synergistic effect of the functionalization of the loofah with the halloysite.
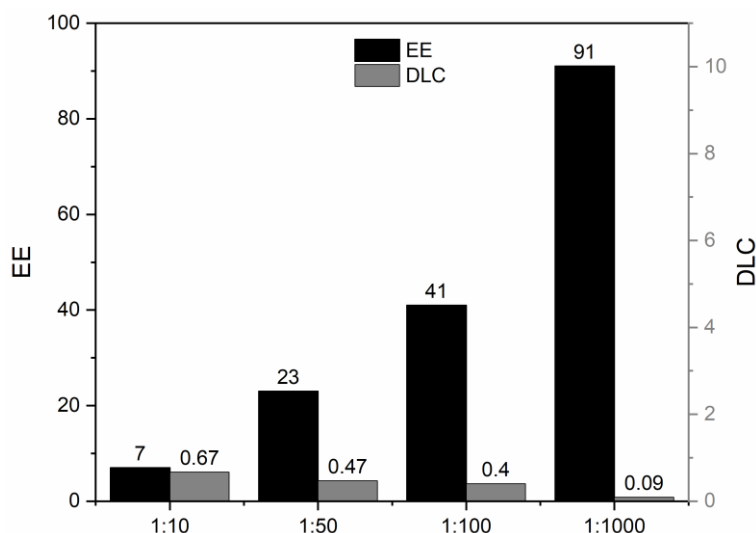
Figure 45. Encapsulation Efficiency (EE) and Drug loading capacity (DLC) of resveratrol on LHC2 composite.

4.2.5 Biological studies

To test the cytotoxicity of the new biomaterial, as it is and resveratrol loaded we performed an in vitro biological assay on HTC-116 colon cancer cells proliferation by the MTT method. Figure 46 shows the biological activity of resveratrol alone and in association with LHC2 (1:10 w/w ratio) against HTC-116 cells. Our data show a distinct inhibitory activity of cell viability of resveratrol alone and in association with LHC2. In particular, the activity of resveratrol alone is equal to a maximum percentage of reduction of 69.3% and strongly dependent on the type of control used for comparison (66.4–57.1% versus the control without ethanol and 69.3–60.8%

versus the control with ethanol). In fact, as previously demonstrated,[115] ethanol, the solvent used for better solubilizing the resveratrol, has shown a positive effect on cell viability equal to 9.5% compared to the untreated control.

The cytotoxic activity of LHC2 (27.1–7.9% versus the control without ethanol and 33.4–15.9% versus the control with ethanol) is lower and inversely proportional to the dose used; this is probably due to a saturation effect rather than to a specific mechanism, given its non-solubility. In the association with resveratrol, this phenomenon is evidently canceled by its specific and powerful inhibitory action; however, there is a slight decrease in intrinsic activity compared to the data obtained from resveratrol alone (60.4–47.1% versus the control without ethanol and 63.8–51.7% versus ethanol control).

Based on these results, we can conclude that resveratrol confirmed its potent inhibitory activity. Interestingly, the association with the LHC2 vehicle did not significantly lose its intrinsic activity.
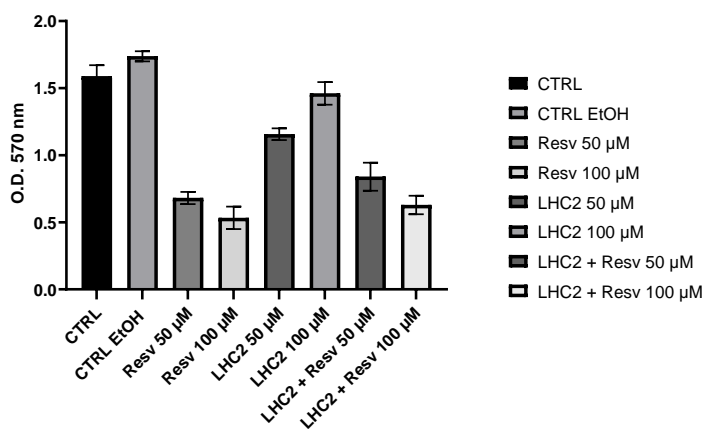

Figure 46. Biological activities of resveratrol alone and associated with LHC2 (1:10 w/w) against HTC 116 cell lines at 72 h.

4.3 Conclusion

In summary, to tackle the current adsorption problems of greenhouse gases such as CO_2 and the possibility of using eco-friendly materials for drug delivery, the development of new low-cost, easy-to-prepare, and environmentally sustainable materials could help solve these problems. We have developed a straightforward and rapid synthetic methodology to synthesize a new hybrid, ecological and reusable material starting from cheap materials such as loofah and halloysite. Considering the low amount of halloysite bound to loofah, the composites showed a significantly greater ability to absorb and retain carbon dioxide than non-contaminated materials. This underlines the synergistic effect of the two materials, which also possess a greater adsorption capacity than the BEA and MOR zeolites, which are currently used in the industrial field for gas adsorption and require more prolonged and more expensive synthetic processes. In addition, the presence of halloysite improves the mechanical properties of the loofah.

Moreover, the synergistic effect of the materials is evident in the greater carrying capacity of resveratrol compared to individual materials. Finally, the association with the LHC2 vehicle did not significantly affect the inhibitory activity of resveratrol against HCT-116 tumor cell lines. This study opens another way towards developing hybrid, organic-inorganic materials, applicable in multiple fields and at the same time eco-sustainable and economical.

4.4 Experimental section

General information. Loofah sponge was purchased from Ibérica de Esponjas Vegetales, SL. All the required chemicals were purchased from Merck and Aldrich Chemical Company. Pre-coated aluminium sheets (silica gel 60 F254, Merck) were used for thin-layer chromatography (TLC), visualizing spots under UV light. UV-vis measures were carried out with a Jasco V-730 spectrophotometer using quartz cuvettes.

Synthesis of LHCx and LHNx composites

100 mg of loofah and 500 mg of halloysite ($Al_2Si_2O_5(OH)_4$ 2 H_2O, MW: 294.19) were suspended in 10 mL of DMF and sonicated for 10 minutes at room temperature. Subsequently, the quantity of cross-linker C (1,1'-carbonyldiimidazole) or N (1,4,5,8-naphthalenetetracarboxylic dianhydride) was added with respect to halloysite moles, depending on the composite to be obtained: for the composites LHC2 and LHN2, 2 eq. of cross-linker were added; for the composites LHC10 and LHN10, 10 eq. of cross-linker were added; for the composites LHC20 and LHN20, 20 eq of cross-linker were added. In all cases, such a quantity of DMF was added to solubilize the added cross-linkers. The reaction mixture was stirred at 80 °C. Once the reaction was completed, the raw product was washed and sonicated with acetone several times until the solution was clear and dried under vacuum.
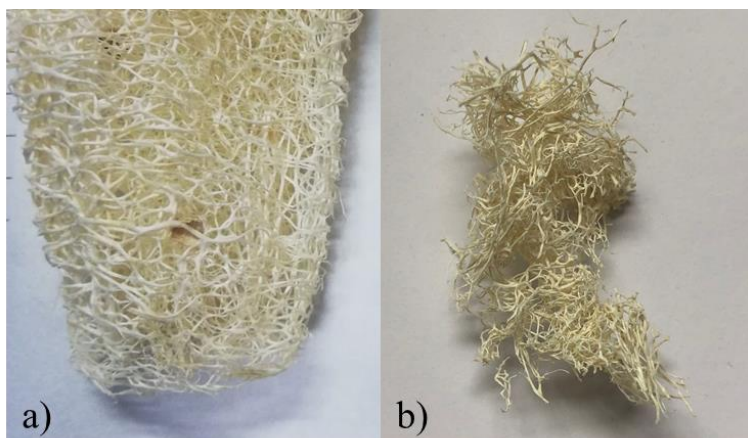
Figure 47. Loofah sponge (a) before of the functionalization and (b) after.

Characterizations

Infrared spectroscopy

The FT-IR ATR spectra were recorded in absorbance mode (64 scans and 4 cm^{-1} resolution) using a Varian 640-IR by Agilent Technologies, with a ZnSe crystal fixed at the incident angle of 45°. 10 mm fibers of each sample were mounted on top of ATR crystal and pressed gently by a pre-mounted sample clamp.

Thermogravimetric analysis (TGA)

Thermogravimetric analyses were conducted on a TA Instruments Q5000 IR. The tests were conducted with a temperature ramp of 10 °C/min from 25 °C to 900 °C under nitrogen flow of 25 cm^3 min^{-1} atmosphere, followed by 15 min isotherm at 900 °C in air flux. About 10 mg of each sample was collected from different points to analyze the sample homogeneously.

Figure 48. TGA traces of H (orange line), L (black line) and LH composites: a) LHC2 (red line), LHC10 (green line) and LHC20 (blue line); b) LHN2 (red line), LHN10 (green line) and LHN20 (blue line).

High-resolution transmission electron microscopy (HRTEM)

HRTEM micrographs on L, H, and LH samples, taken from the sonicated suspensions, were carried out with a Philips CM 200 field emission gun microscope

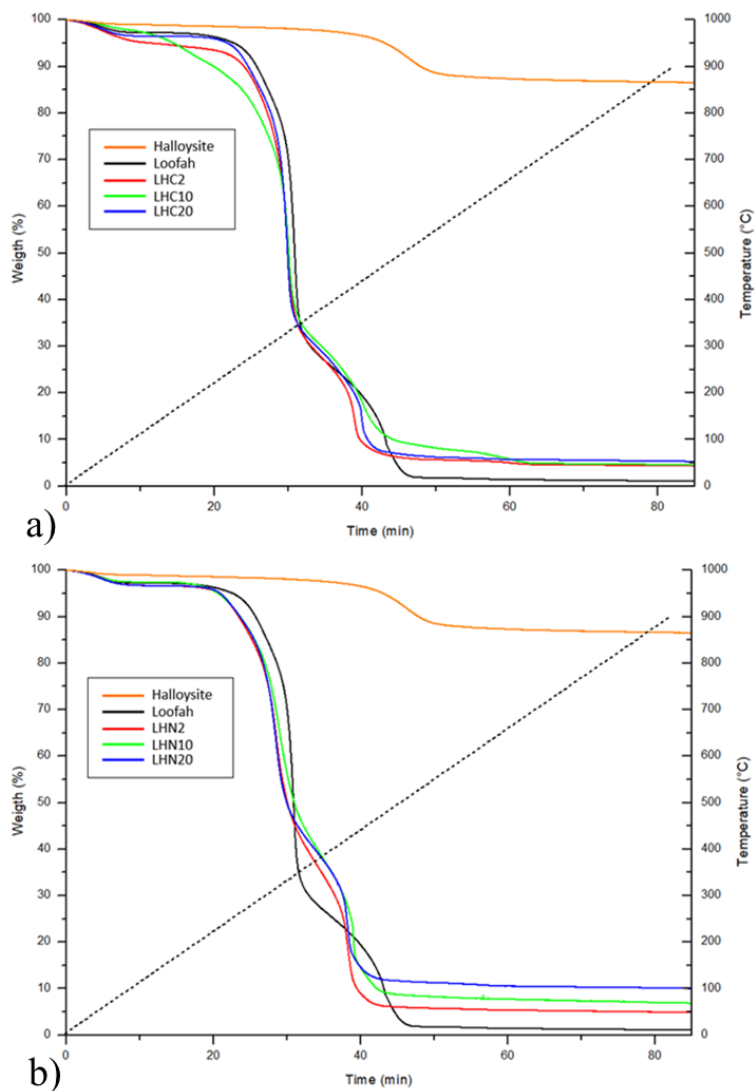operating at an accelerating voltage of 200 kV. Few drops of the suspension were deposited on a 200-mesh lacey carbon-coated copper grid and air-dried for several hours before analysis. During the acquisition of HRTEM images, the samples did not undergo structural transformation. Low beam current densities and short acquisition times were adopted. The Gatan Digital Micrograph software was used to estimate the dimensions of the halloysite nanotubes.

Scanning electron microscopy (SEM)

The loofah and LHNx composites morphology was analyzed by scanning electron microscopy (SEM). The specimens, mounted onto aluminium stubs, were sputter-coated with gold and examined with a StereoScan 360 Cambridge microscope at 10 kV. Samples were observed at 2000× and 10000× magnification, respectively.

Tensile Tests

The tensile tests were performed on a TA Instruments Rheometric Series RSA III analyzer. A sample of 30 mm length was clamped into the two jaws of the machine. Each end of the jaws covered 4 mm of the sample. Reading the tensile strength test instrument for Newton's force and extension was initially set to zero. Tensile stress was applied until the failure of the sample was obtained. Four (4) specimens of each sample have been used to measure the above mechanical properties at ambient laboratory environment, and average results are reported.

Table 13. Method adopted for the evaluation of tensile properties of Loofah and LH composites.

Sample	Stress at break (N)	Elongation at break (%)
Loofah	4.16	9.46
LNH2	5.77	16.47
LNH10	7.96	18.50
LNH20	8.24	17.41
LNC2	5.80	14.10
LNC10	8.31	16.22
LNC20	9.48	13.71

CO_2 adsorption and CO_2-TPD measurements

The carbon dioxide adsorption experiments were carried out in a quartz U-shape reactor, utilizing 150 mg of the investigated sample and a CO_2 (99.999%) flow of 30 mL/min. The CO_2 was detected by a quadrupole mass spectrometer (Sensorlab VG Quadrupoles) following the $m/z = 44$ signal. The breakthrough curves of CO_2 were determined by measuring the ratio between the concentration of CO_2 after the achievement of saturation in the sample and the initial carbon dioxide concentration (*i.e.*, without the sample). Before the measurements, the materials were pre-treated in He flow (50 mL/min) at 100 °C for 1 h to remove eventual impurities from the sample's surface. The amount of CO_2 adsorbed was calculated considering the following formula q (mg/g) $= [(C_{in} - C_f) \times t \times Q]/w$, where w is the weight of the examined sample (g), Q is the CO_2 flow rate (mL/min), t is the time (min) at which

the saturation was achieved, and C_{in} and C_f are the initial and final (at the saturation) CO_2 concentrations (mg/mL), respectively.[58]

The CO_2 TPD (Temperature Programmed Desorption) measurements were carried out in the same type of reactor utilizing 150 mg of sample. The CO_2 flow (30 mL/min) was stopped for these determinations after adsorption and surface saturation processes. Subsequently, the reactor was heated from 30 °C to 400 °C (10 °C/min). After desorption, the products were analyzed with the mass spectrometer. Also, in this case, the samples were pre-treated with a He flow (50 mL/min) for 1 h at 100 °C.
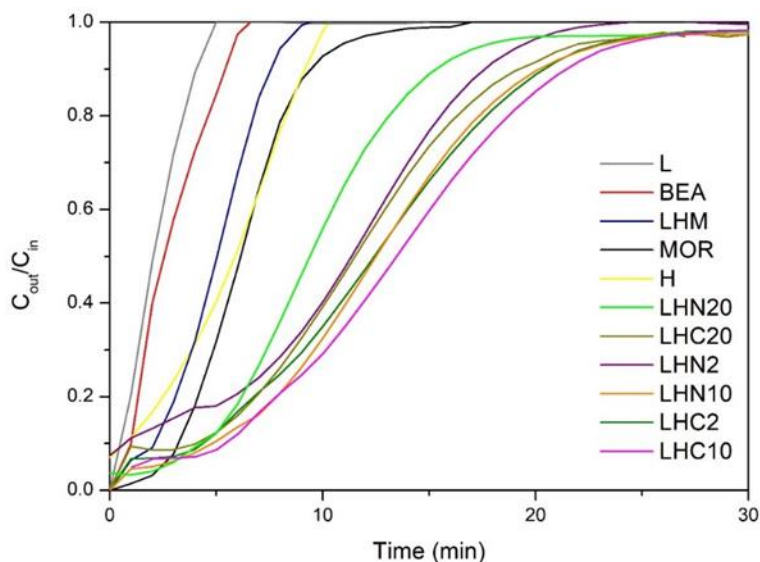
Figure 49. Breakthrough curves of CO_2 for the investigated samples.
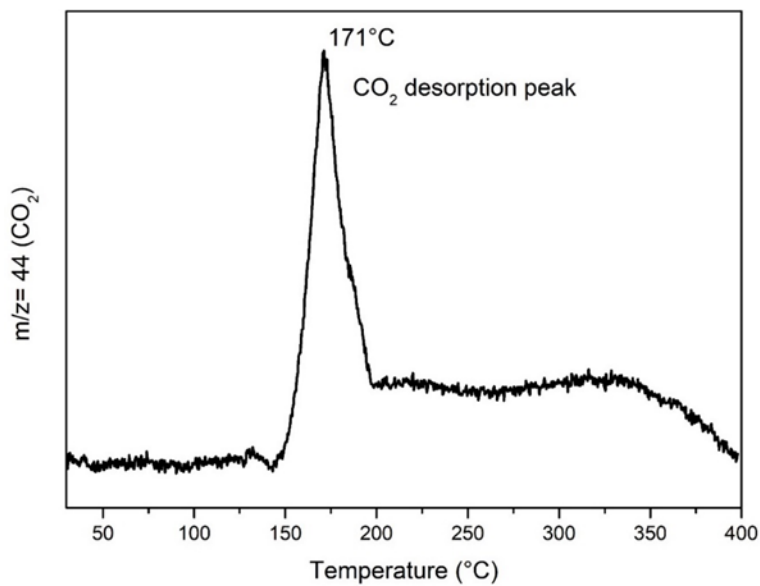
Figure 50. CO$_2$-TPD profile of LHC2 composite.
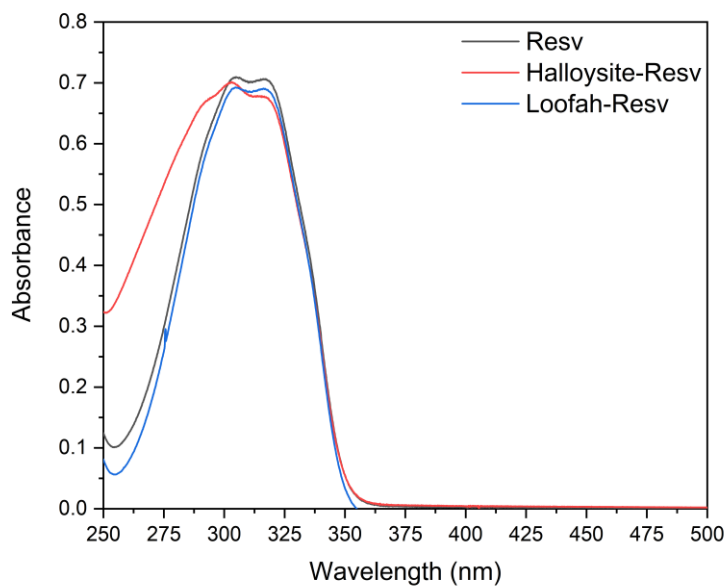
Figure 51. UV spectrum of the loading capacity of resveratrol on the individual starting materials.
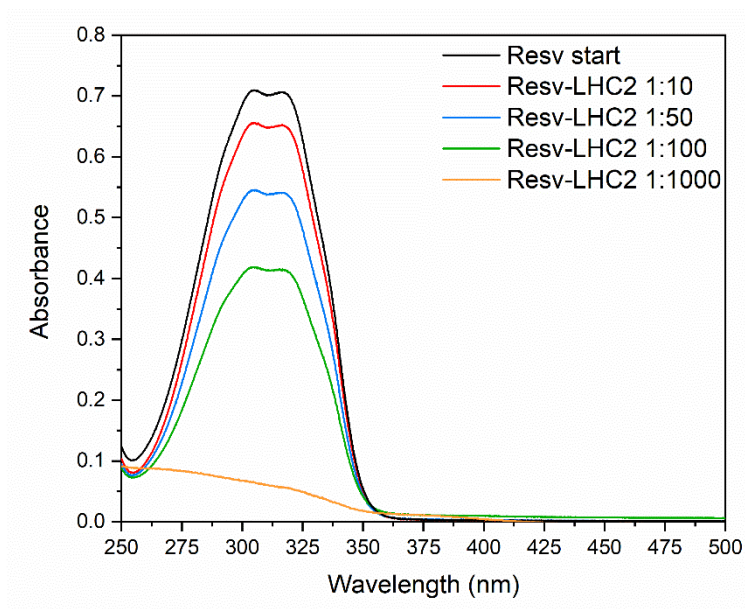
Figure 52. UV spectrum of the loading capacity of resveratrol on the LHC2 composite with different ratios.

Biological assay

The HCT 116 cells were plated in a 24-well plate at a density of 5×104/well. Cell viability was measured through the colorimetric tetrazolium salts assay. This assumption assumes total cellular integrity and assesses the ability of cells to reduce, employing the mitochondrial succinate dehydrogenase, 3-(4,5-dimethylthiazol-2-yl)-2,5-diphenyl tetrazolium bromide (MTT). The tetrazolium salts enter the cells and are transformed into violet-colored formazan crystals. The level of formazan is used as an indirect index of cell density. After incubating the cells for 3 hours, in 5% CO_2 at 37 °C, with 500 µL of the tetrazolium salt solution (5mg/mL), the supernatant was removed, and 500 µL of DMSO per well was added, for the elution of the

crystals allowing the measurement of the optical density (O.D.) at a wavelength of 570 nm with the use of a spectrophotometer for microplates (Titertek Multiscan, Flow Laboratories).

Briefly, HCT 116 cells were seeded in the 24-well plate at a density of 5×104 cells in RPMI 1640 (Gibco) medium supplemented with 10% FBS, 1% Pen/Strep antibiotics, and 2 mM glutamine. The treatments were carried out after 24 hours from when they were sown according to the protocol. Cell viability was determined by MTT testing, following the supplier's instructions. Each test was conducted in triplicate, and the results were expressed as mean ± SD.

All experiments were conducted in triplicate, and the results were expressed as mean ± SD. The data was processed via one-way ANOVA (Tukey's multiple comparisons test), using a p-value <0.05 as a threshold for statistical significance.

References

(1)   Atwood, J. L.; Davies, J. E. D.; MacNicol, D. D. *Inclusion compounds*; Academic Press: London ; Orlando, 1984.

(2)   Blacker, A. J.; Jazwinski, J.; Lehn, J. M. Molecular Anion Binding and Substrate Photooxidation in Visible-Light by 2,7-Diazapyrenium Cations. *Helv Chim Acta* **1987,** *70* (1), 1.

(3)   Cram, D. J. The Design of Molecular Hosts, Guests, and Their Complexes (Nobel Lecture). *Angewandte Chemie-International Edition in English* **1988,** *27* (8), 1009.

(4)   Cram, D. J. Preorganization - from Solvents to Spherands. *Angewandte Chemie-International Edition in English* **1986,** *25* (12), 1039.

(5)   Cramer, F.; Freist, W. Molecular Recognition by Energy-Dissipation, a New Enzymatic Principle - the Example Isoleucine Valine. *Accounts Chem Res* **1987,** *20* (3), 79.

(6)   Koshland, D. E. The Key-Lock Theory and the Induced Fit Theory. *Angew Chem Int Edit* **1994,** *33* (23-24), 2375.

(7)   Hosseini, M. W.; Lehn, J. M. Cocatalysis - Pyrophosphate Synthesis from Acetylphosphate Catalyzed by a Macrocyclic Polyamine. *J Chem Soc Chem Comm* **1985**, DOI:DOI 10.1039/c39850001155 DOI 10.1039/c39850001155(17), 1155.

(8)   Jullien, L.; Lehn, J. M. The Chundle Approach to Molecular Channels Synthesis of a Macrocycle Based Molecular Bundle. *Tetrahedron Lett* **1988,** *29* (31), 3803.

(9)   Terminassiansaraga, L.; Adler, M.; Barraud, A.; Churaev, N. V.; Eaton, D. F.; Kuhn, H.; Misono, M.; Platikanov, D.; Ralston, J.; Silberberg, A.et al. Thin-Films Including Layers - Terminology in Relation to Their Preparation and Characterization. *Pure Appl Chem* **1994,** *66* (8), 1667.

(10)   Shimizu, T.; Masuda, M.; Minamikawa, H. Supramolecular nanotube architectures based on amphiphilic molecules. *Chem Rev* **2005,** *105* (4), 1401.

(11)   Lehn, J. M. Supramolecular Chemistry. *Science* **1993,** *260* (5115), 1762.

(12)   Schmidtchen, F. P.; Berger, M. Artificial organic host molecules for anions. *Chem Rev* **1997,** *97* (5), 1609.

(13)   Lehn, J. M. Supramolecular Chemistry - Scope and Perspectives Molecules, Supermolecules, and Molecular Devices. *Angew Chem Int Edit* **1988,** *27* (1), 89.

(14)   Lehn, J. M. Supramolecular Chemistry - Receptors, Catalysts, and Carriers. *Science* **1985,** *227* (4689), 849.

(15)   Gokel, G. W.; Murillo, O. Synthetic organic chemical models for transmembrane channels. *Accounts Chem Res* **1996,** *29* (9), 425.

(16)   Floresta, G.; Talotta, C.; Gaeta, C.; De Rosa, M.; Chiacchio, U.; Neri, P.; Rescifina, A. gamma-Cyclodextrin as a Catalyst for the Synthesis of 2-Methyl-3,5-diarylisoxazolidines in Water. *J Org Chem* **2017,** *82* (9), 4631.

(17)   Rebek, J. Molecular Recognition with Model Systems. *Angewandte Chemie-International Edition in English* **1990,** *29* (3), 245.

(18)   Bajaj, A. V.; Poonia, N. S. Comprehensive Coordination Chemistry of Alkali and Alkaline-Earth Cations with Macrocyclic Multidentates - Latest Position. *Coordin Chem Rev* **1988,** *87*, 55.

(19)   Gaeta, C.; Talotta, C.; De Rosa, M.; La Manna, P.; Soriente, A.; Neri, P. The Hexameric Resorcinarene Capsule at Work: Supramolecular Catalysis in Confined Spaces. *Chem-Eur J* **2019,** *25* (19), 4899.

(20)   La Manna, P.; Talotta, C.; Floresta, G.; De Rosa, M.; Soriente, A.; Rescifina, A.; Gaeta, C.; Neri, P. Mild Friedel-Crafts Reactions inside a Hexameric Resorcinarene Capsule: C-Cl Bond Activation through Hydrogen Bonding to Bridging Water Molecules. *Angew Chem Int Edit* **2018,** *57* (19), 5423.

(21)   Assaf, K. I.; Nau, W. M. Cucurbiturils: from synthesis to high-affinity binding and catalysis. *Chem Soc Rev* **2015,** *44* (2), 394.

(22)   Gerasko, O. A.; Samsonenko, D. G.; Fedin, V. P. Supramolecular chemistry of cucurbiturils. *Usp Khim+* **2002,** *71* (9), 840.

(23)   Zhang, M. M.; Sigwalt, D.; Isaacs, L. Differentially functionalized acyclic cucurbiturils: synthesis, self-assembly and CB[6]-induced allosteric guest binding. *Chem Commun* **2015,** *51* (78), 14620.

(24)   Palma, A.; Artelsmair, M.; Wu, G. L.; Lu, X. Y.; Barrow, S. J.; Uddin, N.; Rosta, E.; Masson, E.; Scherman, O. A. Cucurbit[7]uril as a Supramolecular Artificial Enzyme for Diels-Alder Reactions. *Angew Chem Int Edit* **2017,** *56* (49), 15688.

(25)   Day, A.; Arnold, A. P.; Blanch, R. J.; Snushall, B. Controlling factors in the synthesis of cucurbituril and its homologues. *J Org Chem* **2001,** *66* (24), 8094.

(26)   Barrow, S. J.; Kasera, S.; Rowland, M. J.; del Barrio, J.; Scherman, O. A. Cucurbituril-Based Molecular Recognition. *Chem Rev* **2015,** *115* (22), 12320.

(27)   Floresta, G.; Rescifina, A. Metyrapone-beta-cyclodextrin supramolecular interactions inferred by complementary spectroscopic/spectrometric and computational studies. *J Mol Struct* **2019,** *1176*, 815.

(28)   Jiao, D. Z.; Zhao, N.; Scherman, O. A. A "green" method for isolation of cucurbit[7]uril via a solid state metathesis reaction. *Chem Commun* **2010,** *46* (12), 2007.

(29)   Casuscelli, F.; Chiacchio, U.; Rescifina, A.; Romeo, R.; Romeo, G.; Tommasini, S.; Uccella, N. Ring-Opening of Isoxazolidine Nucleus - Competitive Formation of Alpha,Beta-Enones and Tetrahydro-1,3-Oxazines. *Tetrahedron* **1995,** *51* (10), 2979.

(30)   Floresta, G.; Talotta, C.; Gaeta, C.; De Rosa, M.; Chiacchio, U.; Neri, P.; Rescifina, A. gamma-Cyclodextrin as a Catalyst for the Synthesis of 2-Methyl-3,5-diarylisoxazolidines in Water. *J Org Chem* **2017,** *82* (9), 4631.

(31)   Hong, C. M.; Bergman, R. G.; Raymond, K. N.; Toste, F. D. Self-Assembled Tetrahedral Hosts as Supramolecular Catalysts. *Accounts Chem Res* **2018,** *51* (10), 2447.

(32)   Caulder, D. L.; Powers, R. E.; Parac, T. N.; Raymond, K. N. The self-assembly of a predesigned tetrahedral M4L6 supramolecular cluster. *Angew Chem Int Edit* **1998,** *37* (13-14), 1840.

(33)   Caulder, D. L.; Bruckner, C.; Powers, R. E.; Konig, S.; Parac, T. N.; Leary, J. A.; Raymond, K. N. Coordination number incommensurate cluster formation, part 21 - Design, formation and properties of tetrahedral M4L4 and M4L6 supramolecular clusters. *J Am Chem Soc* **2001,** *123* (37), 8923.

(34)   Prat, D.; Hayler, J.; Wells, A. A survey of solvent selection guides. *Green Chem.* **2014,** *16* (10), 4546.

(35)   Byrne, F. P.; Jin, S.; Paggiola, G.; Petchey, T. H. M.; Clark, J. H.; Farmer, T. J.; Hunt, A. J.; Robert McElroy, C.; Sherwood, J. Tools and techniques for solvent selection: green solvent selection guides. *Sustainable Chemical Processes* **2016,** *4* (1), 7.

(36)   Li, T. Z.; Liu, S. J.; Sun, Y. W.; Deng, S.; Tan, W.; Jiao, Y. C.; Zhang, Y. C.; Shi, F. Regio- and Enantioselective (3+3) Cycloaddition of Nitrones with 2-Indolylmethanols Enabled by Cooperative Organocatalysis. *Angewandte Chemie-International Edition* **2021,** *60* (5), 2355.

(37)   Murahashi, S. I.; Imada, Y. Synthesis and Transformations of Nitrones for Organic Synthesis. *Chem. Rev.* **2019,** *119* (7), 4684.

(38)   Hong, Z. Y.; Liu, L.; Hsu, C. C.; Wong, C. H. Three-step synthesis of sialic acids and derivatives. *Angew Chem Int Edit* **2006,** *45* (44), 7417.

(39)   Yavuz, S.; Ozkan, H.; Colak, N.; Yildirir, Y. Fast Method for Synthesis of Alkyl and Aryl-N-Methylnitrones. *Molecules* **2011,** *16* (8), 6677.

(40)   Lebel, N. A.; Balasubramanian, N. A Convenient Synthesis of Nitrones by Normal-Alkylation of Ortho-Trimethylsilyloximes. *Tetrahedron Lett* **1985,** *26* (36), 4331.

(41)   Floresta, G.; Punzo, F.; Rescifina, A. Supramolecular host-guest interactions of pseudoginsenoside F11 with beta- and gamma-cyclodextrin: Spectroscopic/spectrometric and computational studies. *J. Mol. Struct.* **2019,** *1195*, 387.

(42)   Cameron, K. S.; Fielding, L. NMR diffusion spectroscopy as a measure of host-guest complex association constants and as a probe of complex size. *J. Org. Chem.* **2001,** *66* (21), 6891.

(43)   Zhao, R.; Sandstrom, C.; Zhang, H.; Tan, T. NMR Study on the Inclusion Complexes of beta-Cyclodextrin with Isoflavones. *Molecules* **2016,** *21* (4), 372.

(44)   Heo, J.; Kim, J.; Whang, D.; Kim, K. Columnar one-dimensional coordination polymer formed with a metal ion and a host-guest complex as building blocks: potassium ion complexed cucurbituril. *Inorg Chim Acta* **2000,** *297* (1-2), 307.

(45)   Lim, S.; Kim, H.; Selvapalam, N.; Kim, K. J.; Cho, S. J.; Seo, G.; Kim, K. Cucurbit[6]uril: Organic molecular porous material with permanent porosity, exceptional stability, and acetylene sorption properties. *Angew Chem Int Edit* **2008,** *47* (18), 3352.

(46)   Shao, L.; Zhong, J. R.; Ren, Y. M.; Tang, H.; Wang, X. F. Perhydroxy-CB[6] decorated graphene oxide composite for uranium(VI) removal. *J Radioanal Nucl Ch* **2017,** *311* (1), 627.

(47)   Tian, J.; Ma, S. Q.; Thallapally, P. K.; Fowler, D.; McGrail, B. P.; Atwood, J. L. Cucurbit[7]uril: an amorphous molecular material for highly selective carbon dioxide uptake. *Chem Commun* **2011,** *47* (27), 7626.

(48)   Kim, H.; Kim, Y.; Yoon, M.; Linn, S.; Park, S. M.; Seo, G.; Kim, K. Highly Selective Carbon Dioxide Sorption in an Organic Molecular Porous Material. *J Am Chem Soc* **2010,** *132* (35), 12200.

(49)   Montes-Navajas, P.; Corma, A.; Garcia, H. Supramolecular ionic liquids based on host-guest cucurbituril imidazolium complexes. *J Mol Catal a-Chem* **2008,** *279* (2), 165.

(50)   Gentile, D.; Floresta, G.; Patamia, V.; Nicosia, A.; Mineo, P. G. G.; Rescifina, A. Cucurbit[7]uril as a catalytic nanoreactor for one-pot synthesis of isoxazolidines in water. *Org Biomol Chem* **2020,** *18* (6), 1194.

(51)   Ma, L.; Haynes, C. J. E.; Grommet, A. B.; Walczak, A.; Parkins, C. C.; Doherty, C. M.; Longley, L.; Tron, A.; Stefankiewicz, A. R.; Bennett, T. D.et al. Coordination cages as permanently porous ionic liquids. *Nat Chem* **2020,** *12* (3), 270.

(52)   Appaturi, J. N.; Adam, F. ImX-MCM-41 (X = Cl, Br and I): Active catalysts for the solvent free synthesis of phenyl glycidyl carbonate. *Surf Interfaces* **2019,** *14*, 305.

(53)   Liu, H.; Guo, P.; Chen, G. J. Investigation of CO2 capture efficiency and mechanism in 2-methylimidazole-glycol solution. *Sep Purif Technol* **2017,** *189*, 66.

(54)   Trotta, F.; Cavalli, R.; Martina, K.; Biasizzo, M.; Vitillo, J. G.; Bordiga, S.; Vavia, P.; Ansari, K. Cyclodextrin nanosponges as effective gas carriers. *J Incl Phenom Macro* **2011,** *71* (1-2), 189.

(55)   Jon, S. Y.; Selvapalam, N.; Oh, D. H.; Kang, J. K.; Kim, S. Y.; Jeon, Y. J.; Lee, J. W.; Kim, K. Facile synthesis of cucurbit[n]uril derivatives via direct functionalization: Expanding utilization of cucurbit[n]uril. *J Am Chem Soc* **2003,** *125* (34), 10186.

(56)   Meng, D.; Liang, H. L.; Chen, Q. D.; Shen, X. H. Preparation and characterization of a novel single crystal of Th(IV) with cucurbit[6]uril. *Chinese Chem Lett* **2018,** *29* (3), 447.

(57)   Feng, Y.; Schmidt, A.; Weiss, R. A. Compatibilization of polymer blends by complexation .1. Spectroscopic characterization of ion-amide interactions in ionomer/polyamide blends. *Macromolecules* **1996,** *29* (11), 3909.

(58)   Lu, C. Y.; Bai, H. L.; Wu, B. L.; Su, F. S.; Fen-Hwang, J. Comparative study of CO2 capture by carbon nanotubes, activated carbons, and zeolites. *Energ Fuel* **2008,** *22* (5), 3050.

(59)   Yang, S. T.; Kim, J.; Ahn, W. S. CO2 adsorption over ion-exchanged zeolite beta with alkali and alkaline earth metal ions. *Micropor Mesopor Mat* **2010,** *135* (1-3), 90.

(60)   Liu, Y. N.; Wang, Z.; Shi, M. Q.; Li, N.; Zhao, S.; Wang, J. X. Carbonic anhydrase inspired poly(N- vinylimidazole)/zeolite Zn- b hybrid membranes for CO2 capture+. *Chem Commun* **2018,** *54* (52), 7239.

(61)   Delgado, M. R.; Arean, C. O. Carbon monoxide, dinitrogen and carbon dioxide adsorption on zeolite H-Beta: IR spectroscopic and thermodynamic studies. *Energy* **2011,** *36* (8), 5286.

(62)   Yang, J. F.; Li, J. M.; Wang, W.; Li, L. B.; Li, J. P. Adsorption of CO2, CH4, and N-2 on 8-, 10-, and 12-Membered Ring Hydrophobic Microporous High-Silica Zeolites: DDR, Silicalite-1, and Beta. *Ind Eng Chem Res* **2013,** *52* (50), 17856.

(63)   Singh, G.; Lee, J.; Karakoti, A.; Bahadur, R.; Yi, J. B.; Zhao, D. Y.; AlBahily, K.; Vinu, A. Emerging trends in porous materials for CO(2)capture and conversion. *Chem Soc Rev* **2020,** *49* (13), 4360.

(64)   Kumar, S.; Srivastava, R.; Koh, J. Utilization of zeolites as CO2 capturing agents: Advances and future perspectives. *J Co2 Util* **2020,** *41*.

(65)   Deng, H.; Pan, T. T.; Zhang, Y.; Wang, L.; Wu, Q. M.; Ma, J. Z.; Shan, W. P.; He, H. Adsorptive removal of toluene and dichloromethane from humid exhaust on MFI, BEA and FAU zeolites: An experimental and theoretical study. *Chem Eng J* **2020,** *394*.

(66)   Sing, K. S. W.; Everett, D. H.; Haul, R. A. W.; Moscou, L.; Pierotti, R. A.; Rouquerol, J.; Siemieniewska, T. Reporting Physisorption Data for Gas Solid Systems with Special Reference to the Determination of Surface-Area and Porosity (Recommendations 1984). *Pure Appl Chem* **1985,** *57* (4), 603.

(67)   Esparza, J. M.; Ojeda, M. L.; Campero, A.; Hernandez, G.; Felipe, C.; Asomoza, M.; Cordero, S.; Kornhauser, I.; Rojas, F. Development and sorption characterization of some model mesoporous and microporous silica adsorbents. *J Mol Catal a-Chem* **2005,** *228* (1-2), 97.

(68)   Srinivas, G.; Krungleviciute, V.; Guo, Z. X.; Yildirim, T. Exceptional CO2 capture in a hierarchically porous carbon with simultaneous high surface area and pore volume. *Energ Environ Sci* **2014,** *7* (1), 335.

(69)   Chang, L.; Stacchiola, D. J.; Hu, Y. H. Direct conversion of CO2 to meso/macro-porous frameworks of surface-microporous graphene for efficient asymmetrical supercapacitors. *J Mater Chem A* **2017,** *5* (44), 23252.

(70)   Giammanco, C. H.; Kramer, P. L.; Yamada, S. A.; Nishida, J.; Tamimi, A.; Fayer, M. D. Coupling of Carbon Dioxide Stretch and Bend Vibrations Reveals Thermal Population Dynamics in an Ionic Liquid. *J Phys Chem B* **2016,** *120* (3), 549.

(71)   Zhang, H.; Liu, J. R.; Li, M. T.; Yang, B. L. Functional groups in geminal imidazolium ionic compounds and their influence on thermo-physical properties. *J Mol Liq* **2018,** *269*, 738.

(72)   Zeng, C. F.; Tang, Z. H.; Guo, B. C.; Zhang, L. Q. Supramolecular ionic liquid based on graphene oxide. *Phys Chem Chem Phys* **2012,** *14* (28), 9838.

(73)   Wu, A. L.; Lu, F.; Sun, P. P.; Qiao, X. X.; Gao, X. P.; Zheng, L. Q. Low-Molecular-Weight Supramolecular Ionogel Based on Host-Guest Interaction. *Langmuir* **2017,** *33* (49), 13982.

(74)   Raoov, M.; Mohamad, S.; Abas, M. R. Synthesis and Characterization of beta-Cyclodextrin Functionalized Ionic Liquid Polymer as a Macroporous

Material for the Removal of Phenols and As(V). *Int J Mol Sci* **2014,** *15* (1), 100.

(75) Ghosh, S.; Ghosh, A.; Riyajuddin, S.; Sarkar, S.; Chowdhury, A. H.; Ghosh, K.; Islam, S. M. Silver Nanoparticles Architectured HMP as a Recyclable Catalyst for Tetramic Acid and Propiolic Acid Synthesis through CO2 Capture at Atmospheric Pressure. *Chemcatchem* **2020,** *12* (4), 1055.

(76) Xie, J. N.; Yu, B.; Zhou, Z. H.; Fu, H. C.; Wang, N.; He, L. N. Copper(I)-based ionic liquid-catalyzed carboxylation of terminal alltynes with CO2 at atmospheric pressure. *Tetrahedron Lett* **2015,** *56* (50), 7059.

(77) Sun, J.; Wang, J. Q.; Cheng, W. G.; Zhang, J. X.; Li, X. H.; Zhang, S. J.; She, Y. B. Chitosan functionalized ionic liquid as a recyclable biopolymer-supported catalyst for cycloaddition of CO2. *Green Chem* **2012,** *14* (3), 654.

(78) Coates, J. P. The interpretation of infrared spectra: Published reference sources. *Appl Spectrosc Rev* **1996,** *31* (1-2), 179.

(79) Katsyuba, S. A.; Dyson, P. J.; Vandyukova, E. E.; Chernova, A. V.; Vidis, A. Molecular structure, vibrational spectra, and hydrogen bonding of the ionic liquid 1-ethyl-3methyl-1H-imidazolium tetrafluoroborate. *Helv Chim Acta* **2004,** *87* (10), 2556.

(80) Chen, Y. X.; Zhang, K. T.; Yuan, F. C.; Zhang, T. T.; Weng, B. B.; Wu, S. S.; Huang, A. Y.; Su, N.; Guo, Y. Properties of Two-Variety Natural Luffa Sponge Columns as Potential Mattress Filling Materials. *Materials* **2018,** *11* (4).

(81) Shen, J. H.; Xie, Y. M.; Huang, X. D.; Zhou, S. W.; Ruan, D. Mechanical properties of luffa sponge. *J Mech Behav Biomed* **2012,** *15*, 141.

(82) Choi, K. S.; Kim, Y. H.; Kim, S. O.; Shin, K. O.; Chung, K. H. Effect of intake of sponge gourd (Luffa cylindrica) seed oil and Yukdomok (Chionanthus retusa L.) seed oil on lipid levels of blood and organs of a mice. *Food Sci Biotechnol* **2013,** *22* (3), 757.

(83)   Islam, M. R.; Nishida, H.; Funatsu, G. Complete Amino-Acid-Sequence of Luffin-a, a Ribosome-Inactivating Protein from the Seeds of Sponge Gourd (Luffa-Cylindrica). *Agr Biol Chem Tokyo* **1990,** *54* (11), 2967.

(84)   Demir, H.; Top, A.; Balkose, D.; Ulku, S. Dye adsorption behavior of Luffa cylindrica fibers. *J Hazard Mater* **2008,** *153* (1-2), 389.

(85)   Ahmadi, M.; Vahabzadeh, F.; Bonakdarpour, B.; Mehranian, M. Empirical modeling of olive oil mill wastewater treatment using loofa-immobilized Phanerochaete chrysosporium. *Process Biochem* **2006,** *41* (5), 1148.

(86)   Chen, J. P.; Lin, T. C. Loofa sponge as a scaffold for culture of rat hepatocytes. *Biotechnol Progr* **2005,** *21* (1), 315.

(87)   In-na, P.; Umar, A. A.; Wallace, A. D.; Flickinger, M. C.; Caldwell, G. S.; Lee, J. G. M. Loofah-based microalgae and cyanobacteria biocomposites for intensifying carbon dioxide capture. *J Co2 Util* **2020,** *42*.

(88)   Ma, Z. J.; Chen, W. B.; Hu, Z. L.; Pan, X. Z.; Peng, M. Y.; Dong, G. P.; Zhou, S. F.; Zhang, Q. Y.; Yang, Z. M.; Qiu, J. R. Luffa-Sponge-Like Glass-TiO2 Composite Fibers as Efficient Photocatalysts for Environmental Remediation. *Acs Appl Mater Inter* **2013,** *5* (15), 7527.

(89)   Papanicolaou, G. C.; Psarra, E.; Anastasiou, D. Manufacturing and mechanical response optimization of epoxy resin/Luffa Cylindrica composite. *J Appl Polym Sci* **2015,** *132* (22).

(90)   Siqueira, G.; Bras, J.; Dufresne, A. Luffa Cylindrica as a Lignocellulosic Source of Fiber, Microfibrillated Cellulose, and Cellulose Nanocrystals. *Bioresources* **2010,** *5* (2), 727.

(91)   Boynard, C. A.; D'Almeida, J. R. M. Water absorption by sponge gourd (luffa cylindrica)-polyester composite materials. *J Mater Sci Lett* **1999,** *18* (21), 1789.

(92)   Acosta-Rubi, S.; Campocosio, A. T.; Montes-Horcasitas, M. D.; Quintanar-Vera, L.; Esparza-Garcia, F.; Rodriguez-Vazquez, R. Production of a halotolerant biofilm from green coffee beans immobilized on loofah fiber

(Luffa cylindrica) and its effect on phenanthrene degradation in seawater. *J Environ Sci Heal A* **2017,** *52* (7), 632.

(93)   Stella, S. M.; Vijayalakshmi, U. Influence of chemically modified Luffa on the preparation of nanofiber and its biological evaluation for biomedical applications. *J Biomed Mater Res A* **2019,** *107* (3), 610.

(94)   Yuan, P.; Tan, D. Y.; Annabi-Bergaya, F. Properties and applications of halloysite nanotubes: recent research advances and future prospects. *Appl Clay Sci* **2015,** *112*, 75.

(95)   Churchman, G. J.; Davy, T. J.; Aylmore, L. A. G.; Gilkes, R. J.; Self, P. G. Characteristics of Fine Pores in Some Halloysites. *Clay Miner* **1995,** *30* (2), 89.

(96)   Yiu, H. H. P.; Wright, P. A.; Botting, N. P. Enzyme immobilisation using siliceous mesoporous molecular sieves. *Micropor Mesopor Mat* **2001,** *44*, 763.

(97)   Vergaro, V.; Abdullayev, E.; Lvov, Y. M.; Zeitoun, A.; Cingolani, R.; Rinaldi, R.; Leporatti, S. Cytocompatibility and Uptake of Halloysite Clay Nanotubes. *Biomacromolecules* **2010,** *11* (3), 820.

(98)   Gulcin, I. Antioxidant properties of resveratrol: A structure-activity insight. *Innov Food Sci Emerg* **2010,** *11* (1), 210.

(99)   Brisdelli, F.; D'Andrea, G.; Bozzi, A. Resveratrol: A Natural Polyphenol with Multiple Chemopreventive Properties (Review). *Curr Drug Metab* **2009,** *10* (6), 530.

(100)   Wicinski, M.; Domanowska, A.; Wodkiewicz, E.; Malinowski, B. Neuroprotective Properties of Resveratrol and Its Derivatives-Influence on Potential Mechanisms Leading to the Development of Alzheimer's Disease. *Int J Mol Sci* **2020,** *21* (8).

(101)   Pedrazzo, A. R.; Caldera, F.; Zanetti, M.; Appleton, S. L.; Dahkar, N. K.; Trotta, F. Mechanochemical green synthesis of hyper-crosslinked cyclodextrin polymers. *Beilstein J Org Chem* **2020,** *16*, 1554.

(102) Liang, W. T.; Yang, C.; Zhou, D. Y.; Haneoka, H.; Nishijima, M.; Fukuhara, G.; Mori, T.; Castiglione, F.; Mele, A.; Caldera, F.et al. Phase-controlled supramolecular photochirogenesis in cyclodextrin nanosponges. *Chem Commun* **2013,** *49* (34), 3510.

(103) Chen, Y. X.; Su, N.; Zhang, K. T.; Zhu, S. L.; Zhao, L.; Fang, F.; Ren, L. Y.; Guo, Y. In-Depth Analysis of the Structure and Properties of Two Varieties of Natural Luffa Sponge Fibers. *Materials* **2017,** *10* (5).

(104) Falcon, J. M.; Sawczen, T.; Aoki, I. V. Dodecylamine-Loaded Halloysite Nanocontainers for Active Anticorrosion Coatings. *Front Mater* **2015,** *2*.

(105) Huang, W. J.; Fernando, S.; Allard, L. F.; Sun, Y. P. Solubilization of single-walled carbon nanotubes with diamine-terminated oligomeric poly(ethylene glycol) in different functionalization reactions. *Nano Lett* **2003,** *3* (4), 565.

(106) Liu, C.; Hong, K. V.; Sun, X.; Natan, A.; Luan, P. C.; Yang, Y.; Zhu, H. L. An 'antifouling' porous loofah sponge with internal microchannels as solar absorbers and water pumpers for thermal desalination. *Journal of Materials Chemistry A* **2020,** *8* (25), 12323.

(107) Barman, M.; Mahmood, S.; Augustine, R.; Hasan, A.; Thomas, S.; Ghosal, K. Natural halloysite nanotubes/chitosan based bio-nanocomposite for delivering norfloxacin, an anti-microbial agent in sustained release manner. *Int. J. Biol. Macromol.* **2020,** *162*, 1849.

(108) Serra, R. M.; de Vilhena, F. S.; Gutierrez, L. B.; Junior, J. M. S.; Ferreira, G. B.; dos Santos, T. C.; Ronconi, C. M.; de Carneiro, J. W. M.; Boix, A. V. Experimental and theoretical investigation of the Na+ -> Li+ cation exchange in mordenite and its effect on CO2 adsorption properties. *Adsorption* **2021**, DOI:10.1007/s10450-020-00288-3 10.1007/s10450-020-00288-3.

(109) Villarreal, A.; Garbarino, G.; Riani, P.; Finocchio, E.; Bosio, B.; Ramirez, J.; Busca, G. Adsorption and separation of CO2 from N-2-rich gas on zeolites: Na-X faujasite vs Na-mordenite. *J Co2 Util* **2017,** *19*, 266.

(110) Gong, R. M.; Zhang, J.; Zhu, J.; Wang, J. T.; Lai, Q. M.; Jiang, B. Loofah sponge activated by periodate oxidation as a carrier for covalent immobilization of lipase. *Korean J Chem Eng* **2013,** *30* (8), 1620.

(111) Patamia, V.; Gentile, D.; Fiorenza, R.; Muccilli, V.; Mineo, P. G.; Scire, S.; Rescifina, A. Nanosponges based on self-assembled starfish-shaped cucurbit[6]urils functionalized with imidazolium arms. *Chem Commun (Camb)* **2021,** *57* (30), 3664.

(112) Zhao, Y. N.; Cai, C.; Liu, M.; Zhao, Y. P.; Wu, Y. S.; Fan, Z. P.; Ding, Z.; Zhang, H. Z.; Wang, Z. P.; Han, J. Drug-binding albumins forming stabilized nanoparticles for co-delivery of paclitaxel and resveratrol: In vitro/in vivo evaluation and binding properties investigation. *Int J Biol Macromol* **2020,** *153*, 873.

(113) Ansari, K. A.; Vavia, P. R.; Trotta, F.; Cavalli, R. Cyclodextrin-Based Nanosponges for Delivery of Resveratrol: In Vitro Characterisation, Stability, Cytotoxicity and Permeation Study. *Aaps Pharmscitech* **2011,** *12* (1), 279.

(114) Summerlin, N.; Soo, E.; Thakur, S.; Qu, Z.; Jambhrunkar, S.; Popat, A. Resveratrol nanoformulations: Challenges and opportunities. *Int J Pharmaceut* **2015,** *479* (2), 282.

(115) Cernigliaro, C.; D'Anneo, A.; Carlisi, D.; Giuliano, M.; Gammazza, A. M.; Barone, R.; Longhitano, L.; Cappello, F.; Emanuele, S.; Distefano, A.et al. Ethanol-Mediated Stress Promotes Autophagic Survival and Aggressiveness of Colon Cancer Cells via Activation of Nrf2/HO-1 Pathway. *Cancers* **2019,** *11* (4).